Novel High Voltage Electrodes for Li-ion Batteries

by

Rajesh Tripathi

A thesis
presented to the University of Waterloo
in fulfillment of the
thesis requirement for the degree of
Doctor of Philosophy
in
Chemistry

Waterloo, Ontario, Canada, 2013

AUTHOR'S DECLARATION

I hereby declare that I am the sole author of this thesis. This is a true copy of the thesis, including any required final revisions, as accepted by my examiners.

I understand that my thesis may be made electronically available to the public.

Rajesh Tripathi

Abstract

Li-ion batteries, as energy storage devices, have seen a remarkable improvement during the last two decades. The first and second generation of the positive electrode materials for Li-ion batteries, namely oxides and phosphates, were already known compounds in both in the mineralogical and chemical literature before being examined for their electrochemical properties. The latter compounds are known as the polyanion class of materials. Amongst them, the olivine $LiFePO_4$, which has a redox couple at 3.4 V *vs* Li, has been most extensively investigated due to its ease of synthesis and non-toxic properties. However, the understanding of the material's electrochemical behavior, especially why it can sustain such very high rates of discharge, is still not completely understood. Na-ion batteries, which operate on a similar principle as Li-ion batteries, are a very attractive alternative due to a relatively higher abundance of the sodium in nature. However, Na^+ ion is larger, heavier and less electronegative than Li^+ which significantly impacts Na^+ intercalation behavior in transition metal oxides and polyanion materials. As a result, the search for suitable electrode materials for Na-ion battery has not been as successful as for Li-ion battery.

An alternate family of "high" voltage (where the equilibrium voltage lies between 3.6 V and 4.2 V) polyanion cathode materials is reported in this thesis with the objective of improving specific energy density (Wh/kg) and developing a better understanding of polyanion electrochemistry. The electrochemical properties, synthesis and the structure of novel fluorosulfate materials crystallizing in the tavorite and the triplite type mineral structures are described. These materials display highest discharge voltages reported for any Fe^{2+}/Fe^{3+} redox couple. $LiFeSO_4F$ was prepared in both the tavorite and the triplite polymorphs using inexpensive and scalable methods. Complete structural characterization was performed using X-

ray and neutron based diffraction methods. A rapid synthesis of fluorosulfates can be achieved by using microwave heating. The local rapid heating created by the microwaves generates nanocrystalline $LiFeSO_4F$ tavorite with defects that induce significant microstrain. To date, this is unique to the microwave synthesis method. Phase transformation to the more stable triplite framework, facilitated by the lattice defects which include hydroxyl groups, is therefore easily triggered. The formation of nanocrystalline tavorite leads to nanocrystalline triplite, which greatly favors its electrochemical performance because of the inherently disordered nature of the triplite structure. Direct synthesis of the electrochemically active triplite type compound can be carried out either by extending the duration of the solvothermal reactions or by the partial substitution of Fe by Mn to produce $LiFe_{1-x}Mn_xSO_4F$. This study, overall, has led to a better understanding of the transformation of tavorite to the triplite phase.

To examine Li and the Na ion conduction and their correlation with the electrochemical performance of 3-D, 2-D and 1-D ion conductors, atomistic scale simulations have been used to investigate tavorite type $LiFeSO_4F$, $NaFeSO_4F$, olivine type $NaMPO_4$ (M= Fe, Mn, $Fe_{0.5}Mn_{0.5}$) and layered Na_2FePO_4F. These calculations predict high mobility of the Li-ion in the tavorite type $LiFeSO_4F$ but sluggish Na-ion transport in iso-structural $NaFeSO_4F$. High mobility of the Na-ion is predicted for phosphate layered and olivine structures.

Finally, the synthesis and structural details of $NaMSO_4F$ (M=Fe, Mn) and NH_4MSO_4F (M=Fe, Mn) are presented in the last chapter to show the structural diversity present in the fluorosulfate family.

Acknowledgements

I am indebted to my supervisor Professor Linda F. Nazar for her input and guidance. Her approach towards science and materials discovery, particularly, her emphasis on independent thinking has greatly inspired, motivated and shaped my approach for the last few years.

I would like to thank my PhD committee members Professor Holger Kleinke, Professor Pavle Radovanovic and Professor Dmitriy Soldatov (University of Guelph) for their time and guidance during this period. I am grateful to Professor M. Saiful Islam (University of Bath, UK) for a very fruitful collaboration and guidance in atomistic scale simulation studies. I am very thankful to Dr. Ashfia Huq (Oak Ridge National Lab, USA) for assistance in neutron diffraction studies. I would also thank Professor Jeffrey Dahn from Dalhousie University and Professor Zhongwei Chen from the Chemical Engineering department for their time being the external committee members.

I would also like to extend my sincere thanks to Dr. Guerman Popov, Dr. Brian Ellis, Dr. Ramesh Aditya, Dr. Prakash Badi, Dr. Xiulei Ji, Dr. Guang He, Dr. Grahame Gardiner (University of Bath, U.K.), Xiaoqi Sun, Elahe Talaie Pashiri, Stepehen M. Wood (University of Bath, U.K.) and many more current and previous lab members for their support and assistance during these years.

I would like to thank my friends Vishal, Kammy, Puneet, Pragya, Avishek, Aishwarya Ajay, Swati, and many others in Waterloo for their continuous support and positive spirit without which I could not have succeeded. Last but not the least; I am very thankful to my wife Mamta not only for her encouragement and support but also for making this process very eventful.

अम्मा और बाबूजी को समर्पित

Dedicated to My Parents

Table of Contents

List of figures……..…xi

List of tables ……..…xx

List of Abbreviations……..…xxiii

Chapter 1. Introduction 1

1.1 Energy Storage 1

1.2 Li-Based Batteries 2

1.2.1 Positive Electrodes 4

1.2.2 Negative Electrodes 24

1.3 Na- Ion Batteries 26

1.4 Scope of the Thesis 31

Chapter 2. Methods and techniques 33

2.1. Introduction 33

2.2. Synthesis Techniques 34

2.2.1. Conventional Tolvothermal Synthesis 34

2.2.2. Microwave Solvothermal Synthesis 35

2.3. Characterization Techniques 36

2.3.1. Diffraction Techniques 36

2.3.1.1. Powder X-ray Diffraction 38

2.3.1.2. Time of Flight Neutron Scattering 40

2.3.2. Structure Refinement 41

2.4. Electron Microscopy 43

2.5. Thermal Analysis 43

2.6. Infrared Spectroscopy 43

2.7. Electrochemical Characterization 44

2.8. Simulation Methods 44

Chapter 3. Synthesis and electrochemistry of Li-transition-metal fluorosulfates 48

3.1. Introduction 49

3.2. Experimental 50

3.2.1. Synthesis 50

3.2.1.1. $MSO_4 \cdot H_2O$ 50

3.2.1.2. Tavorite -Type-$LiMSO_4F$: 50

3.2.1.2.1. Conventional Solvothermal (ST) 51

3.2.1.2.2. Microwave Solvothermal (MW) 52

3.2.1.3 Triplite-Type-$LiMSO_4F$ 53

3.2.1.3.1. Conventional Solvothermal (ST) 53

3.2.1.3.2. Microwave Solvothermal (MW) 53

3.3. Results and Discussion 54

3.3.1. Szomolnokite ($FeSO_4 \cdot H_2O$) 54

3.3.2. Tavorite-Type-$LiMSO_4F$ 55

3.3.3. Triplites-Type-$LiMSO_4F$: 62

3.3.4. Chemical Delithiation of $LiFeSO_4F$ 76

3.3.5. Impact of Moisture Exposure 78

3.3.6. Electrochemistry 80

3.3.6.1. Tavorite-Type-$LiFeSO_4F$ 80

3.3.6.2. Triplite-Type-$Li(Fe,Mn)SO_4F$ 80

3.3.7. Origin of the Voltage Increase: 88

3.3.8. Origin of the Phase Transition 89

3.4. Conclusions 92

Chapter 4. Alkali-ion conduction in tavorite, layered and olivine type structures 94

4.1. Introduction 94

4.2. Method 97

4.3. Results and Discussion 100

4.3.1. Crystal Structure and Potential 100

4.3.2. Intrinsic Atomic Defects 107

4.3.3. Li-ion Migration in Tavorite-Type-$LiFeSO_4F$ 110

4.3.4. Na- ion Migration in Tavorite-Type-$NaFeSO_4F$ 111

4.3.5. Na-ion Migration in Olivine $NaMPO_4$ (M=Fe, Mn, $Fe_{0.5}Mn_{0.5}$) 118

4.3.6. Na-ion Migration in Layerd Na_2FePO_4F 119

4.3.7. Estimation of Diffusion Coefficient..... 125

4.3.8. Electrochemical Behavior *vs.* Ionic Conduction..... 125

4.4. Conclusions 127

Chapter 5. Synthesis and crystal structures of $AMSO_4F$ (A= Na, NH_4, M=Fe, Mn). ... 130

5.2. Experimental 131

5.3. Results and Discussion..... 132

5.3.1. $NaFeSO_4F$ 132

5.3.2. Electrochemistry of $NaFeSO_4F$ 138

5.3.3. $NaMnSO_4F$..... 138

5.3.4. NH_4FeSO_4F and NH_4MnSO_4F..... 142

5.4. Conclusions 149

Chapter 6. Summary And Future Outlook 1**50**

List of publications……154

References ……155

List of Figures

Figure 1.1 Schematic energy diagram in a working Li-ion battery. E_c and E_v represent conduction and valence band of the electrolyte respectively; E_g represents the difference between HOMO and LUMO in the electrolyte; ϕ_c and ϕ_a are the work functions of the cathode and anode respectively and V is the voltage of the cell. SEI represents the solid-electrolyte interface. ……...……..3

Figure 1.2 Various Li-ion cell assemblies: a) cylindrical cell, b) prismatic cell , c) coin cell, and d) a flexible cell made of plastic electrodes and electrolyte..... 4

Figure 1.3 Electrochemical charge-discharge curve of Li_xTiS_2..... 5

Figure 1.4 Electrochemical charge-discharge curve of $Li_xV_2O_5$..... 7

Figure 1.5 V_2O_5 framework transformation on initial Li insertion; red polyhedra represent VO_5 square pyramids. Note that the Li atoms have been removed. Drawn with VESTA using CIF files obtained from ICSD database. 7

Figure 1.6 View of the structures of a) $LiCoO_2$ and b) $LiTiS_2$ along *b*-axis. Black atoms represent Li ions, red-oxygen, yellow-sulfur, blue and cyan - transition metals. 9

Figure 1.7 Electrochemical charge-discharge curve of Li_xCoO_2..... 9

Figure 1.8 Density of states vs. energy diagram of Li_xMO_2..... 10

Figure 1.9 a) Unit cell of spinel $LiMn_2O_4$ projected on a 2-D plane, pink atoms represent Mn, red-O and black-Li; b) framework showing Li –ion diffusion channels. Drawn with VESTA using CIF files obtained from ICSD database..... 13

Figure 1.10 Electrochemical charge-discharge curve of $Li_xMn_2O_4$..... 13

Figure 1.11 Li-Mn-O Phase diagram**.** An expanded view of the phase triangle MnO-Li_2MnO_3-λ-MnO_2 is shown on the right. 14

Figure 1.12 Dependence of Li intercalation voltage on framework and the nature of the polyanion in various phosphates and sulfates. 17

Figure 1.13 Atom distribution in the a) unit cell of olivine $LiFePO_4$, grey atoms are Fe, light pink - P, red-O and black-Li; b) framework showing Li-ion tunnel. Drawn with VESTA using CIF files obtained from ICSD database. 18

Figure 1.14 Electrochemical charge-discharge curve of carbon coated Li_xFePO_4 18

Figure 1.15 Charge-discharge mechanism in a spherical $LiFePO_4$ particle 20

Figure 1.16 Electrochemical charge-discharge curve of carbon coated Li_2FeSiO_4 22

Figure 1.17 Electrochemical charge-discharge curve of $Li_{1+x}FePO_4F$ 24

Figure 1.18 Electrochemical charge-discharge curve of Na_xCoO_2. Inset shows an expanded view of the curve. A 2D projection of the structure of $NaCoO_2$ is also shown. The numbers indicate different phases formed during Na-intercalation 29

Figure 1.19 Electrochemical charge-discharge curve of Na_xFePO_4F 29

Figure 1.20 Electrochemical charge-discharge curve of olivine $Na_xFe_{0.5}Mn_{0.5}PO_4$ 30

Figure 2.1 Conventional solvothermal reaction container setup 34

Figure 2.2 Anton Parr microwave system 37

Figure 2.3 A representative plot for temperature and pressure increase during a microwave reaction. The data was obtained during the reaction using internal probes. 37

Figure 2.4 Bragg scattering of X-rays from a parallel plane of atoms 39

Figure 3.1 X-ray diffraction pattern of $FeSO_4 \cdot H_2O$. Black bars indicate the characteristic peak positions of the pure product derived from the cif file. 55

Figure 3.2 Thermo-gravimetric analysis curve of FeSO4·H2O 55

Figure 3.3 Comparison of szomolnokite and tavorite structures. FeO_6 (in $FeSO_4 \cdot H_2O$) and FeO_4F_2 (in $LiFeSO_4F$) coordination polyhedra are shown in brown. SO_4^{2-} tetrahedra are in yellow. Oxygen atoms are shown in red and fluorine atoms in grey. 57

Figure 3.4 Powder X-ray diffraction refinement of tavorite type $LiFeSO_4F$ prepared *via* conventional solvothermal method. Black points represent experimental data, red solid lines show fitted data while blue lines show the difference map between observed and calculated data. Black bars indicate the phase markers. X-ray diffraction agreement factors*:* $R_{wp} = 8.94\%$, $R_p = 6.95\%$, $R_F^2 = 7.25\%$ 58

Figure 3.5 SEM images of the tavorite type $LiFeSO_4F$ prepared by conventional solvothermal method. 61

Figure 3.6 EDX spectra of $LiFeSO_4F$ 61

Figure 3.7 X-ray diffraction pattern of tavorite $LiFeSO_4F$ prepared *via* microwave solvo-thermal method. Black bars indicate the peak positions for the tavorite phase 63

Figure 3.8 SEM images of the tavorite $LiFeSO_4F$ product obtained by microwave assisted solvothermal method 64

Figure 3.9 X-ray diffraction patterns of LiF and $FeSO_4 \cdot H_2O$ mixture in TEG obtained at different reaction time under conventional solvothermal reaction conditions: a) 2-days of reaction time; b) 7-days of reaction time; b) 14-days of reaction time; d) representation of tavorite crystal structure; f) representation of triplite crystal

structure; FeO_4F_2 octahedra are represented in brown and SO_4 tetrahedra in yellow. 65

Figure 3.10 X-ray patterns of various triplite compounds prepared under conventional solvothermal conditions. 66

Figure 3.11 SEM images of various triplite $LiFe_{1-x}(Mn,Zn)_xSO_4F$ ($0 \leq x < 1$) obtained *via* a conventional solvothermal method; a) and b) triplite $LiFeSO_4F$; c) triplite $LiFe_{0.8}Mn_{0.2}SO_4F$; d) $LiFe_{0.8}Zn_{0.2}SO_4F$ 67

Figure 3.12 Comparison of X-ray diffraction pattern of triplite $LiFeSO_4F$ prepared by a) heating tavorite $LiFeSO_4F$ obtained from microwave synthesis at 350°C for 1 hr under Ar. b) extending conventional solvothermal synthesis for 2 weeks c) heating tavorite $LiFeSO_4F$ obtained by conventional solvothermal at 350°C for 12 hr under Ar. Asterisk (*) represents oxide and sulfide impurity peaks. 68

Figure 3.13 Powder X-ray diffraction refinement of the triplite type $LiFeSO_4F$ obtained by microwave assisted process. Black points represent experimental data, red solid lines show fitted data while blue lines show the difference map between observed and calculated data. Black bars indicate phase markers. X-ray diffraction agreement factors**:** R_{wp} = 3.16%,R_p=1.34%, χ^2 = 3.15**.**. 69

Figure 3.14 SEM images of triplite type $LiFeSO_4F$ obtained by microwave assisted process.. 71

Figure 3.15 Combined X-ray and neutron refinement of $LiFe_{0.8}Mn_{0.2}SO_4F$. Black points represent experimental data, red solid lines show fitted data while blue lines show the difference map between observed and calculated data. Black bars indicate

phase markers. X-ray diffraction agreement factors**:** R_{wp} = 2.33%, R_p = 1.56%, χ^2 = 5.90. 74

Figure 3.16 Refinement of (λ = 0.4122 Å) of $FeSO_4F$ structure from PXRD of $FeSO_4F$ obtained *via* chemical delithiation of tavorite $LiFeSO_4F$. Black points represent experimental data, red solid lines show fitted data while blue lines show the difference map between observed and calculated data; red bars indicate phase markers. X-ray diffraction agreement factors**:** R_{wp}=10.30%,R_p=8.07, R_F^2 = 9.55 .. 77

Figure 3.17 X-ray refinement of moisture exposed triplite $LiFeSO_4F$. Black points represent experimental data, red solid lines show fitted data while blue lines show the difference map between observed and calculated data; Black and red bars represent peak positions for triplite and szomolnokite phases. X-ray diffraction agreement factors: R_{wp} = 2.23%, : R_p = 1.53%, χ^2 = 4.01... 79

Figure 3.18 Electrochemical charge-discharge curve of tavorite type $LiFeSO_4F$ (rate: C/10, active materials 80%, Super P : 20%). Inset shows capacity retention..... 83

Figure 3.19 Electrochemical charge-discharge curve of triplite $LiFe_{0.9}Mn_{0.1}SO_4F$ (rate: C/10, active materials 70%, Super P :30%)..... 84

Figure 3.20 Electrochemical charge-discharge curve of triplite $LiFe_{0.9}Zn_{0.1}SO_4F$ (rate: C/20, active materials 70%, Super P :30%)..... 85

Figure 3.21 Electrochemical charge-discharge curve of triplite $LiFeSO_4F$ prepared *via* microwave assisted synthesis process (rate: C/20, active materials 80%, Super P :20%). Inset shows the capacity retention after cycling..... 86

Figure 3.22 Comparison between electrochemical charge-discharge curve of triplite $LiFeSO_4F$ prepared by extended conventional solvothermal and microwave assisted process (rate: C/20, active materials 80%, Super P :20%)..... 87

Figure 3.23 Differential capacities vs. voltage curves for tavorite and triplite LiFeSO4F. Blue, red and black curves show 2nd , 5th and 10th cycles respectively. 88

Figure 3.24 FT-IR spectra collected for a) tavorite prepared by conventional solvothermal b) tavorite prepared by microwave solvothermal and c) triplite prepared by heating microwave tavorite sample. 91

Figure 3.25 TGA curve for triplite (red) tavorite (blue) $LiFeSO_4F$ 91

Figure 3.26 Comparison of unit cell volumes of tavorite and triplite; b) Phase transition mechanism in MW-$LiFeSO_4F$ 92

Figure 4.1 Schematic illustrating the various Li distances in tavorite $LiFeSO_4F$ along the primary tunnels a). [100] and b). [010]. The preferable Li ion hopping paths are shown where each color belongs to a unique hop with distinct activation energy. Corresponding long range transports within the lattice are shown in c) and d). e) and f) show coordination polyhedra around Li and hopping window for Li-ion migration. The same color code is followed as in (a). 113

Figure 4.2 Schematic showing the various Na-Na distances in $NaFeSO_4F$ along the primary tunnels a) [110] or [-110]. Preferable Na ion hopping paths are depicted in color, where each color belongs to an unique hopping activation energy; b) Corresponding long range transport within the lattice; c) coordination polyhedra

around Na site and corresponding hopping window for Na-ion diffusion. Same color code is followed as in (a). 116

Figure 4.3 Full view of the structure and ion conduction pathways : 3D Li ion conduction in $LiFeSO_4F$. 117

Figure 4.4 Full view of the structure and ion conduction pathways : 1D Na ion conduction in $NaFeSO_4F$ 117

Figure 4.5 a) Unit cell of olivine type $NaFePO_4$ (brown polyhedra: FeO_6 and yellow polyhedra: PO_4) and Na-Na distance along *b*-axis b) tunnel dimensions for olivine $NaFePO_4$ are (numbers in brackets show these lengths for isostructural $LiFePO_4$). c) coordination polyhedra (dark grey) around Na-site and hopping window for long range Na migration along *b*-axis in olivine $NaMPO_4$. 121

Figure 4.6 Na ion migration path along *b*-axis in olivine $NaMPO_4$. Black spheres represent Na atom sites in the olivine structures and most facile pathway for Na-ion hopping is represented by green colored atoms. MO_6 and PO_4 polyhedra are represented in grey and yellow color respectively. 122

Figure 4.7 a) Unit cell of layered Na_2FePO_4F (grey polyhedron: FeO_6 and yellow polyhedron: PO_4) and Na-Na distance (cutoff distance: 4Å) b) Fe and Na layers in layered Na_2FePO_4F. Coordination polyhedron around Na-site in Na_2FePO_4F and examples of hopping window for long range Na migration path c) along *a*-axis; and d) along *c*-axis. 123

Figure 4.8 Na-ion migration path along *a* and *c*-axes in Na_2FePO_4F, octahedra FeO_4F_2 and tetrahedra PO_4 are represented by grey and yellow color respectively. a) along *c*-

axis; long range migration path is formed by combination N4-N3-N6. b) along *a*-axis Na-ions migrate by a combination of N3-N5 hops..... 124

Figure 5.1 a) PXRD pattern of $NaFeSO_4F$. Black points represent experimental data, red solid lines show fitted data while blue lines show the difference map between observed and calculated data. Blue bars indicate the phase markers. X-ray diffraction agreement factors: R_{wp} = 2.91%, R_p = 2.19% χ^2= 2.11 b) unit cell of $NaFeSO_4F$ obtained from the refinement (grey octahedra: FeO_4F_2, yellow tetrahedra: SO_4, red atoms: O, black atoms : Na).. 136

Figure 5.2 Electrochemical charge-discharge curve of tavorite $NaFeSO_4F$ (rate: C/20, active materials 80%, Super P : 20%). ……137

Figure 5.3 a) PXRD pattern of $NaMnSO_4F$ Black points represent experimental data, red solid lines show fitted data while blue lines show the difference map between observed and calculated data. Blue bars indicate the phase markers. X-ray diffraction agreement factors: R_{wp} = 3.49%, R_p = 2.53% χ^2= 2.14. b) unit cell of $NaMnSO_4F$ obtained from the refinement (pink octahedra: (Mn, Na)O_4F_2, yellow tetrahedra: SO_4, pink atoms: Mn, black atoms : Na),..... 141

Figure 5.4 a) PXRD pattern of NH_4FeSO_4F Black points represent experimental data, red solid lines show fitted data while blue lines show the difference map between observed and calculated data. Blue bars indicate the phase markers. X-ray diffraction agreement factors: R_{wp}=4.27%, R_p = 1.92% χ^2= 2.22 b) unit cell of NH_4FeSO_4F obtained from the refinement(grey octahedra: FeO_4F_2, yellow tetrahedra: SO_4, red atoms: O, black tetrahedra :NH_4^+),. 143

Figure 5.5 a) PXRD pattern of NH_4MnSO_4F Black points represent experimental data, red solid lines show fitted data while blue lines show the difference map between observed and calculated data. Blue bars indicate the phase markers. X-ray diffraction agreement factors: R_{wp}=10.13%,R_p=3.48% χ^2 = 2.91 b) unit cell of NH_4FeSO_4F obtained from the refinement (pink octahedra: MnO_4F_2, yellow tetrahedra: SO_4, red atoms: O, black tetrahedra :NH_4^+),..... 146

List of Tables

Table 3.1 Structural data obtained by refinement from powder XRD pattern of the tavorite type $LiFeSO_4F$ prepared *via* conventional solvothermal methods..... 59

Table 3.2 Bond lengths obtained by refinement from powder XRD pattern of tavorite $LiFeSO_4F$ prepared *via* conventional solvothermal methods..... 60

Table 3.3 Structural data obtained by refinement from powder XRD pattern of triplite $LiFeSO_4F$……72

Table 3.4 Summary of bond lengths obtained by refinement from PXRD of triplite-type-$LiFeSO_4F$ 73

Table 3.5 Refined structural parameters of $LiMnSO_4F$, $LiFe_{0.5}Mn_{0.5}SO_4F$, $LiFe_{0.8}Mn_{0.2}SO_4F$ and $LiFe_{0.9}Mn_{0.1}SO_4F$. Rietveld analyses of powder neutron and X-ray diffraction data were done in the *C2/c* space group with all atoms in general positions..... 75

Table 3.6 Structural data of $FeSO_4F$ synthesized by chemical delithiation of tavorite type $LiFeSO_4F$ 78

Table 4.1 Short range potential parameters for tavorite ($LiFeSO_4F$ and $NaFeSO_4F$)..... 99

Table 4.2 Short-Range Potential Parameters for olivine type $Na[Fe,Mn]PO_4$ and layered Na_2FePO_4F 100

Table 4.3 Calculated and experimental structural parameters for $AFeSO_4F$ (A=Li, Na) 102

Table 4.4 Calculated and experimental structural parameters for layered Na_2FePO_4F and olivine type $NaFePO_4$..... 103

Table 4.5 Comparison of selected bond lengths of experimental and calculated tavorite $LiFeSO_4F$ structure 104

Table 4.6 Comparison of selected bond lengths of experimental and calculated tavorite $NaFeSO_4F$ structure 105

Table 4.7 Comparison of selected bond lengths of experimental and calculated layered Na_2FePO_4F structure 106

Table 4.8 Comparison of selected bond lengths of the experimental and calculated olivine $NaFePO_4$ structure..... 107

Table 4.9 Energies of formation of intrinsic defects in $AFeSO_4F$ (A=Li, Na): 108

Table 4.10 Energies of formation of intrinsic defects in Na_2FePO_4F and $NaFePO_4$ 110

Table 4.11 Calculated activation energies for most favorable paths of alkali ion migration in $LiFeSO_4F$ 112

Table 4.12 Calculated activation energies for most favorable paths of alkali ion migration in $NaFeSO_4F$ 113

Table 4.13 Calculated activation energies for most favorable paths of alkali ion migration in Na-olivines 120

Table 4.14 Calculated activation energies for the most favorable paths of alkali ion migration in layered Na_2FePO_4F. 122

Table 5.1 Structural data obtained by refinement from powder XRD pattern of tavorite type $NaFeSO_4F$..... 134

Table 5.2 Selected bond lengths obtained by refinement from powder XRD pattern of tavorite type $NaFeSO_4F$ 135

Table 5.3 Structural data obtained by refinement from powder XRD pattern of triplite type $NaMnSO_4F$ 139

Table 5.4 Selected Bond lengths obtained by refinement from powder XRD pattern of triplite type $NaMnSO_4F$ 140

Table 5.5 Structural data obtained by refinement from powder XRD pattern of NH_4FeSO_4F 144

Table 5.6 Selected bond lengths obtained by refinement from powder XRD pattern of triplite NH_4FeSO_4F 145

Table 5.7 Structural data obtained by refinement from powder XRD pattern of NH_4MnSO_4F 147

Table 5.8 Selected bond lengths obtained by refinement from powder XRD pattern of NH_4MnSO_4F 148

List of Abbreviations

XRD	X-ray diffraction
PXRD	Powder X-ray diffraction
TOF	Time of flight
TEG	Tetraethylene glycol
MW	Microwave
ST	Solvothermal
MWST	Microwave solvothermal
SEM	Scanning electron microscope
EDX	Energy dispersive X-ray spectroscopy
FTIR	Fourier transform infrared spectroscopy
NSF	Sodium Iron Fluorosulphate ($NaFeSO_4F$)
LSF	Lithium Iron Fluorosulphate ($LiFeSO_4F$)
MWLSF	Microwave prepared Lithium Iron Fluorosulfate ($LiFeSO_4F$)
STLSF	Lithium Iron Fluorosulfate ($LiFeSO_4F$) by conventional solvothermal heating
a, b, c	Crystallographic axes
E_a	Activation energy
SG	Space group

Chapter 1

Introduction

1.1 Energy Storage

Due to an increased emphasis on the production and use of pollution free energy along with the tremendous growth pattern in many developing countries, the demand for electrical energy storage is projected to double by 2050.[1] The current energy distribution and storage system will not be able to fulfill these requirements. Additionally, fossil fuel based energy sources create environmental problems and now it is widely recognized that any future energy scenario must exclude environmentally unfavorable options.[2] Nuclear energy is increasingly recognized as unsafe, and geothermal energy can be harnessed only at certain locations. The most abundant and unused energy sources are wind and solar energy but they need to have a strong backup of energy storage to become a reliable source of supply. Energy storage will be required in a modern grid system for load leveling. Powerful energy storage systems are also needed to power the next generation of electric and hybrid electric vehicles. Here, the requirement is urgent due to the threats of environmental instability. Each of these requirements imposes certain restrictions on the mode and methods of energy storage. Unlike mobile devices, grid scale storage places less emphasis on the energy stored per unit of weight,[3] but stability requirements are more stringent. A long stable life, high specific energy density and lower cost are all considerations that must be explored for the replacement of fossil fuel driven automobiles.[1]

Technological innovations, in combination with fundamental scientific discoveries of the last two decades, have created an enormous change in energy storage and how it is used in our

daily life. Today, all electronic gadgets are powered by batteries. Indeed, it is the success of batteries in small scale energy storage which has caused them to be looked upon as the likely, and perhaps the only, solution to the current energy storage crisis.

Among these, Li-ion batteries currently dominate the energy storage market because of their light-weight and high specific energy density. Na-ion batteries operate on the similar principle as Li-ion and they are projected as the best candidates for the grid scale storage. The development of some of the positive and negative electrodes for these battery systems are described below.

1.2 Li-Based Batteries

The most electropositive and the lightest metal in the periodic table, lithium is found in nature in the form of two isotopes ^{6}Li and ^{7}Li. The most abundant isotope ^{7}Li is about 92.5% of all atoms. Lithium has high mobility in many inorganic solids and can be easily and reversibly intercalated in many complex 1-D, 2-D and 3-D structures. In a Li-metal battery (or Li-battery), the negative electrode is Li metal and the positive electrode is generally a crystalline material which can reversibly intercalate Li^{+} ions. Li is deposited or stripped from the negative electrode during the charge and discharge. In a Li-ion battery, both the electrodes are intercalation materials. Electrolytes generally contain a Li-salt in an organic solvent to ensure good conductivity of Li-ions as well as wide electrochemical stability window. **Figure 1.1** demonstrates schematic energy diagram in the electrodes and the electrolyte of a Li (ion) cell. The difference between HOMO and LUMO electronic states of the electrolyte provides a region where no electron transfer can take place between electrodes and the electrolyte which is an essential criteria for the thermodynamic stability of the cell.[4] This means that the Fermi level of the electrodes must lie within the this gap E_g of the electrolyte (**Figure 1.1**). Therefore, the maximum voltage of a Li (ion) cell is limited by the electrolyte and determined by the Fermi

energy level of the electrodes. The difference between the Fermi level (or work function) of the two electrodes is the voltage of the cell (e is the magnitude of electronic charge and ϕ the work function):

$$\Delta V = (\phi_{positive\text{-}electrode} - \phi_{negative\text{-}electrode})/e$$

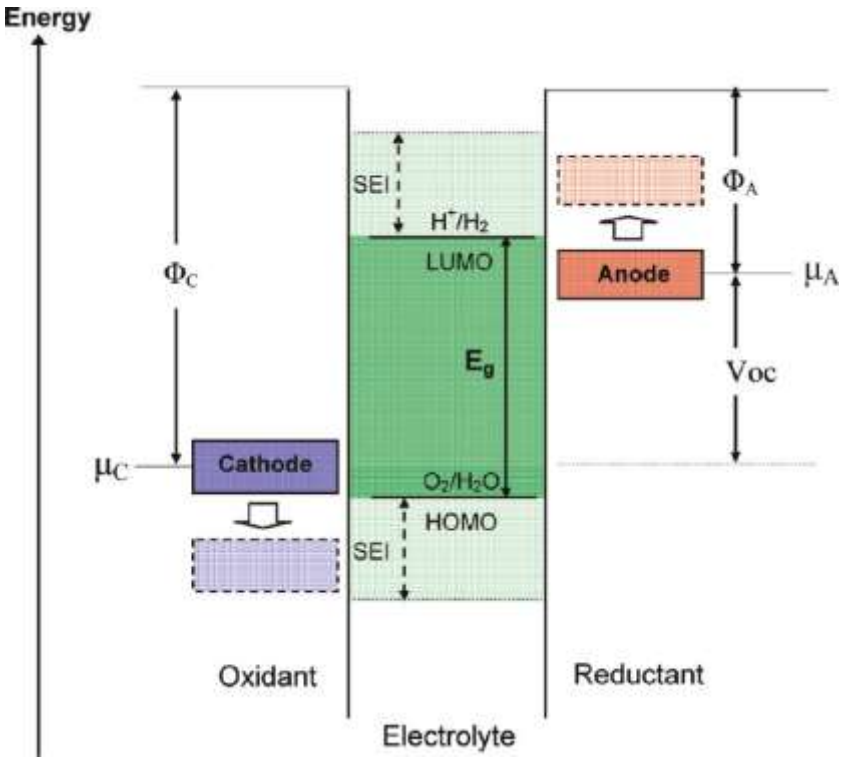

Figure 1.1 Schematic energy diagram in a working Li-ion battery.4 E_c and E_v represent conduction and valence band of the electrolyte respectively; Eg represents the difference between HOMO and LUMO in the electrolyte; ϕ_c and ϕ_a are the work functions of the cathode and anode respectively and V is the voltage of the cell. SEI represents the solid-electrolyte interface.

As shown in **Figure 1.2,** Li-ion cells can be assembled in cylinder, prism and coin geometries. Plastic Li-ion technology provides the added advantage of flexibility. The following

sections provide a detailed structural and electrochemical description of the Li-ion battery electrode materials with added emphasis on the positive electrode.

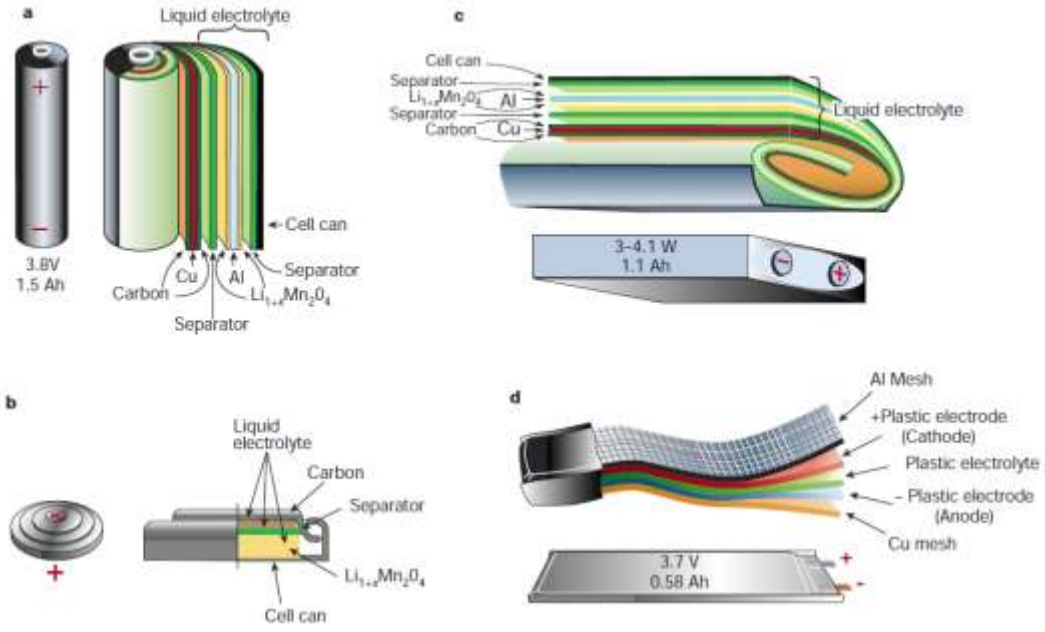

Figure 1.2 Various Li-ion cell assemblies[5]: a) cylindrical cell, b) prismatic cell , c) coin cell and, d) a flexible cell made of plastic electrodes and electrolyte

1.2.1 Positive Electrodes

Intercalation chemistry is at the root of the current generation of Li-ion batteries. Intercalation based positive electrodes were first developed during the early 1970s. It was observed that the electron donating elements, such as lithium could be intercalated in chalcogenides (MS_2, M=Ta, Ti) and it leads to change in the properties of the compound.[6] TiS_2 was better choice due to its lighter weight and semiconductor properties.[7,8,9,10] TiS_2 adopts hexagonal anion packing, and Ti is located in the octahedral site between alternating sulfur sheets. The structure is stabilized by partial covalent character of S and van der Waals forces

between S-S layers. Intercalation of the Li-ion reversibly occurs over the whole composition range Li_xTiS_2 ($0 \leq x \leq 1$) in a single phase reaction.[11] Such electrochemical results are normally reported in a charge-discharge curve as shown in **Figure 1.3**. The ease of intercalation permitted deep discharge over 1000 cycles with less than 0.05% loss in each cycle. Exxon marketed this technology with LiAl negative electrode and TiS_2 positive electrode as button cells. The competitive disadvantage of a Li-battery with TiS_2 as the positive electrode material soon became clear after it was revealed that Li forms dendrites on the negative electrode side upon cycling which leads to unsafe battery operation. Replacement of the Li-metal as the negative electrode meant that the voltage of the full cell with TiS_2 positive electrode was low and the specific energy density lower than the Ni-Metal hydride system. Later Haering *et al.* [12] introduced modified layered MoS_2 structure in the market and Moli energy commercialized Li-cells based on these positive electrode.

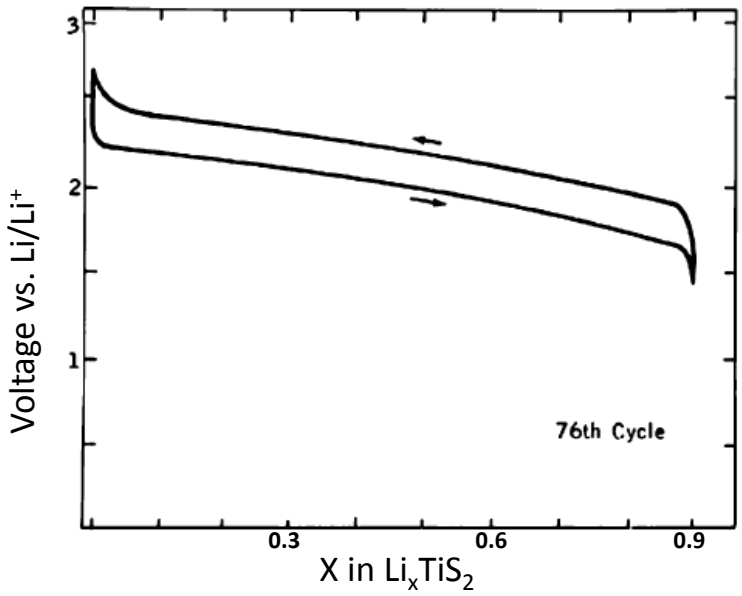

Figure 1.3 Electrochemical charge-discharge curve of Li_xTiS_2[13]

TiS_2 is a semiconductor and therefore the Fermi energy level of the compound is very close to the top of the valence band (S^{2-} : $3p^6$). One way to increase the voltage of the cell is to replace Ti with transition metals that display lower Fermi level. This can be achieved by using high valence redox couples. However, high valence chalcogenides of first row transition metals are not stable. As an alternative, the subsequent decade saw the development and commercialization of the Li-ion battery system based on layered oxides which are described below in detail.

Layered V_2O_5 was the first oxide positive electrode investigated for intercalation of Li ions[11,14,15] in 1976 and since then it has remained an active area of research for many research groups across the world. The gravimetric capacity of this compound is very high due to low molecular weight of the compound. Substantial structural changes are observed as Li is intercalated in the structure (V_2O_5 => $Li_xV_2O_5$) and these are summarized in the charge-discharge curve of **Figure 1.4**. The initial α-phase ($x < 0.1$) changes to the ε-phase as intercalation progresses ($0.35 < x < 0.7$) and at $x = 1$ the structure changes to the δ polymorph. Intercalation beyond one lithium irreversibly transforms the structure to the γ phase (for $x \leq 2.0$). $Li_3V_2O_5$ adopts yet another structure (rock salt type) known as the ω-phase[14] (**Figure 1.4** and **Figure 1.5**). This latter phase can intercalate 3 Li atoms reversibly and displays solid solution behavior over the whole intercalation range. However all of these phases show poor capacity retention upon cycling.

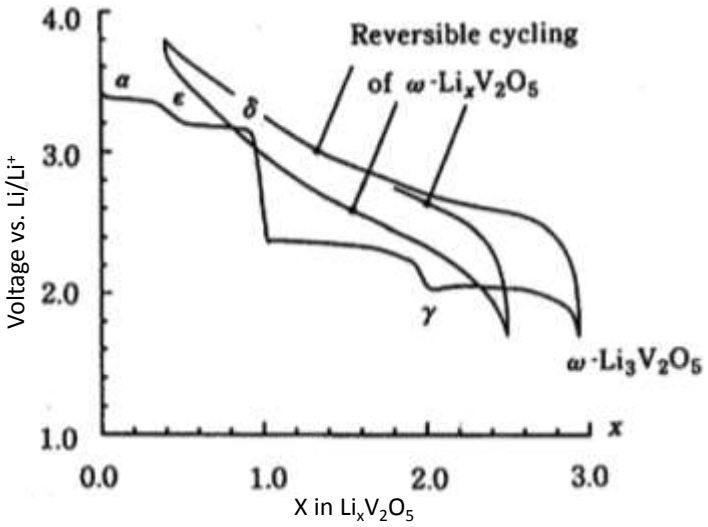

Figure 1.4 Electrochemical charge-discharge curve of $Li_xV_2O_5$.[14]

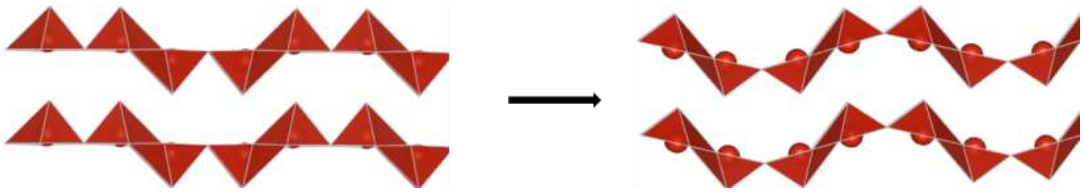

Figure 1.5 V_2O_5 framework transformation on initial Li insertion; red polyhedra represent VO_5 square pyramids. Note that the Li atoms have been removed. Drawn with VESTA using CIF files obtained from ICSD database.

Layered lithium transition metal oxides (e.g. $LiCoO_2$) adopt cubic packing of the anions. The Li^+ ions occupy the octahedral sites between the anion sheets similar to $LiTiS_2$. Among all the transition metal analogues, $LiCoO_2$[16] adopts the most cation ordered structure. The layered $LiFeO_2$ cannot be directly synthesized and $LiNiO_2$ forms with considerable cation disorder which negatively impacts its electrochemical performance. Goodenough *et al.* proposed $LiCoO_2$ as the positive electrode for Li (ion)-batteries in 1980 (**Figure 1.6** and **Figure 1.7**). Substantial rearrangement of the anion stacking occurs upon Li-removal from $LiCoO_2$. The initial

delithiation is followed by an elongation in the interlayer *c*-axis due to an increased repulsion among the oxygen layers.[17,18,19] Subsequently an order-disorder transition occurs[19] at x ≈ 0.5 and the final transition occurs through an intermediate $Li_{0.12}CoO_2$.[20,21] The half-lithiated composition $Li_{0.5}CoO_2$ can also form as a metastable spinel phase and traces of the spinel phase are seen after extensive cycling.[22] Almost completely delithiated material $Li_{0.05}CoO_2$ adopts a TiS_2-like structure.[23] Although full Li-extraction from $LiCoO_2$ gives a very high gravimetric capacity, only approximately half of that is reversible due to the instability of the completely delithiated structure. The capacity loss upon cycling is substantial after extraction of more than 70% lithium. The SONY corporation commercialized this technology[24,25] in 1990.

In 2005-06 several batteries were reported to catch fire during operation and the SONY corporation announced that it would recall about 340,000 batteries due to safety fears.[26] One of the main reasons, for this incident, was found to be the loss of oxygen from the lattice framework of $LiCoO_2$ on deep charge followed by the reaction between the electrode and the electrolyte.[27,28] The incident highlighted an important drawback in the cobalt based layered metal oxides. As the Co (electronic configuration: $3d^6 : t_{2g}^6 e_g^0$) is oxidized, because of the closeness of the "t_{2g}" level of the metal and "p" level of the oxygen (**Figure 1.8**), the oxygen starts giving up the bonding electron and migrates to the surface[29] where it may react with the electrolyte at higher temperatures.[30,31,32] A study done by Chembiam *et al.*[29] indicates that no oxygen evolution occurs until the average Co oxidation state reaches 3.35 after which the extraction of Li is not accompanied by the increase in the oxidation state, indicating a loss of oxygen from the lattice. Therefore, to maintain the chemical stability, $LiCoO_2$ cannot be fully charged.

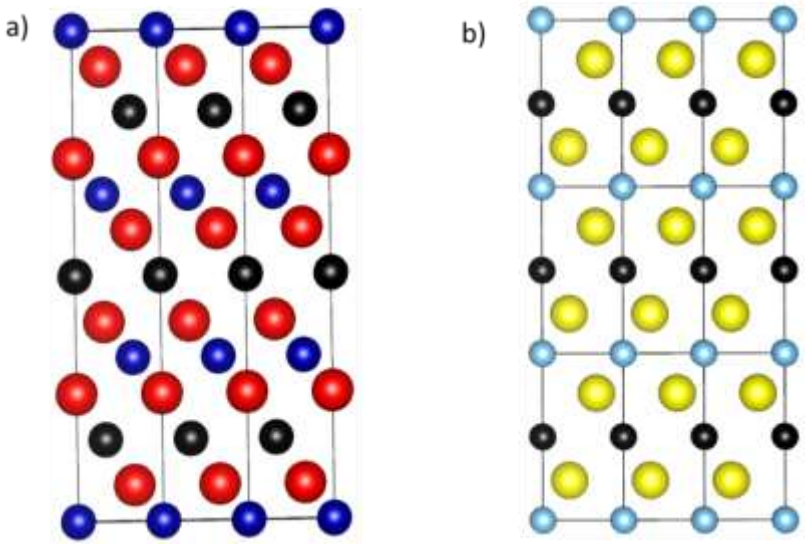

Figure 1.6 View of the structures of a) $LiCoO_2$ and b) $LiTiS_2$ in a plane perpendicular to *b*-axis. Black atoms represent Li ions, red-oxygen, yellow-sulfur and blue and cyan - transition metals. Drawn with VESTA using CIF files obtained from ICSD database.

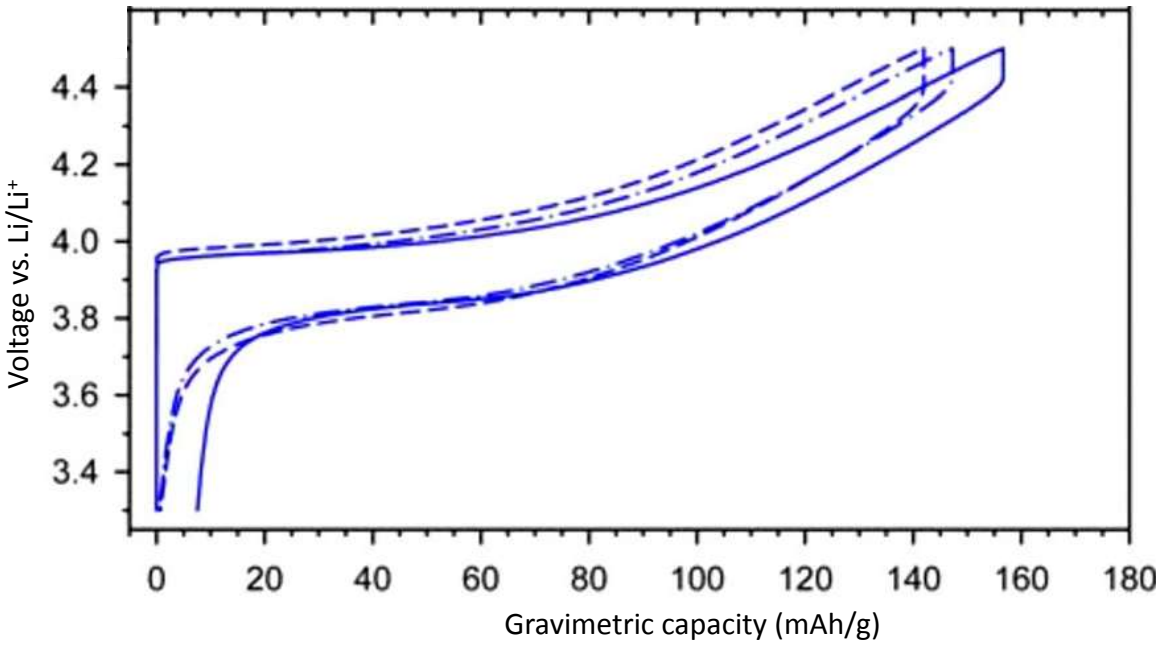

Figure 1.7 Electrochemical charge-discharge curve of Li_xCoO_2[33]

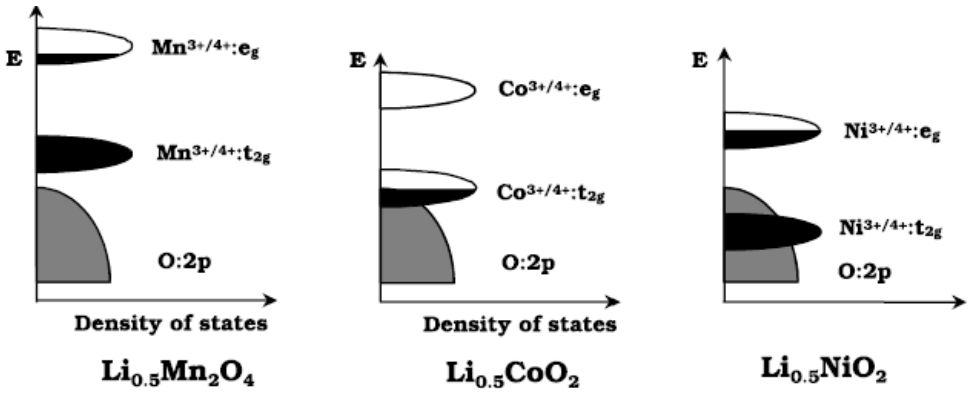

Figure 1.8 Density of states *vs.* energy diagram of Li_xMO_2[29]

To remove the oxidative instability associated with the Co-based compounds it was suggested that compounds, in which either "t_{2g}" band is much above "p" band of oxygen (ex.: Mn) or electron population is higher (ex : Ni), should be used instead of Co. Ni^{3+} ($3d^7$) has one electron ($t_{2g}^6e_g^1$) in the e_g orbital in the low spin configuration (**Figure 1.8**) which is higher in energy than the O-2p level and therefore oxygen is not released from the lattice framework even under deep-charge conditions. However, pure $LiNiO_2$ is slightly cation disordered when synthesized using conventional methods due to the tendency of Ni-ions to enter the Li-layer which effectively reduces the Li-diffusion coefficient and hence adversely impacts the power capability of the cell.[34] The Co and Al substituted $LiNiO_2$ have been studied in more detail where Co prevents the Ni migration to the Li-layer and Al is electrochemically inactive preventing the complete removal of the Li.[35] Study of the samples obtained *via* chemical delithiation of $LiNi_{0.85}Co_{0.15}O_2$ show a linear increase of the oxidation state of the Ni with the degree of Li-extraction from the sample providing strong evidence that the oxygen evolution does not occur in this system until very low lithium content.[29] However thermal stability of the charge material in both cases ($LiNiO_2$ and $LINi_{0.8}Co_{0.2}O_2$) has been shown to be much lower

than charged $LiCoO_2$.[36] Manganese is abundant in nature and costs less than 1% of Co, hence Li containing manganese oxides are some of the least expensive positive electrode materials. However, ordered-layered $LiMnO_2$ could only be synthesized by ion-exchange[37] from the isostructural $NaMnO_2$.

$LiNi_xMn_xCo_{2-x}O_2$ (NMC) is a high capacity and high voltage electrode material with excellent safety characteristics. In particular, the material, $LiNi_{1/3}Mn_{1/3}Co_{1/3}O_2$[38,39] has become one of most successful positive electrode material for Li-ion batteries. In this compound, the oxidation states of Ni, Co and Mn are 2+, 3+ and 4+ respectively. Such oxidation state distribution leaves Mn inactive during the charge process; Ni^{2+} oxidizes to Ni^{4+} upon charge and Co^{3+} becomes Co^{4+}; thus enabling the removal of one lithium per transition metal on average.[40,41] This leads to a very high reversible capacity. In addition, Mn^{4+} acts as a pillar in the structure and only a maximum unit cell volume expansion of 2% is observed after the removal of 70% lithium.[42,43] Induction of Co in the structure reduces cation disorder and an excellent rate capability is observed.[41,44,45,46,47,48] The charged material shows very good tolerance towards oxygen release[49,50] which makes it a very safe material. NCM positive electrodes are being rapidly commercialized in the current generation of Li-ion batteries.

Like lithium containing layered oxides, spinels (general composition: AB_2X_4) also form with cubic close packing of the anions and the cations occupy either the octahedron (cation B) or tetrahedron (cation A) site. Thackeray *et al.* have studied[51,52,53,54] these compounds (ex: Fe_3O_4, Mn_3O_4 and $LiMn_2O_4$) in great detail and the main conclusions are as following:

1. Li can be reversibly inserted in Fe_3O_4 (inverse spinel). The Intercalated Li-ion occupies the empty octahedral site (16c) and displaces Fe^{3+} ions from the tetrahedral (8a) site to

empty octahedral site (16c) but the Fe_3O_4 framework of the spinel structure remains intact.

2. The interstitial space formed by the Fe_3O_4 framework and comprising of vacant octahedral and tetrahedral sites provides a 3-D conduction pathway for the Li-ions
3. Li intercalation in Mn_3O_4 follows a similar process and $LiMn_3O_4$ is isostructural to $LiFe_3O_4$.
4. Li can also be intercalated in $LiMn_2O_4$ (**Figure 1.9**). However, unlike Fe_3O_4, intercalation of the additional lithium on the neighboring octahedral site does not lead to any site reconfiguration in the parent framework. Electrochemically this process occurs at 3 V (Mn^{4+}/Mn^{3+}, **Figure 1.10**). However, the cooperative Jahn-Teller distortion forces phase separation in the system beyond the intercalation of 0.2 Li.[52]

Hunter *et al.* reported direct formation of the Mn_2O_4 spinel framework (λ-MnO_2) obtained by acid treatment of $LiMn_2O_4$ in 1981.[55] This study proved that tetrahedrally coordinated Li can be topotactically removed from the spinel-$LiMn_2O_4$. Electrochemically, this process occurs at 4 V. Two different voltages for the same active redox couple ($Mn^{3+/}Mn^{4+}$) in the spinel-$LiMn_2O_4$ underline the role of Li-coordination in determining the voltage **(Figure 1.10)**. Subsequently, $LiMn_2O_4$ has been studied[56,57,58,59] with great interest by various groups due to the ease of its synthesis, environmental benignity and abundance of Mn in nature. However, after long term cycling, some problems occur which are described below:

1. Dissolution of the Mn from the spinel, particularly if the electrolyte is slightly acidic. Since only Mn^{2+} ions dissolve under acidic conditions, the process is expected to occur *via* disproportion reaction of Mn^{3+} to Mn^{2+} and Mn^{4+}.
2. Delithiated spinel is unstable in the presence of the organic electrolyte.

3. Overcharge during the cycling can lead to excess of Mn^{3+} on the surface and hence a strained structure due to Jahn-Teller distortion of the Mn^{3+}.

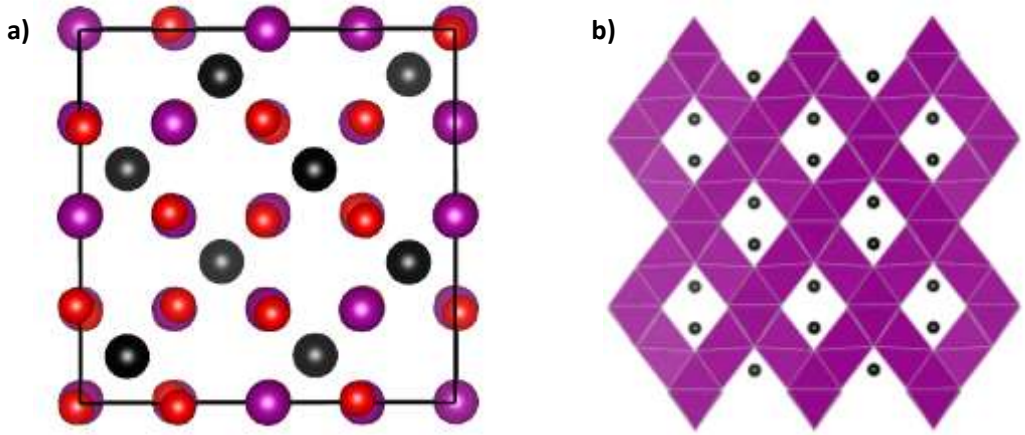

Figure 1.9 a) Unit cell of spinel $LiMn_2O_4$ projected on a 2-D plane, b) framework showing Li –ion diffusion channels (projected along [110]). Pink atoms represent Mn, red-O and black-Li Drawn with VESTA using CIF files obtained from ICSD database.

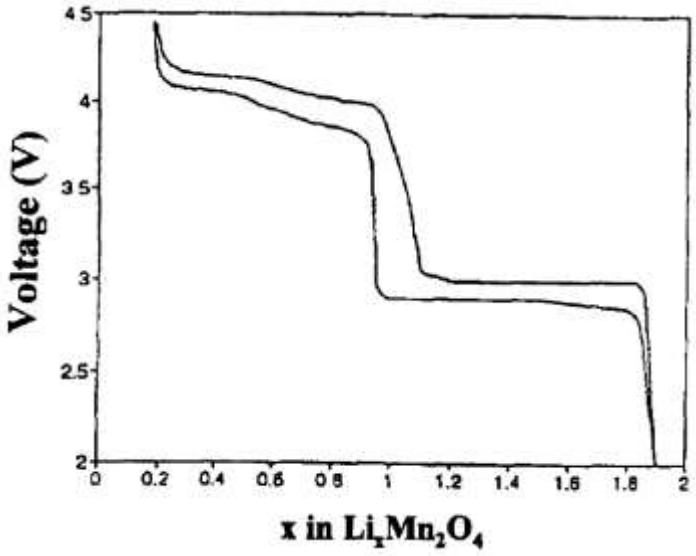

Figure 1.10 Electrochemical charge-discharge curve of $Li_xMn_2O_4$[60]

To avoid the problems associated with Jahn-Teller distortion, substitution of Mn^{3+} by subvalent cations has been extensively explored. Substitution with divalent cations such as Mg,[61] Zn,[61] Co[62] and Ni[63, 64, 65] in $LiMn_2O_4$ reduces the amount of Mn^{3+} in the material and hence the 4 V capacity of the material decreases. Doping of more than 50% divalent cation forces all the Mn to the tetravalent form and hence no Li can be extracted from these compounds. However the composition $LiMn^{IV}_{1.5}Ni^{II}_{0.5}O_4$ displays an interesting electrochemical activity at 4.7 V. Subsequent investigations have revealed that this voltage plateau can be attributed to direct oxidation of the Ni^{2+} to Ni^{4+}.[64] Li substitution on the Mn site yielding the general chemical formula Li $[Mn_{2-x}Li_x]O_4$ has been reported to successfully stabilize the capacity retention with slightly less capacity.[61]

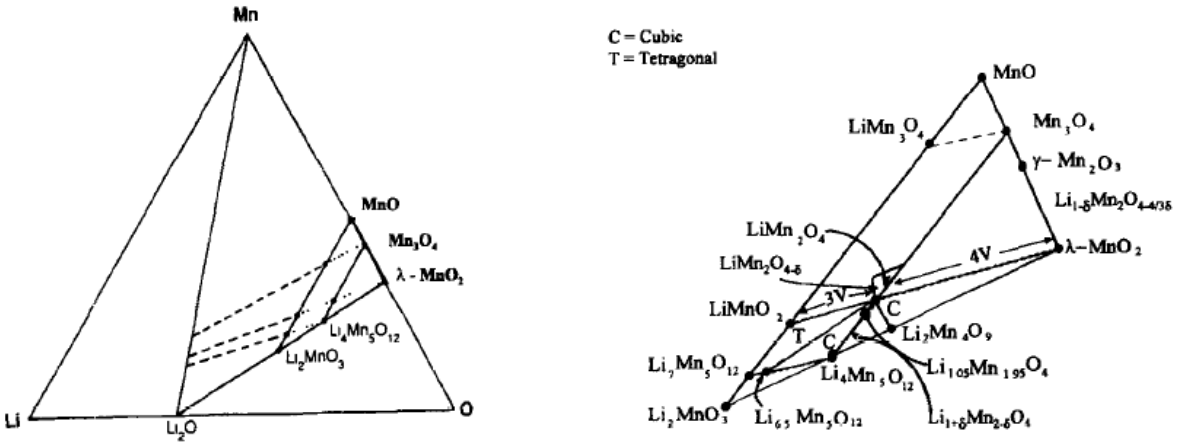

Figure 1.11 Li-Mn-O Phase diagram.[60] An expanded view of the phase triangle MnO-Li_2MnO_3-λ-MnO_2 is shown on the right.

Figure 1.11 shows the Li-Mn-O phase diagram with an expanded view of the important phases displayed on the right taken from the work of Thackeray *et al.*[60] The phases on the tie line formed by connecting the compounds Li_2O and MnO_2 are of particular interest. Closer to the MnO_2 compound is $Li_4Mn_5O_{12}$ or Li $[Mn_{(2-1/3)}Li_{1/3}]O_4$ i.e. a Li-rich spinel with only tetravalent

Mn ions. This material can be discharged to $Li_{6.5}Mn_5O_{12}$ at 3 V. Li_2MnO_3 is another important composition in the Li_2O-MnO_2 (1 $Li_2O\cdot$ 1 MnO_2) tie line. It shows interesting electrochemical activity upon charge to 4.6 volts despite the fact that all of the Mn is in the tetravalent state. The compound can be classified as possessing an ordered rock salt type structure. However due to cationic ordering the structure is classified in monoclinic space group *C*2/*c*.[66] Unusual electrochemical activity has been reported due to the release of oxygen from the structure, which is an irreversible process.

Iron-based compounds are amongst the cheapest and some of the least toxic materials, and therefore best suited, for large scale energy storage (electric vehicles and grid scale). The difficulty of synthesizing the layered $LiFeO_2$ and an impractically high voltage of the Fe^{3+}/Fe^{4+} redox couple in these compounds prompted Goodenough *et al.* to investigate[67,68,69] various polyanion based iron compounds for Li intercalation during 1990s with the general formula $Li_aFe_b(XO_4)_c$ (X=S, P). Based on the electrochemical and structural characterization of several Fe-based phosphates and sulfates, the following rules were suggested for mapping the redox energy (voltage) of Fe^{2+}/Fe^{3+} couple in a polyanion based compound:

1. $(XO_4)^{n-}$ polyanion based compounds adopt framework structures which provide facile channels for Li ion conduction.
2. In a given framework, as covalent mixing at the iron from Fe-O bond decreases, the energy of the corresponding redox couple also decreases causing an increase in the voltage. Therefore, the energy of a given redox couple can be tuned by selecting the appropriate X cation. As the electronegativity of the X cation increases, the transition metal faces more competition for covalent mixing with oxygen. As a result, when

phosphates are replaced by sulfates and if this is not accompanied by a change in the structure, an increase of 0.8 V is observed for $Li_aFe_b(XO_4)_c$ compounds (**Figure 1.12**).

3. The redox energy can also be tuned by changing the Fe-O-X connectivity (i.e. changing framework, **Figure 1.12**).
4. Introduction of the polyanion in the framework increases the distance between transitional metal atoms resulting in a decreased electronic conductivity.
5. $LiFePO_4$ crystallizing in the olivine type mineral framework displays the highest redox voltage (Fe^{2+}/Fe^{3+}) among all Fe-phosphate frameworks.

The olivine type M_2XO_4 structure has M atoms in half of the octahedral sites and X atoms in $1/8^{th}$ of the tetrahedral sites in a hexagonally close packed lattice of oxygen atoms (**Figure 1.13**). Therefore it is the HCP analogue of $X[M_2]O_4$ spinels. For smaller X cations such as P^{5+}, B^{3+} and Si^{4+} the olivine type structure is preferred over the spinel type. In $LiFePO_4$, cation-cation Coulombic repulsion causes a distortion of the HCP array of anions. Fe forms a chain of corner shared FeO_6 octahedra along the *c*-axis and shares 2 edges with LiO_6 octahedra. It also shares one edge with the PO_4 tetrahedra.

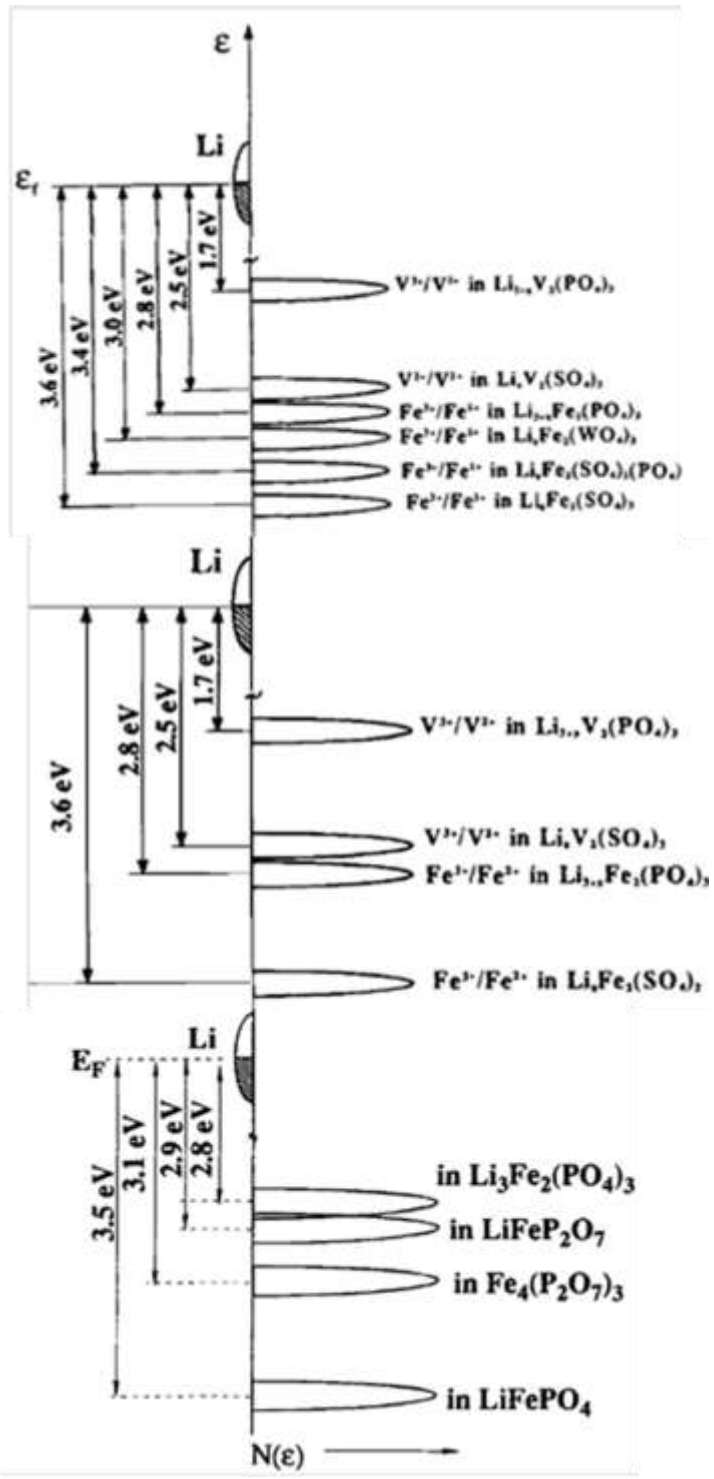

Figure 1.12 Dependence of Li intercalation voltage on framework and the nature of the polyanion in various phosphates and sulfates. [67,69]

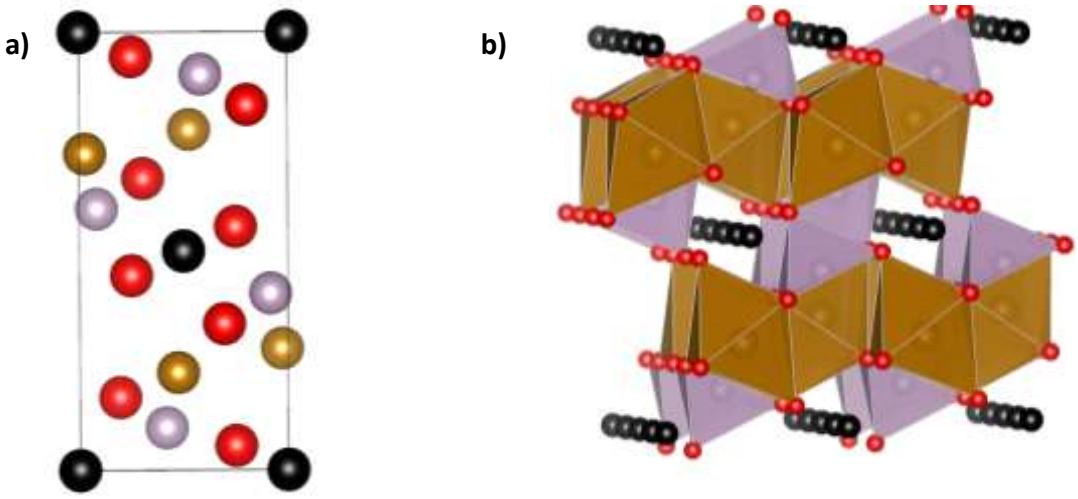

Figure 1.13 Atom distribution in the a) unit cell of olivine $LiFePO_4$, b) framework showing Li-ion tunnels. Grey atoms represent Fe, light pink- P, red-O and black-Li; Drawn with VESTA using CIF files obtained from ICSD database.

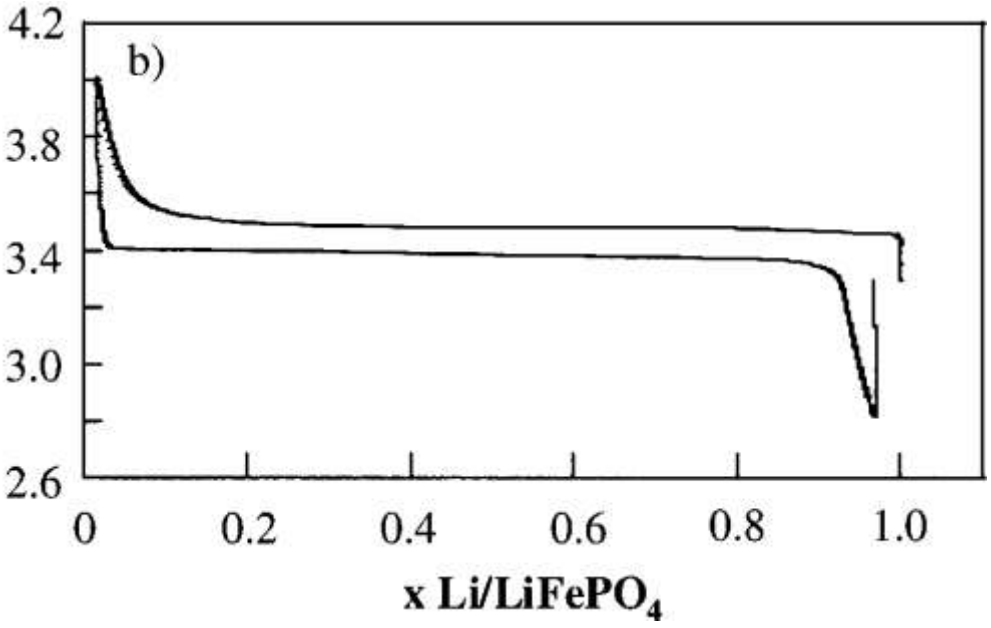

Figure 1.14 Electrochemical charge-discharge curve of carbon coated Li_xFePO_4.[70]

Initially $LiFePO_4$ was predicted to be a replacement electrode in batteries only for low power applications due to its poor electronic and ionic conductivity. However, this material has displayed some of the highest charge and discharge rates, achieved by post processing of the material to either tune the electronic or the ionic conductivity.[70] These and many other interesting properties of $LiFePO_4$ have been followed with a great interest in the past decade resulting in more than 3000 peer-reviewed publications. The main discoveries and ensuing discussions are summarized below:

1. The intrinsic material can be coated with a conductive carbon by using organic precursors[71,72,73]or conductive inorganic materials[74] during the synthesis. The coated material displays much better reversible gravimetric capacity and power capability.[75] The positive effect is mainly attributed to the increased electronic conductivity.
2. Better electrochemical properties can also be obtained by reducing the primary particle size.[76] This results in a shorter Li-diffusion distance and hence improved kinetics of the de/-intercalation process.[77]
3. Charge conduction in the material occurs through a polaron-hopping[78] mechanism and the olivine type structure restricts ion-conduction to only one direction.[79] However, the presence of defects can force 2-D ion conduction in the material.[80]
4. Li-intercalation in the micro-sized material occurs *via* two phase boundary formation with $FePO_4$ and $LiFePO_4$ phase separating after 5-10% Li de/-intercalation (**Figure 1.15**).[81,82] Miscibility of the two phases can be increased by reducing the particle size and below ~50nm, these are completely miscible in to each other.[83,84] Complete miscibility can also be achieved by raising the

temperature to above 350°C. Some reports also suggest that a dynamic intercalation process occurs through a non-equilibrium path which does not involve formation of two separate phases.[85]

5. $LiMnPO_4$ also crystallizes in the olivine type structure and charge-discharge in this compound occurs at an average of 4.1 V.[86] However the electronic and ionic conductivity is poorer than $LiFePO_4$.[87]
6. Mixed olivines $LiFe_{1-x}Mn_xPO_4$ have also been studied in good detail due to higher theoretical specific energy density. $LiFe_{0.2}Mn_{0.8}PO_4$, recently[88] has been demonstrated to be a high specific energy density positive electrode material with a very stable cycling capacity. High power density was also achieved for carbon coated material.[88]

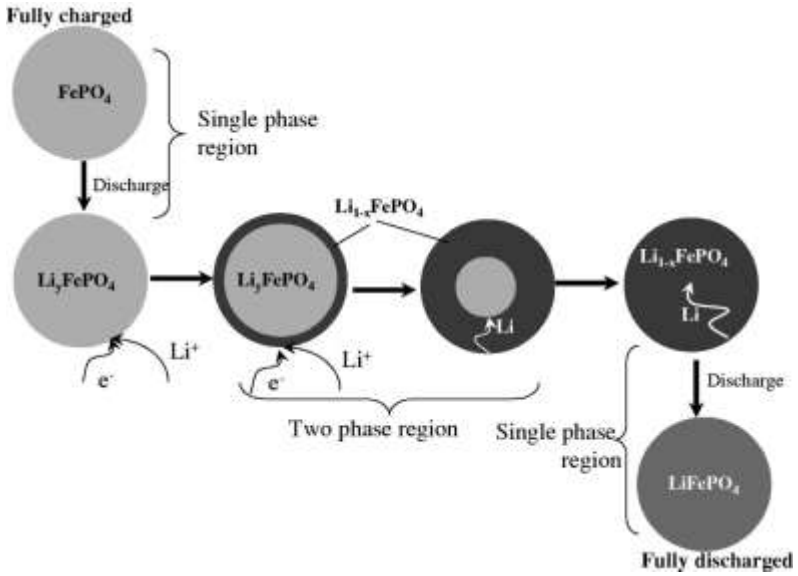

Figure 1.25 Charge-discharge mechanism in a spherical $LiFePO_4$ particle[89]

Silicates are abundant materials in the earth's crust and easily form various transition metal silicates.[90] Due to higher charge/weight ratio, polyanionic materials with $(SiO_4)^{-4}$ as the anion

group provide higher specific energy density than phosphates of similar composition.[91] In addition, common lithium transition metal silicates of general composition Li_2MSiO_4 (M= transition metal), accommodate two lithium per transition metal. Therefore, theoretical gravimetric capacity is very high. However, the voltage for Li_2FeSiO_4 is lower than $LiFePO_4$ because of the inductive effect and a different framework. During the last decade, the silicate compositions Li_2FeSiO_4 and Li_2MnSiO_4 have been studied in great detail. Li_2MSiO_4 (M=Fe, Mn) adopt tetrahedral structures based on the framework of the Li_3PO_4 type (β or γ).[92] These structures are made by distorted HCP packing of the oxides (tetragonal packing) within which half of the tetrahedral sites are occupied by Li and transition metals such that no two tetrahedra share faces with each other.[93]

Li_2MSiO_4 frameworks can be broadly divided into the β and γ-types. The main conclusions regarding their polymorphism and structural preference are summarized below:[94,95,96,97,98,99,100,101]

1. β-Li_2FeSiO_4 can be synthesized at 700°C and its framework contains chains of LiO_4 tetrahedra which connect to parallel chains of the alternate FeO_4 and SiO_4 tetrahedra *via* edge sharing. Synthesis at 800°C yields γ_s-Li_2FeSiO_4 (space group $P2_1/n$) in which LiO_4 tetrahedra are corner shared. Synthesis at 900°C results in the formation of the Υ_{II} polymorph (space group : *Pmnb*) which differs from the β-polymorph (space group : $Pmn2_1$) in the orientation of the tetrahedra. Hydrothermal synthesis yields an ordered β_{II}-polymorph (space group : $Pmn2_1$). In addition, Bruce *et al.* have recently identified another structure designated as inverse-β_{II} in which Li and Fe atoms display mixed site occupancy.[99] The "Υ" polymorphs are, in general, more stable at higher temperatures.

2. Li_2MnSiO_4 has been studied extensively due to its higher intercalation potential than Li_2FeSiO_4 along with the possibility of extracting two Li from the structure. It also adopts Li_3PO_4 based tetrahedral structures like Li_2FeSiO_4. However, after few cycles, Li_2MnSiO_4 has been reported to become largely amorphous which results in rapid capacity degradation.
3. Li_2CoSiO_4 has also been reported and structurally and electrochemically characterized. Hydrothermal synthesis at 150°C yields the β_{II}-polymorph (space group: $Pmn2_1$). Heat treatment of the β_{II}-polymorph at 700°C results in a phase transformation to the β_I –polymorph (space group : $Pmn2_1$). Another polymorph γ_0 (space group: $P2_1/n$) appears when β_I is heated to 1100°C and quenched. No site mixing is observed in the γ_0 polymorph. Attempts of reversible intercalation of Li in Li_2CoSiO_4 show very poor electrochemical activity in the sample, mostly due to electrolyte instability associated with its high redox couple (Co^{2+}/Co^{3+}) which is over 4.8 V.

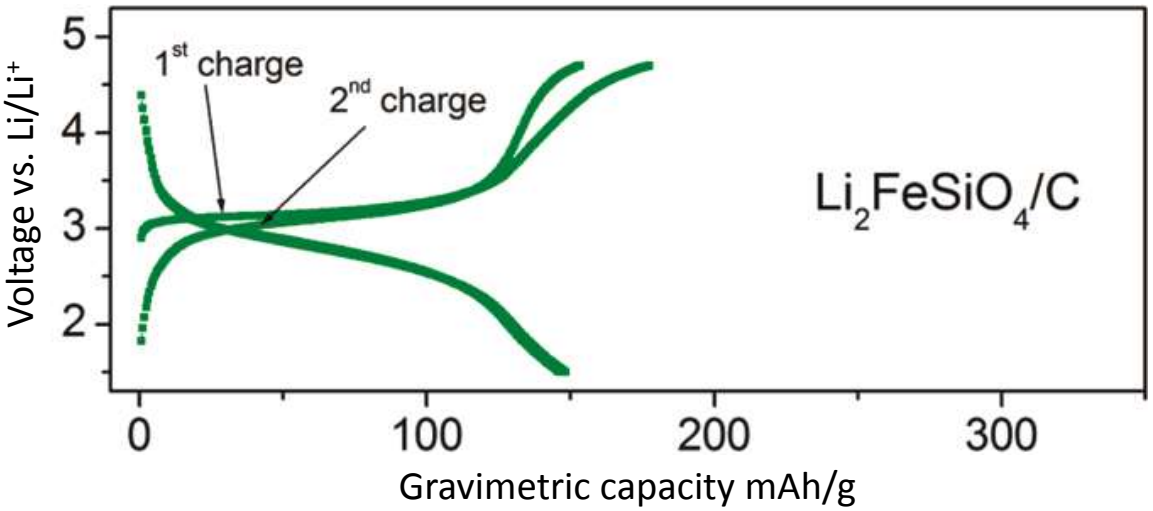

Figure 1.36 Electrochemical charge-discharge curve of carbon coated Li_2FeSiO_4[102]

The electrochemical performance of Li_2FeSiO_4 has been reported extensively and stable cycling has been achieved for reversible intercalation of one Li in the structure. However, the voltage is quite low which results in inferior specific energy density compared to olivine type $LiFePO_4$. The reversible intercalation of two Li in the structure has been demonstrated in one report but the capacity fades quickly after few cycles.[103] The capacity fade is even more severe in the case of Li_2MnSiO_4. The presence of Fe^{4+} or Mn^{4+} in the charged material was not confirmed in this report.[103] The capacity fade in tetrahedra based structures can be understood by invoking the preference of transition metal of "d^4" electronic configuration for octahedron coordination. Topotactic removal of one or two lithium respectively from Li_2MnSiO_4 or Li_2FeSiO_4 results in tetrahedrally coordinated Mn^{3+} or Fe^{4+}. Both of these ions contain 4 electrons in the "d" band and therefore tetrahedral coordination is very unstable configuration which leads to amorphization and consequently capacity degradation after few cycles.

In order to overcome the inherent structural limitations imposed by the olivine type $LiFePO_4$ on Li-ion conductivity, modification of the structure using the F^- polyanion has been proposed.[104,105] $LiFe^{3+}PO_4F$ adopts a triclinic structure similar to mineral "tavorite" found in nature as $LiFePO_4$ (F, OH).[106] In this case, the modifier F^- opens up the structure which allows multidimensional pathways for Li-ion diffusion. Instead of edge sharing, polyhedra are now corner shared. Such connectivity among polyhedra provides two intersecting tunnels in the structure in which Li ions are located. $LiVPO_4F$ adopts a similar structure. Both of these materials display very good capacity retention upon cycling. $LiVPO_4F$ can be further charged at an average voltage of 4.05 V with 90% reversibility at C/10 rate.[107] $LiFePO_4F$ cannot be charged further due to difficulty of obtaining Fe^{4+} within electrolyte stability range. However, discharge

to Li_2FePO_4F occurs at an average of 3 V with very good capacity retention.[108,109] The fact that these excellent electrochemical results could be obtained without any size reduction efforts confirms that tavorites are very good ionic conductors. Low voltage of intercalation for $LiFePO_4F$, however, renders it less desirable than $LiFePO_4$.

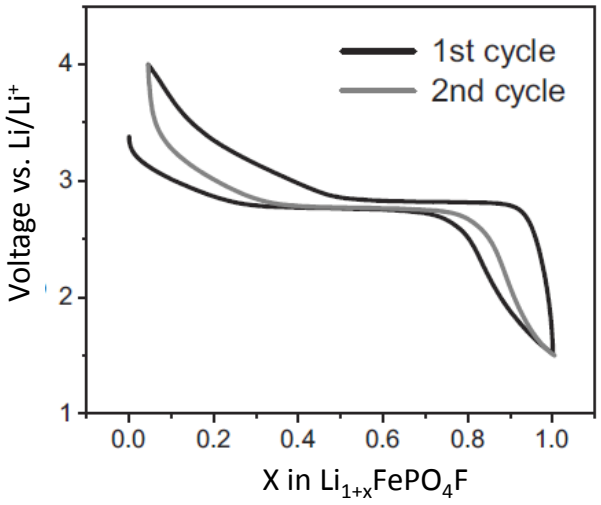

Figure 1.17 Electrochemical charge-discharge curve of $Li_{1+x}FePO_4F$.[108]

1.2.2 Negative Electrodes

In a Li-metal battery, Li metal itself is used as the negative electrode. Li^+ ion is deposited on the Li metal sheet and stripped from it during charge and discharge respectively. However, after few cycles lithium does not deposit uniformly leading to dendritic growth of the metal and short circuit of the cell.[110,111] Due to serious safety issues, use of Li-metal as a negative electrode has been discontinued for any scalable assembly of batteries.

Carbon based materials are the most popular negative electrodes used currently in commercial Li-ion batteries.[112,113,114] Naturally occurring graphite intercalates Li at 0.1-0.2 V *vs.* Li/Li^+ between the carbon layers. It displays much higher theoretical and practical gravimetric

capacity than the common positive electrode materials due to the lighter weight of the carbon.[115,116] The fully intercalated composition can be written as LiC_6 where the intercalation occurs through various intermediate compositions.[117] Comparatively lower volume expansion of the graphite during the intercalation process is a major advantage of this material. Other forms of carbon have been suggested to improve the gravimetric capacity further. Disordered carbon, for example, may increase the capacity by interfacial reaction with lithium instead of intercalation only between the layers.[115] Porous carbon can also increase the interfacial capacity during charge-discharge.

Li-metal alloys have been extensively investigated as negative electrode materials for Li-ion batteries.[118,119,120] Many of the group 4 and 5 metals and semimetals can be alloyed with lithium during the electrochemical process or by using solid state synthesis methods. These materials provide very high specific energy density and react with Li at low potential *vs.* Li/Li^+. However, their most common problem is the large volume expansion observed during the Li de/-intercalation. Several approaches such as nano-sizing, using a second matrix and alloying with a third electrochemically inactive component have been employed to overcome the huge volume change.[121] However, these result only in partial success.

Silicon is one of the most abundant elements on the earth. It reacts with Li at 0.6 V *vs.* Li/Li^+ and therefore can be used as a negative electrode material.[122] Lithium can be alloyed with silicon up to 4.4 atoms of lithium per silicon atom leading to a final stoichiometry of $Li_{22}Si_5$.[123] Such a high Li to Si ratio results in about 10 times higher gravimetric capacity than graphite.[124] However, the unit cell volume of the Si expands by about 400% during the electrochemical reaction and therefore rapid capacity degradation is observed during cycling of the cell.[125] The issue of large volume expansion has been addressed by essentially two basic approaches: the first

is to modify the morphology of the silicon (e.g. silicon nanowires),[126] and the second is to use a carbon matrix to confine the Si and provide greater electronic conductivity.[127,128] More than 80% capacity retention after 100 cycles has been achieved using Si/C composites.[129] Crystalline Si undergoes solid state amorphization upon initial reaction with lithium which exhibits homogeneous volume expansion. However, upon further lithiation, a crystalline phase of composition $Li_{15}Si_4$ precipitates.[130,131,132] Silicon nanowires, however, show absence of any crystalline phase in the lithiated silicon even after deep charging[133] which enables the material to display greater capacity retention with high gravimetric capacities.[134,135]

Among other materials, $Li_4Ti_5O_{12}$ has been studied in great detail for reversible intercalation of Li.[136] The compound crystallizes in the spinel structure and the octahedral sites are shared by 1/3 Li and 5/3 Ti, while rest of the Li is located on the tetrahedral sites. Reversible intercalation of Li^+ in the material occurs at 1.55 volt.[137] This material provides very stable cycling capacity at very high rates, however, its high intercalation voltage results in lower specific energy density compared to intermetallics and Si.

1.3 Na- ion batteries

Na is a much more inexpensive alkali metal than Li, in addition, it is only slightly more electropositive than Li (difference ~0.3 V). Hence replacing Li with Na is an attractive option for the batteries where a slight loss in specific energy density is acceptable with a decrease in the price. Na-ion batteries operate on the similar principle as Li-ion batteries and many similar negative and positive electrode combination pairs can, at least theoretically, provide moderate to high specific energy density.[138,139] In the last 20 years various structures and compositions have been proposed and examined as negative or positive electrode materials for Na-ion batteries. Some of them are summarized below.

Due to similar operating principles and criteria, most of the Na-ion positive and negative electrode materials/structures are similar to those extensively researched for the Li-ion cells. $NaMnO_2$ can be crystallized in either the α (monoclinic) or β (orthorhombic) polymorphs.[140] The first report of the electrochemical behavior of both of these polymorphs was published as early as 1985,[141] showing reversible intercalation of 22% and 15% Na in α or β polymorph respectively. Recently, much improved reversible capacities (~200mAh/g, ~80%) have been reported for the monoclinic α-phase.[142] Unlike $LiMO_2$, charging of $NaMO_2$ takes place in several voltage steps. This is due to the formation of various stable intermediates of Na_xMO_2 composition during the process. As a result of the Na-vacancy ordering and the simultaneous gliding of oxygen layers during cycling of the material, and a large hysteresis is observed between the charge and discharge. Due the relatively large ion size, however, Na^+ does not migrate to the tetrahedral coordination during the cycling and therefore unlike $Li_{0.5}MnO_2$, $Na_{0.5}MnO_2$ does not convert to the spinel phase. Na_xCoO_2 may adopt any of the O3, P2 or P3 type structures depending on the value of x.[143,144] Here, O and P respectively represent the structure with octahedral or prismatic coordination polyhedra around the Na and the numbers 2 and 3 represent count of CoO_6 sheets in one unit cell of the structure.[143] $Na_{0.66}CoO_2$ is the easiest to synthesize and it crystallizes in the P2 type phase. Sodium intercalation in this material also results in many intermediate compositions and many steps are seen in the charge-discharge curve. Among mixed layered oxides, $Na_{0.66}Co_{0.66}Mn_{0.33}O_2$ has been examined most thoroughly and shows solid solution behavior except for one intermediate at $Na_{0.5}Co_{0.66}Mn_{0.33}O_2$.[145] $Na_{0.44}MnO_2$ adopts an orthorhombic crystal structure with MnO_6 octahedra and MnO_5 square pyramid coordination polyhedra as building units.[146,147] Na insertion is fully reversible between 0.25 to 0.65 Na content in the overall composition. Reversible Na-insertion in single crystal

nanowires of the material has been demonstrated up to 1000 cycles with very good capacity retention.[148] P2- type $Na_x[Fe_{0.5}Mn_{0.5}]O_2$ has been recently explored in detail and it displays very promising electrochemical behavior.[149,150]

Among polyanionic materials, NASICONs (Natrium Super Ionic Conductors) have been extensively studied as Na-ion cell positive electrodes.[151,152] Most important of these is $Na_3V_2(PO_4)_3$. Na can be extracted from this material at 3.4 V (V^{3+}/V^{4+}) or inserted at 1.6 V. Therefore it can be used as either negative or positive electrode. Sodium vanadium fluorophosphates are another class of attractive positive electrode materials for Na-ion batteries. Two compositions; specifically $NaVPO_4F$[153] and $Na_3V_2(PO_4)_2F_3$,[154] have been examined for electrochemical insertion/extraction of Na. Na extraction from $NaVPO_4F$ occurs in two steps with the first being at 3 V and the second at 3.7 V *vs.* Na/Na^+. $Na_3V_2(PO_4)_2F_3$ also charges in two voltage steps at 3.6 and 4 V *vs.* Na/Na^+.

Na_2FePO_4F was first proposed by Ellis *et al.* in 2007 and it is isostructural with Na_2MgPO_4F.[155] The layered structure contains Na ions located between the sheets of interconnected FeO_4F_2 and PO_4 tetrahedra. It is very suitable for reversible Na intercalation and experiences only about a 3.5% volume change as Na is removed or inserted. Electrochemically obtained charge-discharge curve displays distinct voltage plateaus between 2.9 and 3.05 V during discharge and charge. Formation of two distinct plateaus in the electrochemical charge-discharge curve (**Figure 1.19**) indicates the formation of an intermediate composition which was identified as $Na_{1.5}FePO_4F$.

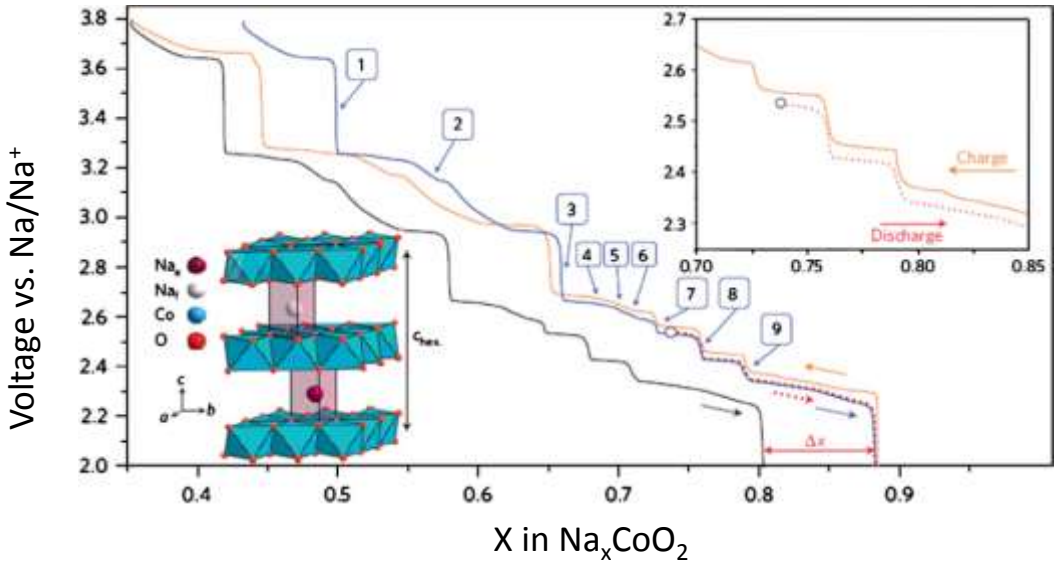

Figure 1.18 Electrochemical charge-discharge curve of Na_xCoO_2.[156] Inset shows an expanded view of the curve. A 2D projection of the structure of $NaCoO_2$ is also shown. The numbers indicate different phases formed during Na-intercalation

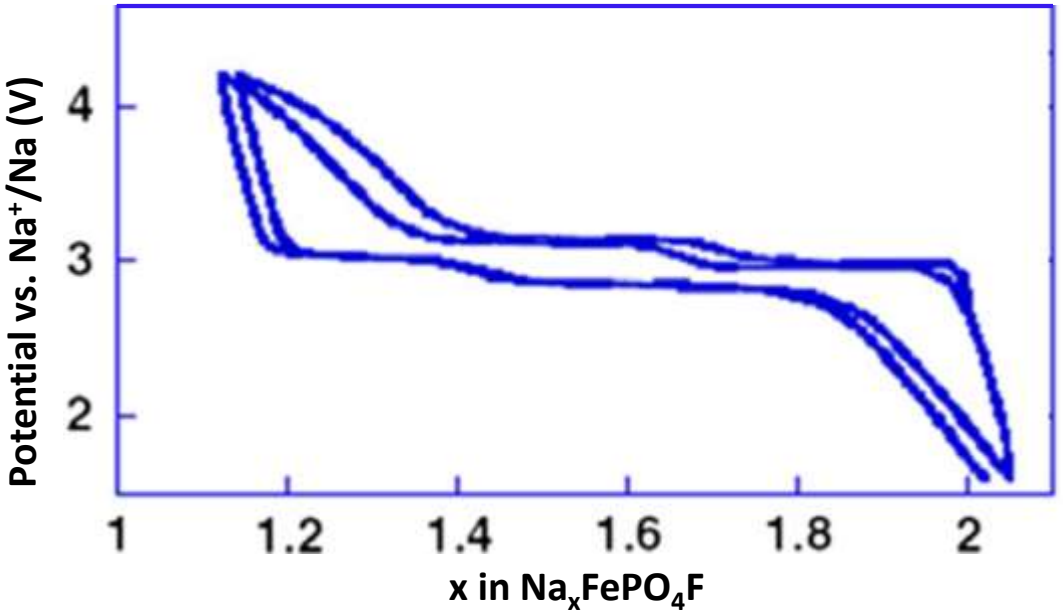

Figure 1.19 Electrochemical charge-discharge curve of Na_xFePO_4F[157]

$NaFePO_4$, when synthesized using conventional methods, does not crystallize in the olivine type structure unlike its Li-analogue $LiFePO_4$. Instead, high temperature synthesis routes yield the maricite type framework. The maricite type framework does not possess open pathways for ion migration similar to olivine and therefore it exhibits no electrochemical activity upon charge or discharge. Recently, however, it has been reported that olivine $NaFePO_4$ can be obtained by inserting Na electrochemically in the olivine type $FePO_4$.[158] Olivine $FePO_4$ in this case is obtained by delithiating isostructural $LiFePO_4$. Interestingly, while only a single plateau at 2.8 V is observed upon discharge, upon charge, an intermediate step corresponding to the composition of $Na_{0.7}FePO_4$ appears. Subsequent cycling shows severe capacity fade. $NaMnPO_4$ and $NaFe_{0.5}Mn_{0.5}PO_4$ can be crystallized in the olivine type structure *via* an ion exchange method from $NH_4MnPO_4 \cdot H_2O$ and $NH_4Fe_{0.5}Mn_{0.5}PO_4 \cdot H_2O$. Interestingly, this material displays a sloping electrochemical profile suggesting solid solution behavior.

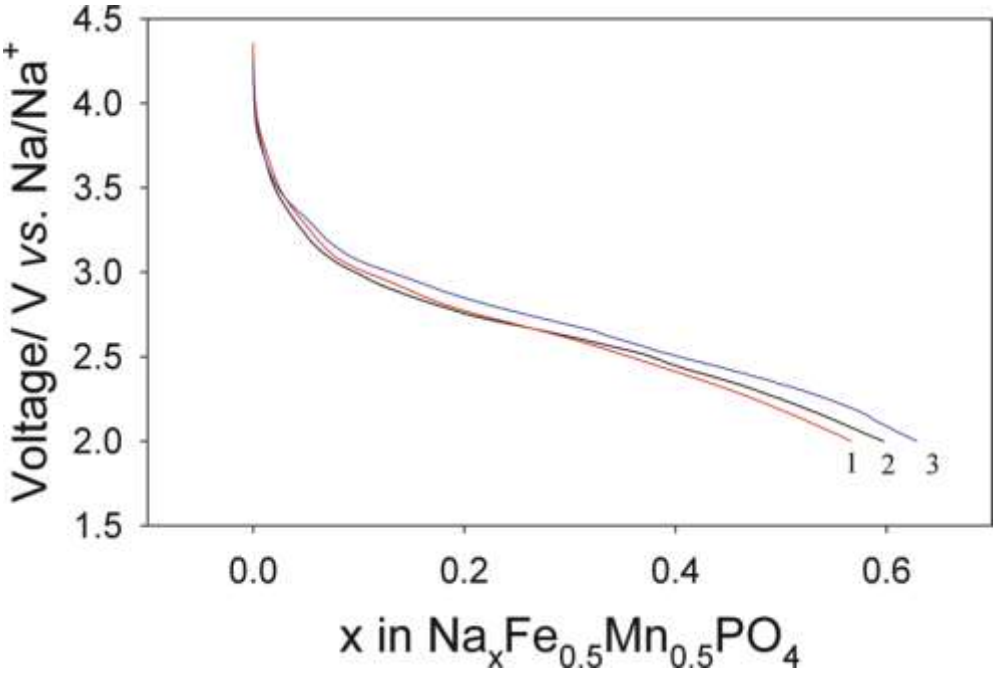

Figure 1.20 Electrochemical charge-discharge curve of olivine $Na_xFe_{0.5}Mn_{0.5}PO_4$[158]

Substantial research work has been devoted to developing suitable negative electrodes for Na ion batteries. Sodium metal itself, just like Li, cannot be used for long term cycling because of dendritic growth of the Na on charge which leads to short circuiting. The most common negative electrode for Li ion batteries, graphite, does not intercalate Na between its layers due to the larger size of the ion. Among other carbon based electrodes petroleum coke show good potential for Na-intercalation.[159] Electrochemical potential for Na insertion in hard carbon is same as that of the metal itself which indicates that the insertion occurs through surface pores. Following investigation, Na was found to intercalate among disordered layers of the carbon and it can display high gravimetric capacities at low rates.[160] It has been shown recently that high rates in non-graphitic carbons can be achieved by tuning the microstructure and the porosity.[161] Among the non-carbon and the non-silicon based negative electrodes for Na-ion batteries, Na_xTiO_2 [162] has been shown to intercalate Na around 1 V. $Na_2Ti_3O_7$[163] intercalates Na at 0.3 V and $Na_2Ti(PO_4)_3$ at 2.1 V.[164]

1.4 Scope of the Thesis

This thesis deals with the synthesis and characterization of fluorosulfate based high voltage positive electrode material for the Li and Na-ion cells using solvothermal techniques. A number of compounds belonging to this family were synthesized and electrochemically characterized in a Li-batteries. The structure of each of them was solved using X-ray and neutron diffraction methods. Sodium based compounds of similar compositions were also synthesized. Various characterization techniques have been employed to understand the structure, ionic conduction and electrochemical performance. The possibility of synthesizing alternate structures to improve the electrochemical performance was also explored by changing the nature of the alkali or transition metal cation. **Chapter 2** describes the synthesis and characterization

methods/techniques used in this thesis. **Chapter 3** details the synthesis, structural analysis and electrochemistry for fluorosulfate of general composition $LiMSO_4F$ (M=Fe, Mn, $Fe_{1-x}Mn_x$). **Chapter 4** describes the application of computer simulation methods to determine the Li and Na ion migration pathways in various phosphate and sulfate based framework. **Chapter 5** deals with the synthesis and structural characterization of sodium and ammonium based fluorosulfate materials. **Chapter 6** presents the overall summary and the roadmap for future work.

Chapter 2

Methods and Techniques

2.1 Introduction

To understand and improve a material's property, it is important that it is characterized using modern tools available to the scientific community. An in-depth characterization of the fluorosulfate materials is complicated by the fact that these are air sensitive and must be synthesized and processed only under a dry and oxygen free atmosphere. Various techniques and methods have been used to prepare and characterize these materials to determine their structure, morphology and electrochemical properties. These provide an in-depth understanding of mechanisms that operate during preparation and subsequent application of these materials as positive electrodes for Li-ion batteries.

Diffraction methods reveal detailed information about crystalline materials at the atomic scale and have been extensively used in the current work. Electron microscopy provides morphological and compositional information and therefore it was used to examine the material's purity and particle size correlation with electrochemical performance. Electrochemical methods were used to study the material's behavior as a positive electrode in Li batteries. Characterizations based on Fourier transform infrared infra-red (FTIR) spectra were used to study the nature of chemical bonds in the structures and thermogravimetric analysis (TGA) established the thermal stability of the materials. Atomistic scale simulations were carried out to investigate migration pathways of Li and Na ions in various structural frameworks. This chapter

outlines the basic scientific and technical details about the synthesis and characterization methods used in the current work.

2.2 Synthesis Techniques

2.2.1 Conventional Solvothermal Synthesis

Solvothermal synthesis methods have been extensively used to prepare various novel phases and morphologies.[165,166,167] In contrast with traditional solid state methods, solvothermal synthesis is carried out in an organic solvent in a closed system at moderately high temperature- usually above the boiling point of the solvent. Under such conditions, critical properties of solvents such as dielectric constant and viscosity are considerably modified. This results in a lower activation energy barrier for the reaction. The reaction container used in the current work is described in **Figure 2.1**.

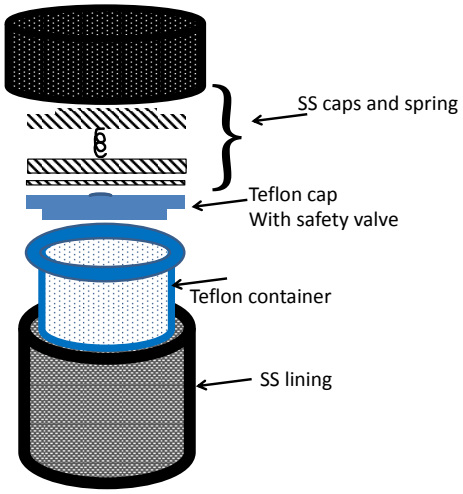

Figure 2.1 Conventional solvothermal reaction container

Reactants are first transferred in a Teflon™ container along with the solvent and then placed in a stainless steel (SS) autoclave. The use of the autoclave provides physical strength

against the inside pressure and the Teflon™ lining provides protection against corrosion due to the solvent. Magnetic stir bars can be added in the reaction mixture if stirring is needed. The container is sealed using various caps as shown. Finally the mixture is transferred to a preheated oven for a required time and temperature.

2.2.2 Microwave Solvothermal Synthesis

Microwave solvothermal synthesis differs from conventional solvothermal methods in that the heating of the reaction mixture is now carried out in a microwave oven where it occurs through microwave-matter interaction. The frequency normally used in commercial microwaves is 2.45 GHz which is optimum for generating maximum heat with common solvents. Under microwave heating, polar solvents try to align their dipolar moment along the electric field generated by the microwave. As this electric field quickly fluctuates, dipolar moments try to realign themselves accordingly and heat is generated in this process due to the friction and dielectric losses.[168] The energy loss during this interaction is quantified by the term known as the tangent loss which is defined as the following:

$$\tan \delta = \varepsilon'' / \varepsilon'$$

where ε'' is the dielectric loss and ε' is the polarizability of the molecules under the electric field. Due to this specific interaction under microwave irradiation, temperature gradients in solvent are almost absent during the reaction, and temperatures can rise very quickly throughout the reaction medium. However, the reasons behind the remarkable ability of the microwave methods to rapidly synthesize compound within minutes that otherwise takes hours and days are still under debate.[169]

Organic solvents are generally classified in three categories for microwave synthesis. Solvents with tan δ>0.5 are high microwave absorbers and therefore can generate a great deal of heat very quickly under microwave irradiation. Solvents with 0.1< tan δ < 0.5 and tan δ <0.1 are known as medium and low grade solvents for microwave synthesis respectively. Glycols, in general, have been noted as ideal candidates for microwave solvothermal synthesis as these materials interact very strongly with the microwaves.

During recent years microwaves have been effectively used for the synthesis of many battery related materials such as $LiFePO_4$[170,171] and Li_2FeSiO_4.[102] These methods are rapid and provide interesting morphology along with good size control. However, due to low temperatures and very rapid synthesis routes, frequently, the product displays poor crystallinity and high concentration of defects which may require post synthesis heat treatment.

2.3 Characterization Techniques

2.3.1 Diffraction Techniques

Diffraction is one of the consequences associated with a wave's interaction with an obstacle in the path of its propagation. Each point on the obstacle acts as a new point source and intensity of the resulting wave is produced as a result of interference. Similarly, when neutrons of a certain energy interact with an obstacle, due to their wave like behavior at high velocity, they can also produce diffraction patterns. Effects of the diffraction are intensified if the obstacle is of the similar size range as the wavelength of the incident wave. If the obstacle is periodic in nature, diffraction patterns can be analyzed to study the nature of the periodicity and local distribution. This is one of the very popular techniques adapted to study crystal structures where incident waves are X-rays or neutrons.

Figure 2.2 Anton Parr microwave system

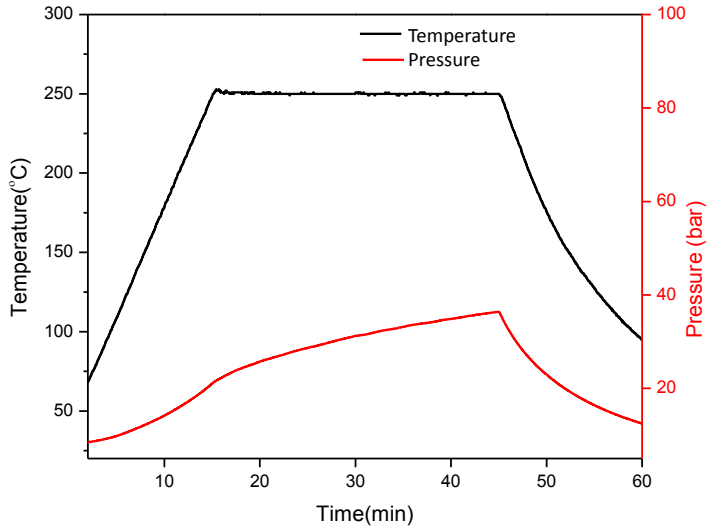

Figure 2.3 A representative plot for temperature and pressure increase during a microwave reaction. The data was obtained during the reaction using internal probes.

2.3.2 Powder X-ray Diffraction

X-rays have an electric field which oscillates perpendicular to their movement. They are located in the electromagnetic spectrum between the γ-rays and the ultraviolet. Depending on the energy, they can be classified either as hard X-rays (high energy) or soft X-rays (low energy). When an electron comes under the influence of an X-ray beam it starts to accelerate or de-

accelerate with the frequency of the incident beam. This phenomenon is called "Thompson scattering". If an X-ray beam encounters a distribution of the electrons which is periodic in nature, these multiple scattered beams interfere with each other to produce a diffraction pattern.

Prof. Max von Laue, first (1912)[172] identified the basic mechanism by which crystals can be used as a grating for the diffraction of the X-ray beam. He showed that when a stream of X-rays is passed through the crystal of a zinc blende structure, a pattern of bright spots appear on the screen according to the laws of diffraction. Subsequently Lawrence Bragg simplified and explained the underlying principle in a more simple and effective manner by assuming each plane of atoms in the crystal behaved as a reflecting surface. The schematic shown in **Figure 2.4** outlines the diffraction of X-rays from an array of atoms. A monochromatic parallel set of beam striking at an angle Θ from a plane of atoms is reflected back and the reflecting beam makes a 2Θ angle from the incident beam. It can be shown using geometry that two scattered beams of wavelength λ from a set of parallel planes at distance d from each other will have zero phase difference if following condition is satisfied (n is an integer number):

$$n\lambda = 2d * \sin\theta$$

The implication of the above equation simply means that at any given orientation of a crystal a set of parallel monochromatic X-rays will constructively interfere for only one set of parallel planes. In other words a set of bright points will appear on the screen when a spectra of X-rays (a set of λ) are passed through the crystal at a given orientation. Each bright point in this case can be analyzed for a set of parallel planes.

It is difficult to prepare single crystals of many complex and metastable materials. Therefore an alternative technique, known as the Debye-Scherrer method, was developed to

collect X-ray diffraction patterns from powder samples. Modern techniques use diffractometer in which the sample and the diffracted beams are rotated with respected to the incident beam to collect the pattern for a range of angles. An angle *vs.* intensity plot is analyzed to extract the crystal structure. In this thesis, powder X-ray diffraction was performed on a Bruker D8-Advance powder diffractometer equipped with a Vantec-1 detector, using Cu-Kα radiation (λ_{avg}= 1.5418 Å) in the range from 10° to 120° 2θ at a step size of 0.025° using Bragg-Brentano geometry.

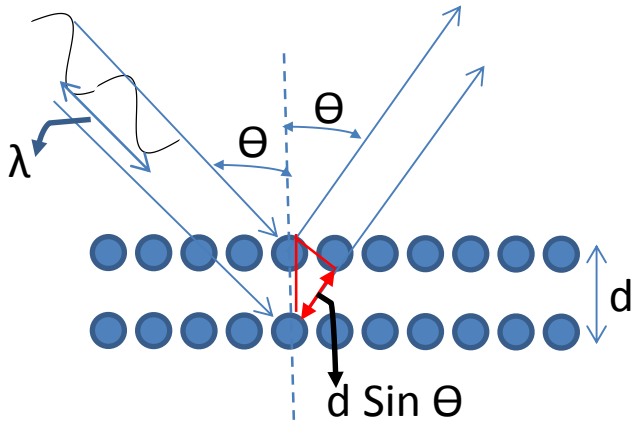

Figure 2.4 Bragg scattering of X-rays from parallel plane of atoms

2.3.3 Time of Flight Neutron Scattering

Due to wave particle duality, neutrons of moderate energy also produce a diffraction pattern when they are passed through a crystal. Unlike X-rays, neutrons directly interact with the nucleus of the atom. The interaction of the neutron with a nucleus can result in either incoherent or coherent scattering. The coherent scattering from a crystal appears as Laue diffraction spots and is used in the identification of the structure. Strength of the scattering is measured in terms of a scattering length which is specific to each atom in the periodic table. Therefore, the neutron diffraction pattern complements the X-ray diffraction in the sense that former is generated by

waves scattered by the nucleus and later is generated by waves scattered from the electrons surrounding the nucleus. Lighter atoms such as Li cannot be located based on X-ray diffraction pattern and neutron diffraction is essential. Additionally, X-rays cannot distinguish between two atoms with close atomic numbers while neutron diffraction can generally provide this information depending on the scattering lengths.

Neutron experiments reported in the current work were carried out at the Oak Ridge National Lab, Tennessee (ORNL), USA. This facility uses a spallation method to produce neutrons, in which a stream of protons is first bombarded at a heavy nucleus resulting in high energy neutrons. These neutrons are then passed through a moderator to decrease their energy. The moderate energy beam (thermalized neutrons) is used to probe the crystal structure of the microcrystalline sample. Samples were placed in a vanadium can and POWGEN diffractometer at ORNL was used to collect the diffraction data. This diffractometer is capable of probing the 0.3Å to 3Å d-range with a resolution of < 1%.

Bragg's law can be modified for a spectrum of diffracted neutron beams collected on a single orientation Θ for a period of time t:

$$t = (2m/h)* L*\sin\theta * d$$

Where m and h are the mass of the neutron and Planck's constant respectively, L is the length travelled by neutron after bombarding the sample, Θ is the angle of data collection and d is the interplanar distance in the crystal. Clearly, for a range of λ values, the diffracted beam hits the target at different times and this can be used to extract the d or Θ vs. intensity plot. This method is known as "time of flight" data collection for neutron diffraction.

2.3.4 Structure Refinement

Relevant structural parameters such as lattice parameters and atomic positions are obtained from the experimentally collected diffractogram by using an iterative fitting process starting from a given model of the structure. This process is known as structural refinement. To identify the initial model of the crystal structure from the collected diffraction pattern, the pattern is matched to the inorganic crystallographic structure database. This strategy was adopted for compounds reported in Chapter 3 and 5. Once a good model has been found, exact values of atomic position and lattice parameters can be extracted by iterative refinement. The technique was developed by Hugo Rietveld in the 20^{th} century and it is now extensively used to derive accurate structural parameters for a wide range of materials, and to determine structures of microcrystalline materials.

Three kinds of information can be extracted from a diffractogram: 1. The position (2 Θ or d) of the peaks provides clues as to the symmetry of the structure; 2. The intensity of the peaks provides the information about the atom type (scatterer), and their location in the unit cell; 3. The peak shape provides information about the nature of the crystal (coherence length). The goal of the Rietveld refinement is to minimize the difference between the observed and the calculated diffraction pattern using least squares methods. This is achieved by refining the factors influencing the peak position, height and shape. Peak positions are refined starting from given model of the unit cell and the sample position parameters; the later accounts for the relative position of the sample with respect to the incident beam. This is followed by refinement of a set of other parameters such as profile functions and the atomic positions which adjust themselves to yield the right peak shape and intensity.

In the Rietveld refinement method, the intensity of a diffraction peak obtained by powder x-ray diffraction (PXRD) is formulated as follows:

$$I_{Calc} = S_F \Sigma_k L_k \left| F_k \right|^2 S\ (2\theta_i - 2\theta_k) P_{k,} A\ + bkg_i$$

Here, bkg_i is the background intensity, S_F the beam intensity scale factor, S ($2\theta_i$- $2\theta_k$) the profile shape function, L_k the polarization factor, A the absorption factor and P_k the preferred orientation factor. F_k is known as structure factor and depends on the type and location of atoms in the structure. For a plane with *hkl* Miller indices the structure factor is defined as follows:

$$F(hkl) = \sum_{n=1}^{N} f_n e^{2\pi i(hx_n + ky_n + lz_n)}$$

Here, f is atomic scattering factor and is considered analogous to the scattering length discussed above in the context of neutron scattering. Similar formulations exist for neutron diffraction as well. In addition two parameters specific to time of flight neutron diffraction exist in GSAS: DIFC, and DIFA. These two respectively represent theoretical time of flight and wavelength absorption correction and are refined accordingly. In the current work Rietveld refinement has been performed using either GSAS on the EXPGUI[173,174] platform or the Bruker-AXS TOPAS 4.2 (Bruker-AXS, 2008)® software program.

2.4 Electron Microscopy

Electron microscopy is used to visually inspect the sample, its topology and primary particle size. In an electron microscope, electrons are thermally produced from the source and focused on to the sample with the help of condenser and objective lenses. Electron's interaction with the matter results in emission of secondary electrons, backscattered electrons and X-rays,

and the image of the sample can be produced by analyzing these. Images in this thesis were taken on a LEO 1530 field emission electron microscope in back scattered imaging mode. Energy Dispersive X-ray (EDX) analysis was carried out on a system attached to the scanning electron microscope (SEM) to determine the elemental composition of the sample.

2.5 Thermal Analysis

Thermal analysis was carried out to determine the stability of the fluorosulfate and hydroxyl sulfate compounds. The technique involves heating of the sample with continuous monitoring of the weight loss. The measurements were performed under a controlled atmosphere on a SDT Q600 analyzer.

2.6 Infrared Spectroscopy

Infrared spectroscopy (IR) determines the energy levels that can absorb incident infrared wavelength. In this technique a spectrum of infrared rays are passed through the material and the resulting absorption spectrum is analyzed. A standard table exists for most of the known chemical bonds and the corresponding absorption peak. In the current work, a Bruker Tensor infrared spectrometer was used to collect spectra of as-prepared materials ground with KBr and pressed into pellets. Pellets were dried overnight at 100°C in a vacuum oven before characterization.

2.7 Electrochemical Characterization

To study the electrochemical properties of the materials, they were cycled under a galvanostatic mode. In this mode, a constant current is applied to a cell and voltage is recorded as a function of the number of lithium ions and electrons de/-inserted into the active material in

the electrode. The current direction is changed at the cut-off potentials to reverse the flow of the charge and test the reversibility. Electrode characteristics, such as capacity, rate capability and cycle life can be extracted from the results. Electrochemical evaluations of the Li (ion) batteries were mainly carried out in Swagelok^{TM} cells using a commercial (VMP3) multichannel galavanostat/potentiostat. To prepare a working electrode, the active material was typically first ball milled with Super P carbon. A slurry was formed by adding N-methylpyrrolidinone (NMP) solvent to this mixture. The slurry was spread onto a carbon coated current collector and dried overnight. Typical loading of the active mass was between 3 and 5 mg/cm^2. The cells were assembled in an argon-filled glove box with oxygen and moisture levels lower than 5 ppm. The electrolytes were composed of a 1 to 1.2 M $LiPF_6$ solution in a polar organic solvent (EC:DMC:: 1:1), and lithium metal foil was used as the counter electrode.

2.8 Simulation Methods

Simulation of materials is considered now a well-established field in solid state chemistry. Due to significantly increased computational capabilities in last few decades, it has become possible to simulate some of the very complex calculations. Various techniques have been developed based on the current understanding of the atomic and molecular interactions to predict properties of the materials which are otherwise very difficult to measure. There are three broad methods[175] that are currently used to calculate the properties of solid state materials. First, q*uantum-mechanical (QM or ab initio)* calculations are used to calculate the electronic structure. Introduction of local charge correlations in the calculation during last decade has made this method increasingly accurate for the prediction of various properties. Second are *molecular dynamic (MD)* methods, which are based on explicit dynamical solution of the ensemble of particles for which Newton's laws of motion are solved. The third category is

known as the *atomistic simulation* method and it is based on the formulation of the total energy of the system. This energy is minimized to determine accurate potential parameters for further calculations for a given structure. Atomistic simulations methods as embodied in the General Utility Lattice Program (GULP)[176] code have been used extensively in **Chapter 4** of the current thesis.

The atomistic scale simulation method calculates the total energy of the system,[177] by dividing the solid into two kinds of interatomic forces: short range and long range. Long range force consists of the electrostatic interaction among atoms and it is expressed as the general Coulombic interaction equation between two point charges. Short range forces are mainly represented by attractive dispersive forces and repulsive van der Waals interaction. The energy of the total system is written in terms of nuclear coordinates. Minimization of the energy is not straight forward due to diverging nature of the Coulombic forces since the number of interaction increase as $4\pi r^2 N_\rho$ where N_ρ is the atomic pair density. To solve this problem, Ewald summation technique is used which divides the whole charge interaction in to real and reciprocal space:[178,179]

$$U^{real} = \frac{1}{2}\sum_{i=1}^{N}\sum_{j=1}^{N}\frac{q_i q_j}{r_{ij}} erfc\left(\eta^{\frac{1}{2}} r_{ij}\right)$$

$$U^{recip} = \frac{1}{2}\sum_{i=1}^{N}\sum_{j=1}^{N}\sum_{G}\frac{4\pi}{V} q_i q_j \exp\left(iG.r_{ij}\right)\frac{\exp\left(-\frac{G^2}{4\eta}\right)}{G^2}$$

$$U^{self} = -\sum_{i=1}^{N} q_i^2 \left(\frac{\eta}{\pi}\right)^{\frac{1}{2}}$$

$$U^{electrostatic} = U^{real} + U^{recip} + U^{self}$$

Here, U is the energy term, G the reciprocal lattice vector, q the charge on the ion and V is the volume of the unit cell. Parameter η controls the division of work in real and reciprocal

space and it is defined as follows (*w* represents the relative computational expense term in real *vs*. reciprocal space):[178]

$$\eta_{opt} = \left(\frac{Nw\pi^3}{V^2}\right)^{\frac{1}{3}}$$

Short range interactions are modeled using a Buckingham potential which is defined as follows:

$$V_{ij}(r_{ij}) = A\exp^{-\frac{r_{ij}}{\rho}} - \frac{C}{r_{ij}^6}$$

A, ρ and C are ion-ion potential parameters and r is the inter-atomic distance. In this case as well, both, the van de Waals and dispersion interaction can be quickly converged by splitting them in reciprocal and real space. A list of other functions and their detailed discussion can be found here.[180] For the higher covalent degree of interaction in the sulfate group, Morse potentials were used to describe intra-molecular bond-stretching interactions between the S and O ions:

$$\phi_{ij}(r_{ij}) = D\{1-\exp[-\beta(r_{ij}-r_0)]\}^2$$

Here r_0 is the equilibrium atomic separation between ions *i* and *j*, and *D* is the dissociation energy of the molecule or polyatomic ion, and β is a parameter that controls the width of the potential well.

Three-body (covalent) bond-bending forces within the SO_4^{2-} (or PO_4^{3-}) tetrahedra were modeled using a harmonic potential,

$$\phi_{ijk}(\theta_{ijk}) = \frac{1}{2}k(\theta_{ijk}-\theta_0)^2,$$

where k is a force constant and Θ_0 is the equilibrium angle subtended by ions j and k about ion i. Interactions between ions in the same sulfate group were assumed to be entirely non-Coulombic. To account for the polarization of the atoms, a core-shell model developed by Dick and Overhauser is employed in which charge is distributed on the core and massless shell of the atom attached to it by a harmonic force. This is important to calculate the dielectric properties and impact of defects in the structure. Initial distribution of the charge distribution on the core and shell was taken from the literature data and relaxed to fit the input structure. Most of the cations are assumed to be rigid in the current work and therefore formal charges are assigned to the core of the atoms. Shell and core both are simultaneously refined in the GULP code.

Once the energy of the system has been defined in terms of the nuclear coordinates, an initial structure is provided as the first guess and the interatomic potential parameters are relaxed to simulate the crystal structure by minimizing the calculated energy of the system. In the current work, simulations have been performed under constant pressure conditions. In this case, lattice vectors and coordinates are adjusted to remove forces on both the unit cell and the individual atom. Energy minimization is achieved by using Newton-Raphson procedure. An important feature of the atomistic scale simulations is their ability to calculate the energy of formation of point defects. GULP incorporates this feature by adopting the strategy developed by Mott and Littleton. In this scheme, polarization response of the lattice to a charged defect is studied by dividing the region of interaction in to two parts. The inner region is relaxed explicitly and the outer region is calculated by assuming continuum approximation.

These simulation methods have been extensively used in the past to study various oxides, phosphate, silicates and other ionic and semi ionic solids. They provide valuable information about ionic conduction, defect chemistry and other structural information that is otherwise either

difficult or impossible to probe using physical characterization tools. In the context of the battery materials they have been used to understand the mechanism of defect chemistry and ionic conduction in olivine[79] $LiFePO_4$ and recently Li_3PO_4 type[181] Li_2FeSiO_4 materials.

Chapter 3

Synthesis and Electrochemistry of Li-Transition-Metal Fluorosulfates

3.1 Introduction

Li transition metal fluorosulfates were proposed as promising Li-ion battery positive electrode materials in 2002 along with a synthesis procedure for obtaining phase pure tavorite-type-$LiMgSO_4F$.[182] The synthesis of $LiMgSO_4F$ was carried out using conventional high temperature solid state methods which involved heating $MgSO_4 \cdot H_2O$, Li_2CO_3 and NH_4F together at 550°C. However, isostructural Li-transition metal-fluorosulfates cannot be synthesized using the same method because of the precipitation of more thermodynamically stable sulfates and oxides. Solid state reaction among NH_4F, Li_2CO_3 and $FeSO_4 \cdot H_2O$, for example, produces LiF and $FeSO_4$ below 400°C and various other products above 400°C. This indicates that activation energy needed for the crystallization of $LiFeSO_4F$ cannot be achieved within thermodynamic stability limits of this compound in a conventional solid state reaction. Solution based synthesis methods can reduce the kinetic energy barrier during a reaction by providing better contact among reactants. However, water based solvents dissolve the fluorosulfate product and therefore cannot be used. It was reported in 2010 by Recham *et al.*[183,184] that the thermodynamic metastability of $LiFeSO_4F$ means that crystallization must be effected in hydrophobic liquid medium using $FeSO_4 \cdot H_2O$ and LiF as reactants. The ionic liquids, while offering much promise of tailoring reactivity, are prohibitively expensive at ca. $500/g, and removal of excess LiF reagent is almost impossible owing to its low solubility.

The structure type (szomolnokite) of $FeSO_4 \cdot H_2O$ has a strong structural resemblance to the fluorosulfate $LiFeSO_4F$ tavorite type structure and the H-OH in $FeSO_4 \cdot H_2O$ (i.e. $HFeSO_4OH$) is replaced by Li-F to generate $LiFeSO_4F$ in an ionothermal reaction, as noted.[183] Thus, the reaction between the alkali metal fluorides and $FeSO_4 \cdot H_2O$ involves two simultaneous processes: 1) loss of water from $FeSO_4 \cdot H_2O$ and 2) insertion of LiF into the structure. To obtain a pure product, the reaction rate (step 2) must be greater than the dehydration rate (step 1) so that the crystallization of $FeSO_4$ can be avoided. Increasing the temperature lowers the activation energy barrier for the reaction. However, it will also accelerate the dehydration of the precursor. Therefore a balance must be struck between these two competing processes of dehydration and reaction in order to crystallize $LiFeSO_4F$. This is achieved in ionothermal synthesis[183] due to the tendency of hydrophobic ionic liquid medium to delay the release of water from the precursor and allow an increase in the reaction temperature.

Organic solvents are ideal candidates for the synthesis of novel compounds, particularly, in the case of water sensitive compounds. They have been used in the past to synthesize metastable compounds,[185] complex morphologies[186] and nanosized materials.[187] However, the topotactic reaction under solvothermal conditions in common hydrophobic solvents such as toluene does not result in the fluorosulfate product. This chapter describes the synthesis method of tavorite and triplite type $LiMSO_4F$ (M =Fe, Mn, $Fe_{1-x}Mn_x$) in hydrophilic glycol media followed by their structural and electrochemical characterization.

3.2 Experimental

3.2.1 Synthesis

3.2.1.1 $MSO_4 \cdot H_2O$

Monohydrate precursor $FeSO_4 \cdot H_2O$ was obtained by heating $FeSO_4 \cdot 7H2O$ under Ar atmosphere. In order to synthesize $FeSO_4 \cdot 7H_2O$, Fe-powder (5g) and dilute H_2SO_4 (45 ml, 33%w/w) were mixed together in a beaker. The reaction solution first became transparent and then changed to slightly green color after 1 hour of the reaction. $FeSO_4 \cdot 7H_2O$ was precipitated by adding ethanol in 2:1 volume ratio to the solution. The precipitate was filtered and the resultant green product was characterized as $FeSO_4 \cdot 7H_2O$. $FeSO_4 \cdot 7H_2O$ was heated at 100°C for 3 hours in Ar atmosphere to obtain $FeSO_4 \cdot H_2O$ which was characterized using XRD and TGA (**Figure 3.1** and **Figure 3.2**). $MnSO_4 \cdot H_2O$ was directly purchased from Sigma-Aldrich.

To synthesize mixed transition metal monohydrate $Fe_{1-x}Mn_xSO_4 \cdot H_2O$, required moles of Fe powder were first dissolved in dilute H_2SO_4, and $MnSO_4 \cdot H_2O$ was added to it after the solution turned completely transparent. After one hour of continuous stirring, mixed-metal-sulfate hydrate was precipitated by adding ethanol in 2:1 volume ratio to the solution. Filtered product was heated at 150°C for 2 hours in Ar atmosphere to obtain the monohydrate sulfate compound.

3.2.1.2 Tavorite -Type-$LiMSO_4F$

3.2.1.2.1 Conventional Solvothermal (ST)

Synthesis of $LiMSO_4F$ was performed using well known conventional solvothermal methods. Tetraethylene glycol (TEG) was used as a solvent. TEG has high boiling point (314°C

at atmospheric pressure), moderately low viscosity at room temperature (58.3mPs) and moderate dielectric constant (15.7). Therefore, it serves as an ideal candidate for the synthesis of metastable compounds below 300°C. Temperatures as low as 220 °C are ideal in glycol for the topotactic reaction as $FeSO_4 \cdot H_2O$ dehydrates at temperatures greater than 230 °C. The reaction in more hydrophilic solvents such as triethylene glycol does not result in the fluorosulfate product.

To obtain phase pure product, monohydrate transition metal sulfate ($MSO_4 \cdot H_2O$) and LiF (Sigma-Aldrich) were well mixed in 1:1.1 molar ratio. The mixing was achieved in a planetary ball mill (Fritsch pulverisette 5) under Ar atmosphere with typically 1:30 weight ratio of precursor powder to agate balls (10mm diameter) in an agate container after 10 hours of milling at 300 rpm. The ball-milled mixture was transferred into a 43 ml Teflon^{TM}-lined Parr reactor along with 30 ml of the tetraethylene glycol (TEG) and stirred for 30 min. The reactor was then placed in an oven preheated to 220°C for the synthesis of $LiFeSO_4F$. After 60 hours of heating, the reactor was taken out of the oven and cooled down on a lab bench to room temperature. Product was washed with dry acetone or tetrahydrofuran (THF) three times and vacuum filtered in a bench top glove-box filled with nitrogen followed by overnight drying in a vacuum oven at 100°C before characterization.

3.2.1.2.2 Microwave Solvothermal (MW)

To perform the microwave synthesis, LiF and $FeSO_4 \cdot H_2O$ (1.1:1) were mixed under argon atmosphere for 2 hours in a planetary ball mill under similar conditions as above. The homogeneous reaction mixture, along with 20 ml tetraethylene glycol (TEG), was sealed in a closed 100 ml Teflon™ vessel which was fitted to a rotor with a pressure and temperature probe. The rotor containing the closed Teflon™ vessels was then placed on a turntable for uniform heating in an Anton Paar microwave synthesis system (Synthos 3000). The desired microwave

exposure time and temperature were software controlled. A preset profile (desired time, temperature) was followed automatically by continuously adjusting the applied microwave power (0-1200W, 2.45 GHz); the temperature was raised to 220°C in 5 min and maintained for 10 min. The pressure increased almost linearly with the temperature upto 20 bar but remained constant at this value once the temperature ramp reached its plateau.

3.2.1.3 Triplite Type-$LiMSO_4F$

3.2.1.3.1 Conventional Solvothermal (ST)

$LiFe_{1-x}Mn_xSO_4F$ (x = 0, 0.05, 0.1, 0.2, 0.5 and 1) powders were synthesized *via* solvothermal chemistry following the procedure described above. Monohydrate powder was ball milled (Fritsch pulverisette 5) with LiF in 1:1.1 ratio for 10 hours at 300 rpm. The mixed precursors were transferred into a 43 ml Teflon™-lined reactor, and 30 ml of tetraethylene glycol was added. The mixture was stirred for 30 minutes and the reactor was transferred to an oven (T = 250 °C) for 60 hours for $0.1 \leq x \leq 1$ and for 1 and 2 weeks respectively for x = 0.05 and x = 0. Product was washed with dry acetone or tetrahydrofuran (THF) three times and vacuum filtered in a bench top glove-box filled with nitrogen followed by overnight drying in a vacuum oven at 100°C before characterization.

3.2.1.3.2 Microwave Solvothermal (MW)

Tavorite $LiFeSO_4F$ obtained by microwave synthesis method was heated at 350°C for one hour under Ar atmosphere.

3.3 Results and Discussion

3.3.1 Szomolnokite ($FeSO_4 \cdot H_2O$)

X-ray powder diffraction pattern of Fe monohydrate sulfates ($FeSO_4 \cdot H_2O$) is shown in **Figure 3.1**. TGA curves of $FeSO_4 \cdot H_2O$ are shown in **Figure 3.2**. Dehydration of this compound starts around 230°C and the resulting compound $FeSO_4$ is stable until above 500°C. Monohydrate iron sulfate adopts szomolnokite mineral type structure which is classified in monoclinic space group *C*2/*c*. The structure consists of corner shared metal octahedral chain along the *c*-axis and two hydrogen atoms are attached to the linking oxygen atom of the Fe-O-Fe chain as shown in **Figure 3.3**. Thus, linking oxygen atoms is the most electronegative ligand which leaves the structure as H_2O after a heat treatment.

3.3.2 Tavorite-Type-$LiMSO_4F$

The crystallographic structures of $FeSO_4 \cdot H_2O$ and $LiFeSO_4F$ are very similar as shown in **Figure 3.3**. During the reaction with LiF, H-OH molecule of $FeSO_4 \cdot H_2O$ is replaced respectively by Li-F followed by rotation of the framework around *c*-axis to form $LiFeSO_4F$:

$$LiF + FeSO_4 \bullet H_2O \rightarrow LiFeSO_4F + H_2O \text{ ……..(1)}$$

Milling of the reactants ensures a smaller particle size and intimate mixing. These factors speed up the reaction as opposed to slowing down the dehydration, thus favoring the topotactic conversion at lower temperatures in inexpensive hydrophilic solvents and reducing the energy and materials cost of producing $LiFeSO_4F$.

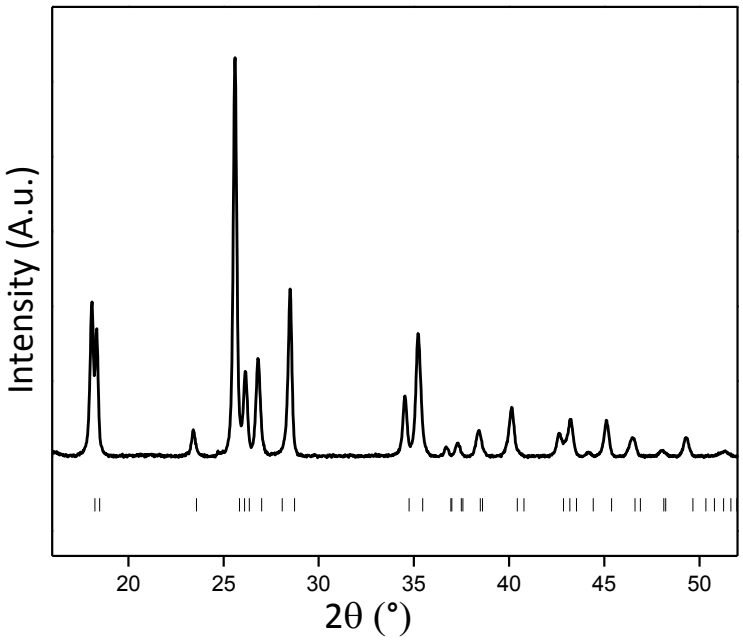

Figure 3.1 X-ray diffraction pattern of $FeSO_4 \cdot H_2O$. Black bars indicate the characteristic peak positions of the pure product derived from the cif file.

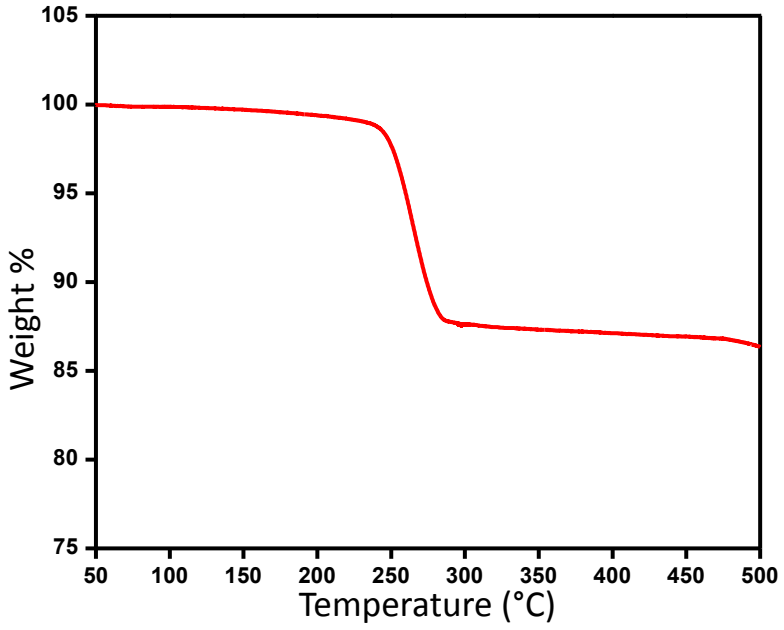

Figure 3.2 Thermo-gravimetric analysis curve of $FeSO_4 \cdot H_2O$

Mechanism of the reaction can be understood by assuming that it initiates by exchange of H and OH moieties of surface $FeSO_4 \cdot H_2O$ by Li and F respectively. Ion exchange on the surface is followed by rotation of the framework to form tavorite type $LiFeSO_4F$. Thus, an interphase boundary is formed between $FeSO_4 \cdot H_2O$ and newly formed tavorite type $LiFeSO_4F$ on the surface. This phase front moves inwards as the reaction progresses and when the interfacial stress induced by structural difference between the two phases exceeds a certain limit, crystallites of tavorite type $LiFeSO_4F$ break off from the parent $FeSO_4 \cdot H_2O$ particle. At the end of the reaction, parent $FeSO_4 \cdot H_2O$ fragments in several smaller crystallites of the tavorite type $LiFeSO_4F$. As shown later in **Chapter 5**, particle size of the tavorite type $NaFeSO_4F$ prepared by using similar precursors and methods is much smaller than tavorite type $LiFeSO_4F$. This can be explained by taking in to account the higher unit cell volume of $NaFeSO_4F$ which exerts higher stress on the product-precursor interface and therefore crystallites of smaller size break off from the surface as product $NaFeSO_4F$ than those of $LiFeSO_4F$. During the microwave synthesis this mechanism is perturbed to produce very small $LiFeSO_4F$ particles, which will be discussed later in this chapter.

The $LiFeSO_4F$ structure parameters were refined from the X-ray powder diffraction pattern with very good fitting statistics (**Figure 3.4**). The tavorite structure can be described by considering the basic units of the FeO_4F_2 octahedra and the SO_4 tetrahedra. The octahedra share corners along the *c*-axis forming parallel chains of repeating sequence Fe-F-Fe. These chains are cross linked *via* SO_4 tetrahedra in *a* and *b*-direction. Thus, each tetrahedron links three Fe-chains. Such networking among polyhedra opens up a tunnel like space along *a* and *b* directions. The tunnel provides an empty space in the framework and creates facile diffusion paths for the lithium ions. In the tavorite type structure (eg. $LiFePO_4OH$),[188] Li site is refined as located on

two neighboring sites which are very close to each other. In $LiFeSO_4F$, Li is refined to be equally distributed (occupancy: 0.5) between these 2 sites which are 0.80 Å away from each other. Some reports also exist where Li in tavorites has been refined on a single site (such as in $LiGaPO_4OH$),[189] however the X-ray diffraction data did not allow such distinction and the $LiFeSO_4F$ X-ray refinement "goodness of fit" parameters remain unchanged whether Li is refined by the former model or the later. Adjacent octahedra in the Fe-F-Fe chain are rotated with respect to each other by approximately 22° and neighboring Fe-atoms occupy crystallographically distinct sites. Refined structural parameters are presented in **Table 3.1**. **Table 3.2** presents a summary of bond lengths obtained from the refinement. SEM and EDX results are summarized in **Figures 3.5** and **3.6.**

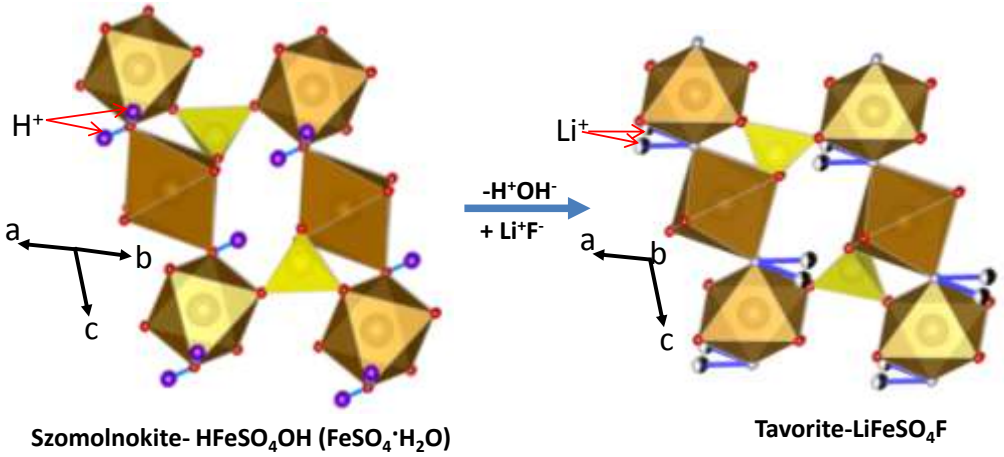

Figure 3.3 Comparison of szomolnokite and tavorite structures. FeO_6 (in $FeSO_4{\cdot}H_2O$) and FeO_4F_2 (in $LiFeSO_4F$) coordination polyhedra are shown in brown. SO_4^{2-} tetrahedra are in yellow. Oxygen atoms are shown in red and fluorine atoms in grey.

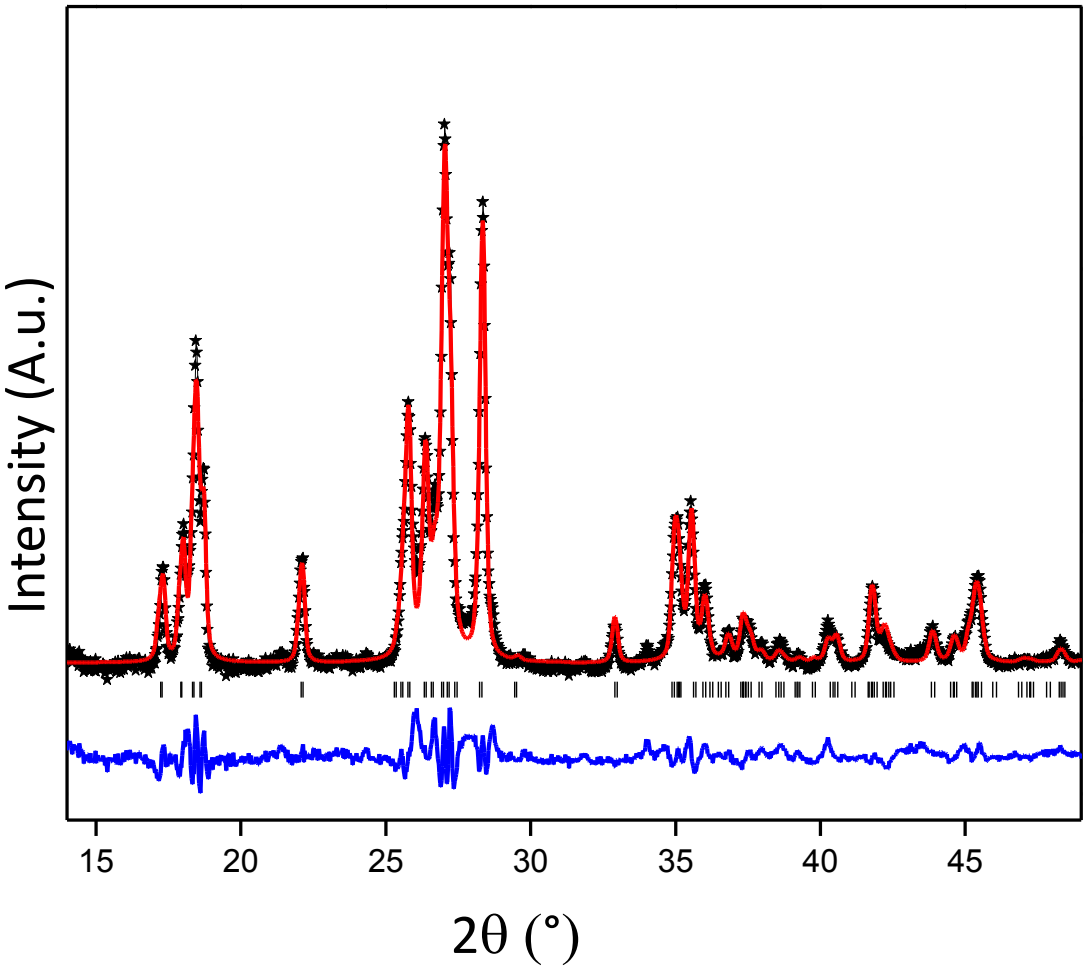

Figure 3.4 Powder X-ray diffraction refinement of tavorite type $LiFeSO_4F$ prepared *via* conventional solvothermal method. Black points represent experimental data, red solid lines show fitted data while blue lines show the difference map between observed and calculated data. Black bars indicate phase markers. X-ray diffraction agreement factors R_{wp} = 8.94%, R_p = 6.95%, R_F^2 = 7.25%.

Table 3.1 Structural data obtained by refinement from powder XRD pattern of the tavorite type $LiFeSO_4F$ prepared by conventional solvothermal methods

ST-$LiFeSO_4F$						
Space group: *P* -1 (#2), Triclinic M_w = 177.85 g/mol D = 3.230 g cm^{-3}						
a = 5.1751(1) Å *b* = 5.4915(1) Å *c* = 7.2211(2) Å α = 106.506(2)° β = 107.178(2)° γ = 97.865(2)° V = 182.440(5) $Å^3$						
Atom	**Wyck.**	***x/a***	***y/b***	***z/c***	**Occ.**	***U_{iso}* (Å^2)**
Li(1)	2*i*	0.35(1)	0.67(1)	0.82(1)	0.5	0.015(2)
Li(2)	2*i*	0.18(1)	0.61(1)	0.73(1)	0.5	0.015(3)
Fe(1)	1*a*	0	0	0	1.0	0.007(5)
Fe(2)	1*b*	0	0	1/2	1.0	0.007(6)
S	2*i*	0.3197(6)	0.6318(6)	0.2490(5)	1.0	0.009(8)
O(1)	2*i*	0.599(1)	0.745(1)	0.4074(9)	1.0	0.015(2)
O(2)	2*i*	0.104(1)	0.6334(9)	0.3470(9)	1.0	0.012(2)
O(3)	2*i*	0.319(1)	0.353(1)	0.1428(9)	1.0	0.013(2)
O(4)	2*i*	0.288(1)	0.778(1)	0.106(1)	1.0	0.016(2)
F	2*i*	0.1323(9)	0.910(1)	0.7578(8)	1.0	0.012(2)

Table 3.2 Bond lengths obtained by refinement from powder XRD pattern of tavorite type $LiFeSO_4F$ prepared by conventional solvothermal methods

Atom 1	Atom 2	Multiplicity	Length (Å)
Fe(2)	F(1)	2x	2.0013(2)
	O(3)	2x	2.1196(2)
	O(4)	2x	2.1127(2)
Fe(1)	F(1)	2x	2.0013(2)
	O(1)	2x	2.1713(2)
	O(2)	2x	2.1855(2)
S(1)	O(1)	1x	1.4045(2)
	O(4)	1x	1.4556(2)
	O(2)	1x	1.4576(3)
	O(3)	1x	1.5165(3)
Li(1)	Li(2)	1x	0.8059(6)
	O(3)	1x	1.6731(3)
	F(1)	1x	1.9786(2)
	O(4)	1x	2.1773(3)
	O(2)	1x	2.4748(2)
	O(1)	1x	2.5156(2)
Li(2)	Li(1)	1x	0.8059(6)
	F(1)	1x	1.7565(2)
	O(2)	1x	1.8069(9)
	O(3)	1x	2.3147(4)
	O(1)	1x	2.4353(1)
	O(4)	1x	2.5287(1)

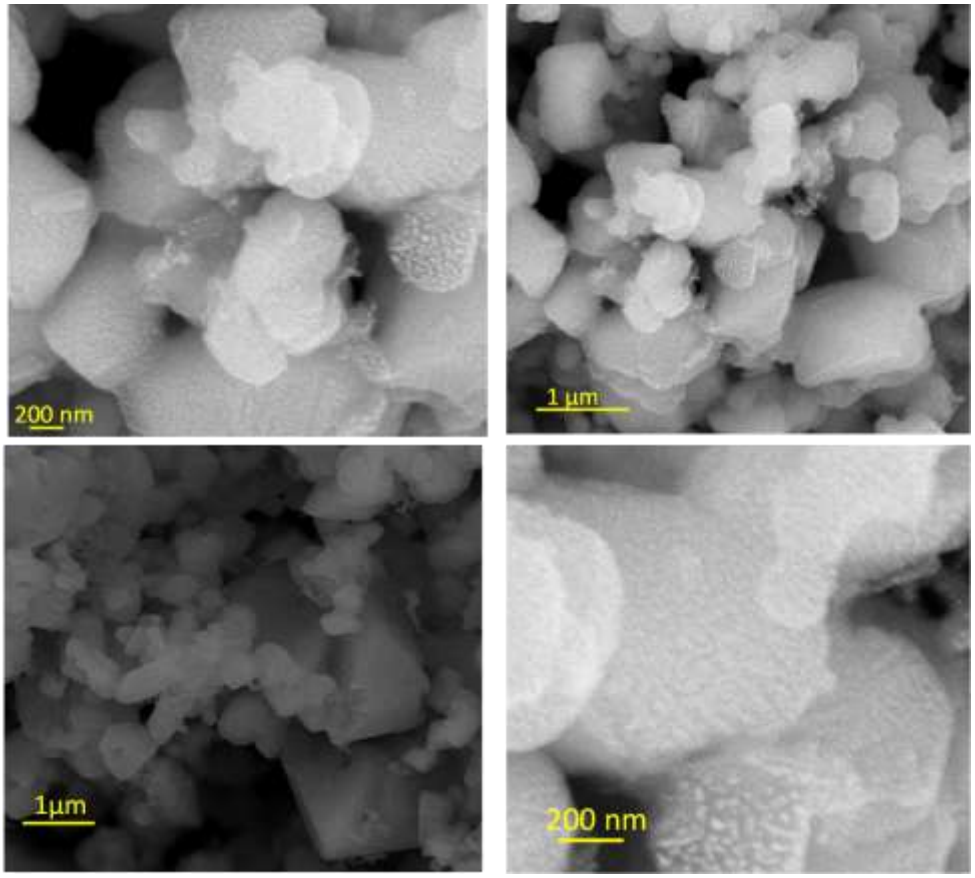

Figure 3.5 SEM images of tavorite type $LiFeSO_4F$ prepared by conventional solvothermal method.

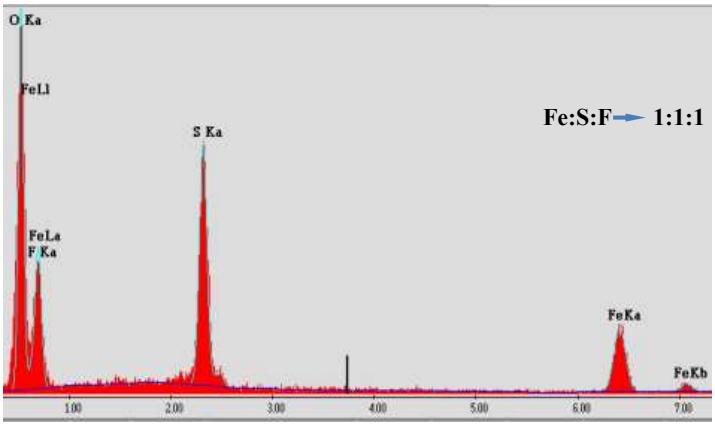

Figure 3.6 EDX spectra obtained from tavorite type $LiFeSO_4F$

Figure 3.7 shows a selected region of the XRD pattern of $LiFeSO_4F$ prepared by microwave heating of the precursors in tetraethylene glycol (TEG) for 10 minutes. The characteristic reflections identify it as a tavorite type compound and clearly differentiate from the starting material $FeSO_4 \cdot H_2O$. The SEM images show randomly shaped particles with sizes ranging from 100 to 200 nm (**Figure 3.8**). As discussed in **Chapter 2** microwave heating occurs through interaction with the chemical bonds and therefore thermal gradients during the synthesis are absent. In addition, rapid heating ensures that higher number of new phase nuclei appear on the surface of the precursor and grow to become separate crystallites as discussed previously. Thus, higher rate and uniform heating during microwave synthesis results in smaller sized crystallites. Very rapid crystallizations also does not allow the strain generated during the topotactic exchange of atoms to be completely relieved and therefore the diffraction pattern of the microwave-prepared tavorite type $LiFeSO_4F$ (MW-ST) exhibits noticeably different peak shapes compared to those of the solvothermal tavorite (ST). Comparison of the diffraction patterns of the microwave and solvothermal tavorite also reveals intensity redistribution that cannot be described by cation disorder. The low symmetry (SG*: P-1*) and moderate x-ray fluorescence from iron in the sample preclude detailed analysis of microstrain and texture in the MW tavorite and a reasonable fit could not be obtained.

3.3.3 Triplite-Type-$LiMSO_4F$

Phases and compounds obtained by ion-exchange or topotactic replacement of the atoms are generally metastable in nature. The conventional solvothermal reaction of tavorite $LiFeSO_4F$ when extended over few weeks at 250°C precipitates as a completely new phase (**Figure 3.9**). Clearly, the tavorite type $LiFeSO_4F$ slowly converts into another phase. It takes 2 weeks to complete the conversion of the tavorite in to this new polymorph of the $LiFeSO_4F$ which adopts

triplite type mineral framework. The triplite framework is adopted by (Mn,Fe)PO_4F family of mineral compounds. The structure is formed by edge shared metal-octahedra networked with SO_4 tetrahedra *via* corner sharing. Unlike tavorites, triplites have additional symmetry elements and they are classified under monoclinic space group *C*2/*c*. Unlike $LiFeSO_4F$, triplite $LiMnSO_4F$ could be obtained only after 2-days of conventional-solvothermal reaction between LiF and $MnSO_4 \cdot H_2O$ at 220°C. Tavorite type $LiMnSO_4F$ could not be obtained using solvothermal methods.

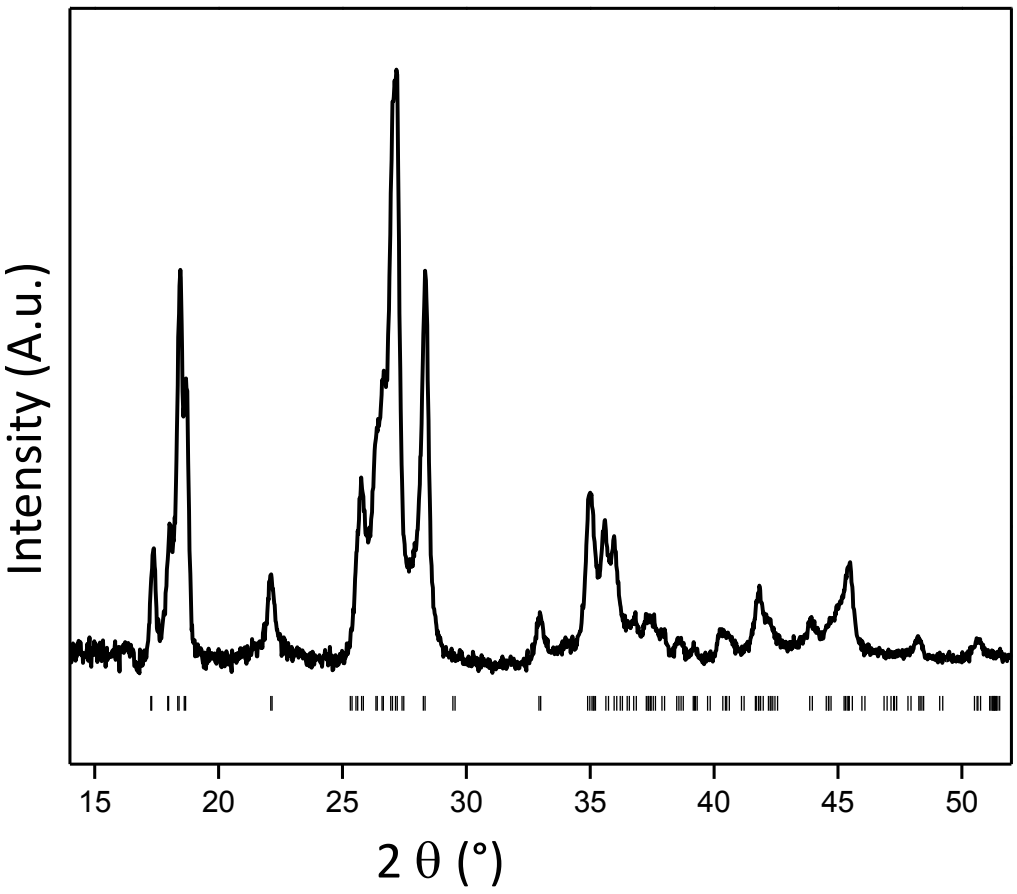

Figure 3.7 X-ray diffraction pattern of tavorite $LiFeSO_4F$ prepared *via* microwave solvothermal method. Black bars indicate the peak positions for the tavorite phase

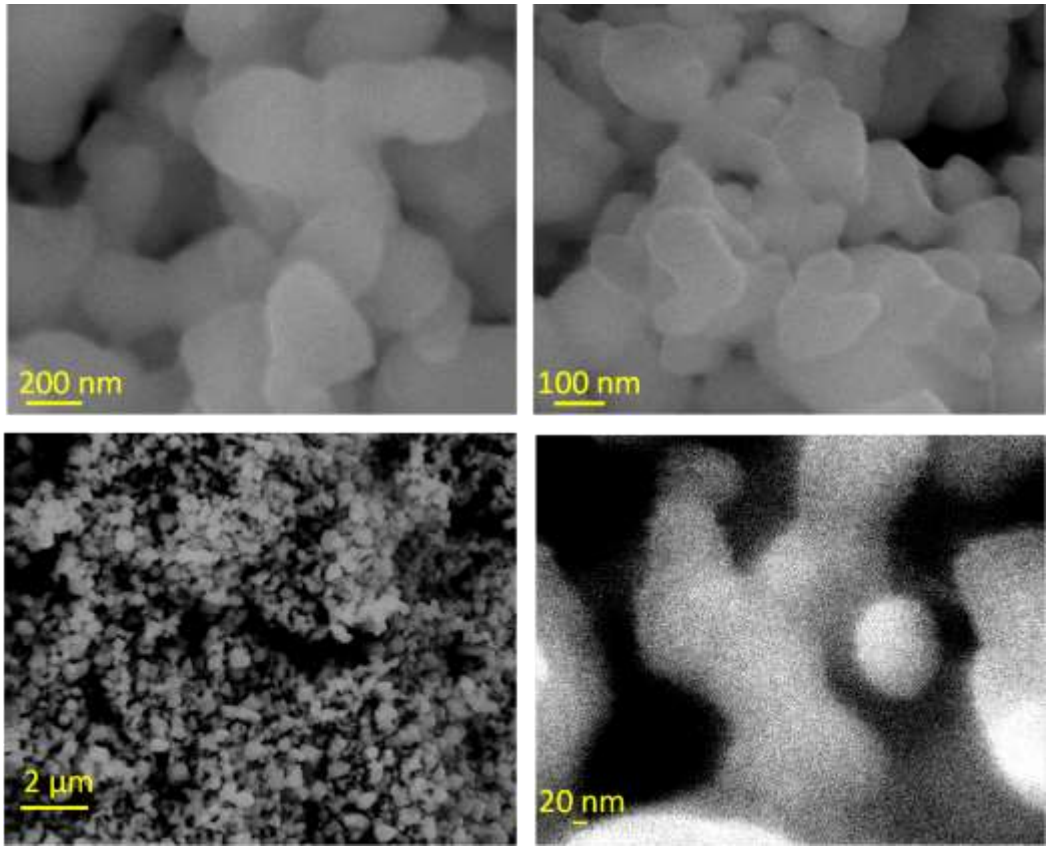

Figure 3.8 SEM images of the tavorite $LiFeSO_4F$ product obtained by microwave assisted solvothermal methods.

To study the impact of the transition metals on the structural preference of the $LiMSO_4F$, compounds of general composition $LiFe_{1-x}M_xSO_4F$ (M=Mn, Zn) were synthesized. Zinc was chosen as the other substituent because $LiZnSO_4F$ has been shown to crystallize in orthorhombic space group and is isostructural with sillimanite type compounds[190] which are different from either of the tavorite or triplite. **Figure 3.10** shows the X-ray pattern of the products obtained after conventional solvothermal reaction at 250°C for 3 ($x \neq 0$) to 14 ($x = 0$) days. No reaction was detected at temperatures lower than 250˚C for "$0.1 \leq x < 1$" indicating that triplites form at

slightly higher temperature. For $x \leq 0.1$, the product remained tavorite and for x=1 and M=Mn ($LiMnSO_4F$), the product was triplite. No tavorite intermediate could be isolated for $x \geq 0.1$ in $LiFe_{1-x}Mn_xSO_4F$. Eventual formation of triplite for any value of the composition parameter x establishes this as the thermodynamically favored phase for fluorosulfate compounds. **Figure 3.11** shows the SEM images for these samples.

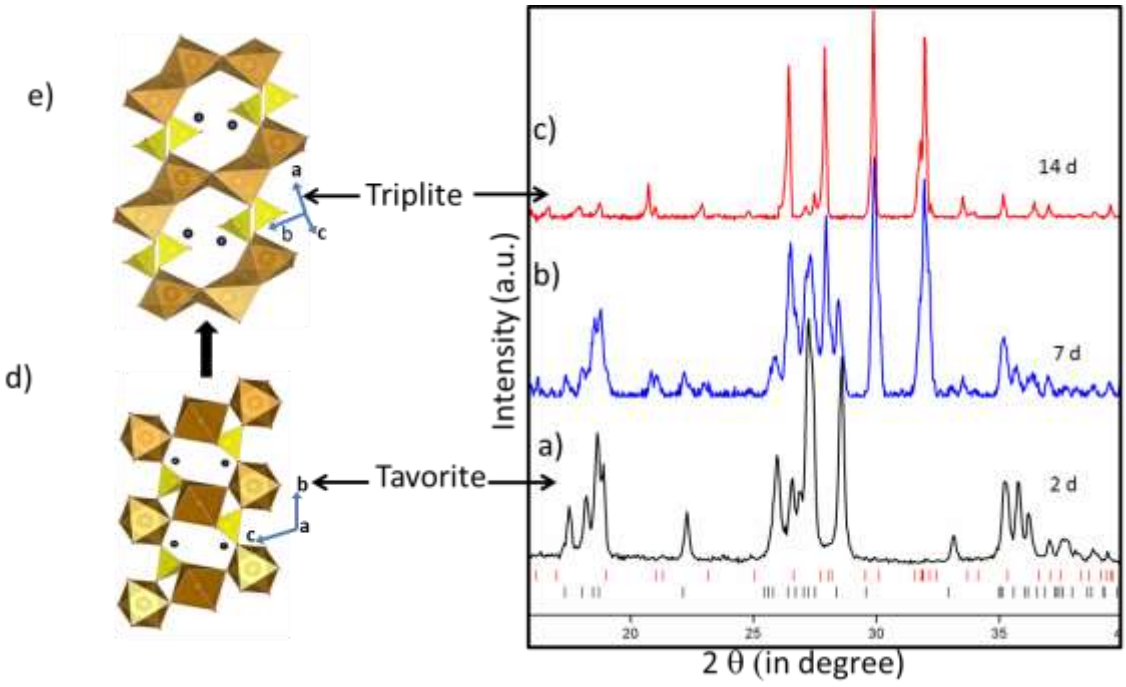

Figure 3.9 X-ray diffraction patterns of LiF and $FeSO_4 \cdot H_2O$ mixture in TEG obtained at different reaction time under conventional solvothermal reaction conditions: a) 2-days of reaction time; b) 7-days of reaction time; b) 14-days of reaction time; d) representation of tavorite crystal structure; f) representation of triplite crystal structure; FeO_4F_2 octahedra are represented in brown and SO_4 tetrahedra in yellow and black spheres represent Li atoms.

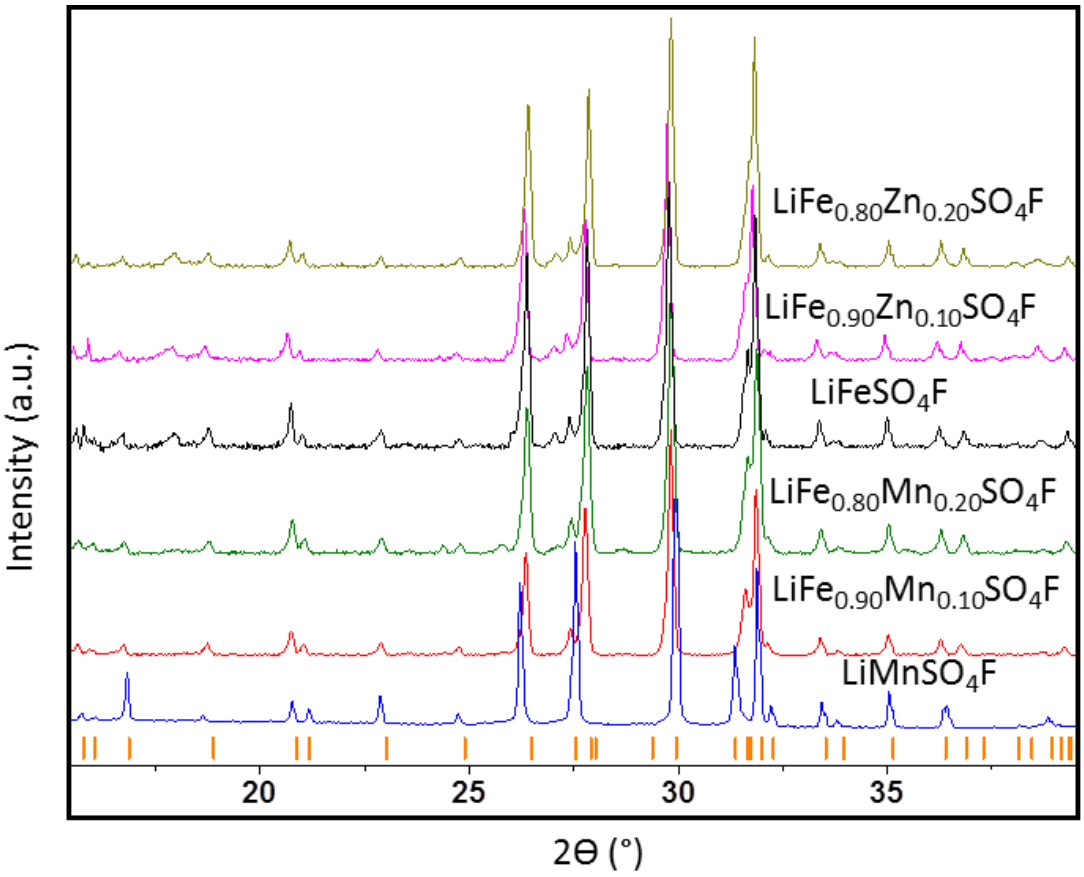

Figure 3.10 X-ray patterns of various triplite compounds prepared under conventional solvothermal conditions. Orange bars represent phase markers for triplite $LiMnSO_4F$

Under the microwave solvothermal synthesis conditions triplite $LiFeSO_4F$ cannot be obtained directly in the microwave even after heating the reaction mixture up to 300°C and 3 hours. However, pure phase triplite type $LiFeSO_4F$ can be obtained by very short heat treatment (as little as one hour) of microwave prepared tavorite type $LiFeSO_4F$ at 350°C. Tavorite type $LiFeSO_4F$ samples prepared by methods other than microwave assisted synthesis does not undergo such rapid conversion.

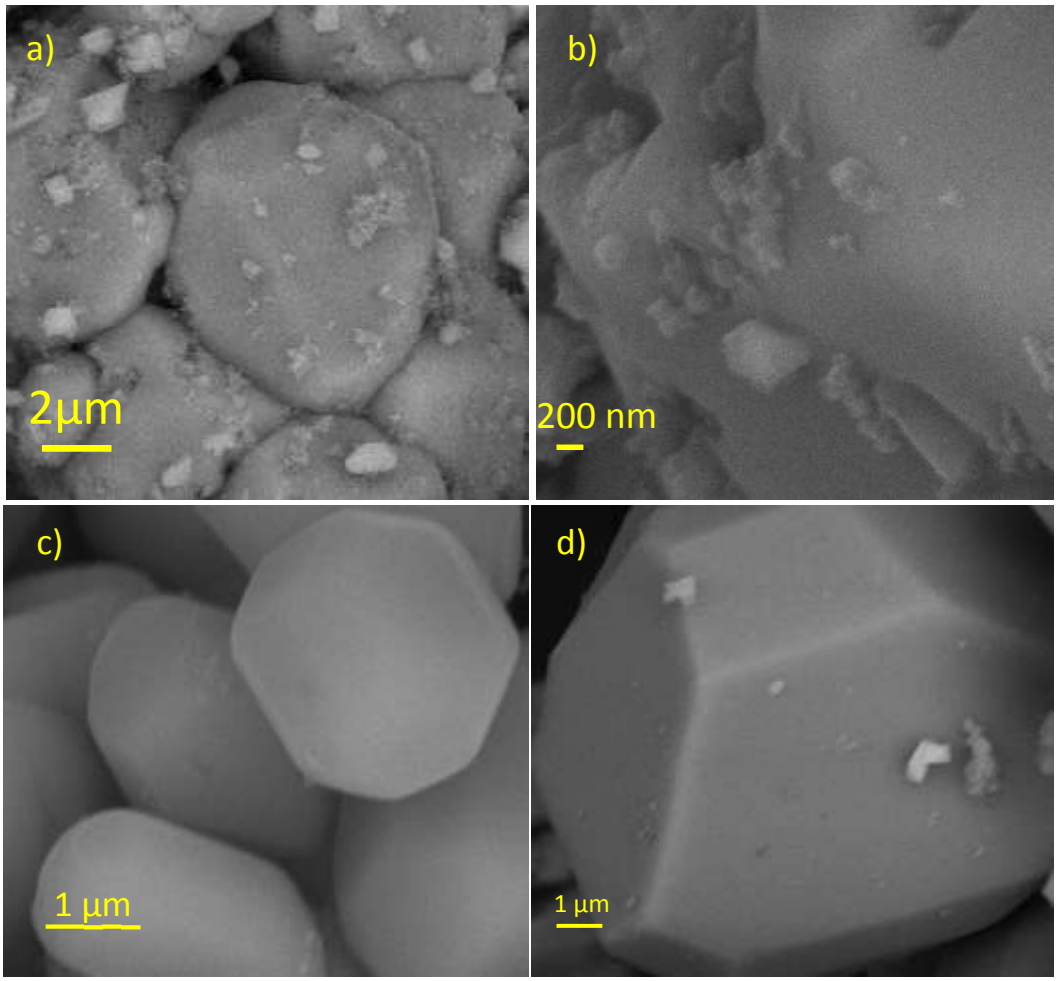

Figure 3.11 SEM images of various triplite $LiFe_{1-x}(Mn,Zn)_xSO_4F$ ($0 \leq x < 1$)obtained *via* conventional solvothermal method; a) and b) triplite $LiFeSO_4F$; c) triplite $LiFe_{0.8}Mn_{0.2}SO_4F$; d) $LiFe_{0.8}Zn_{0.2}SO_4F$

Figure 3.12 compares the impact of the heat treatment (at 350°C) on tavorite $LiFeSO_4F$ prepared by microwave and conventional solvothermal methods. The latter do not show any phase transformation after heat treatment for one hour; a prolonged heat treatment of 12 hours is necessary which also results in significant formation of extraneous iron oxides. These impurities have been reported to form during direct solid state synthesis of the triplite type $LiFeSO_4F$ using a 1:1 ratio of LiF and $FeSO_4 \cdot H_2O$.[191] The complete lack of impurities in the microwave-assisted

preparation of triplite type $LiFeSO_4F$ suggests that the kinetics governing the conversion of tavorite to triplite type compound is dramatically enhanced. This provides a very easy and scalable route for the synthesis of the triplite type $LiFeSO_4F$. Rietveld fit of the X-ray diffraction pattern obtained by refining microwave prepared triplite type $LiFeSO_4F$ are shown in **Figure 3.13** and the structural data is reported in **Table 3.3** and **Table 3.4.**

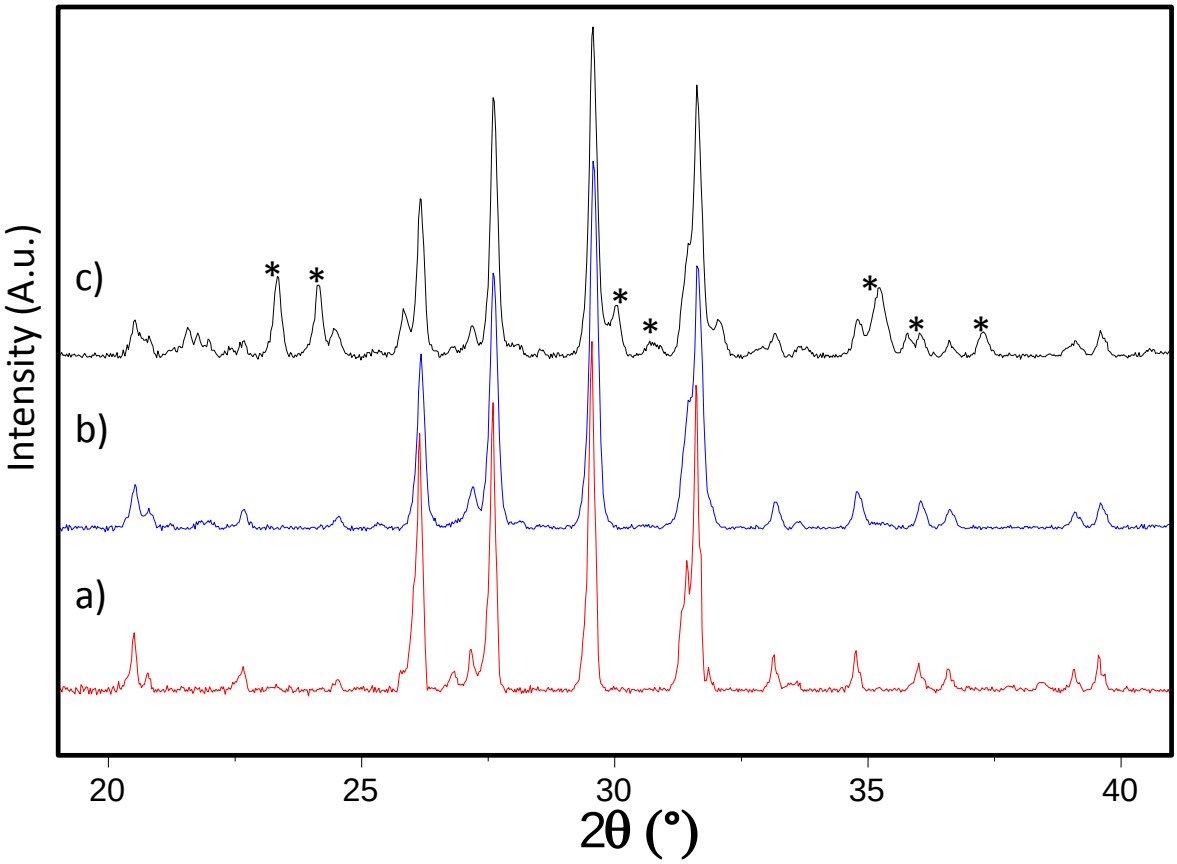

Figure 3.12 Comparison of X-ray diffraction pattern of triplite $LiFeSO_4F$ prepared by a) Heating tavorite type $LiFeSO_4F$ obtained from microwave synthesis at 350°C for 1 hr under Ar. b) extending conventional solvothermal synthesis for 2 weeks c) heating tavorite $LiFeSO_4F$ obtained by conventional solvothermal at 350°C for 12 hr under Ar. Asterisk (*) represents oxide and sulfide impurity peaks.

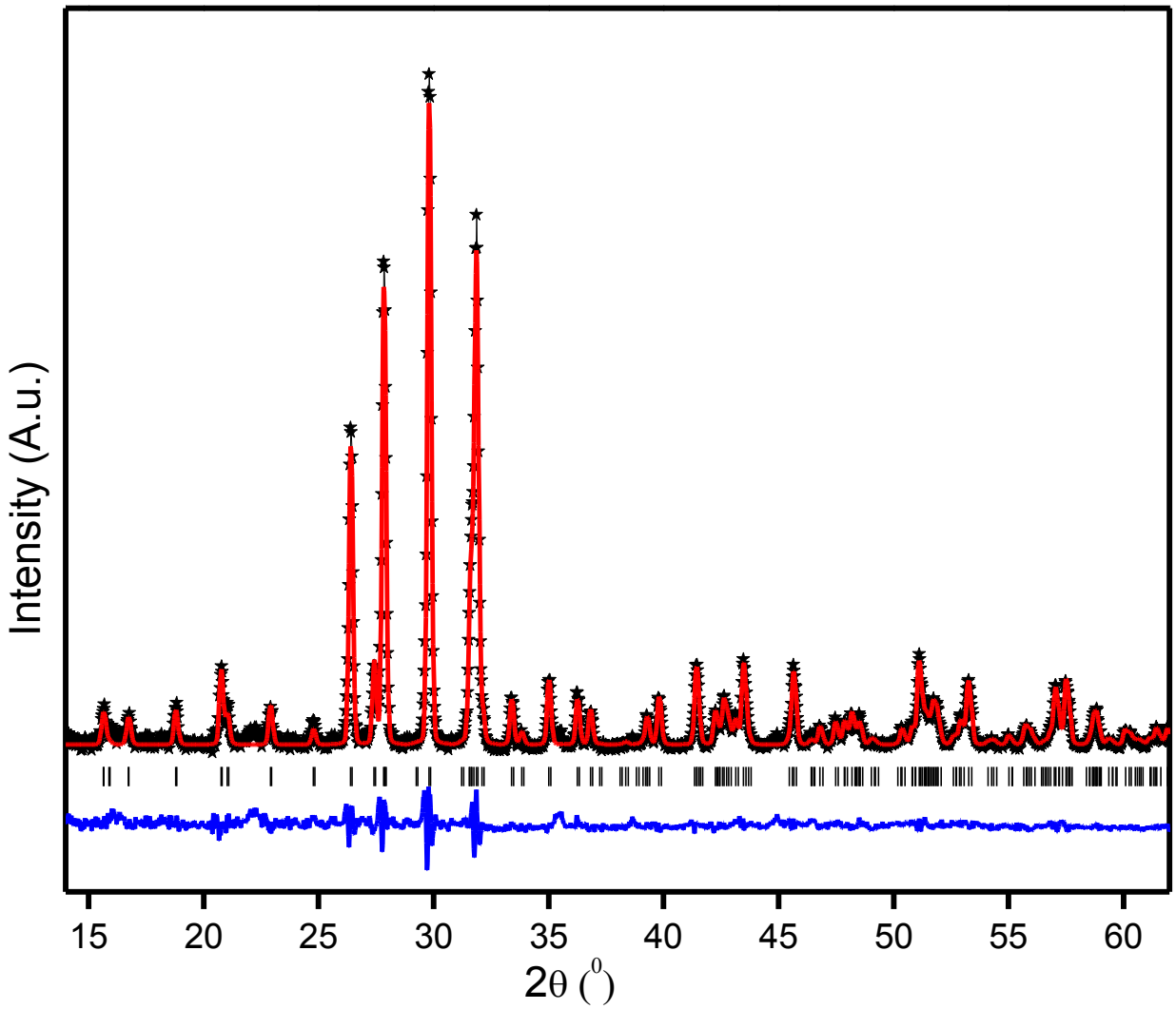

Figure 3.13 Powder X-ray diffraction refinement of the triplite type $LiFeSO_4F$ obtained by microwave assisted process. Black points represent experimental data, red solid lines show fitted data while blue lines show the difference map between observed and calculated data. Black bars indicate phase markers. X-ray diffraction agreement factors: R_{wp} = 3.16%,R_p=1.34%, χ^2 = 3.15.

The structure refinement studies of the triplite type $LiFe_{1-x}Mn_xSO_4F$ were based on the initial model of triplite mineral Mn_2PO_4F. Structures of $LiFe_{0.5}Mn_{0.5}SO_4F$, $LiFe_{0.8}Mn_{0.2}SO_4F$ and $LiFe_{0.9}Mn_{0.1}SO_4F$ were refined using combined (i.e. simultaneously refined) neutron and X-ray diffraction data. Owing to the very different scattering lengths in each couple, the ability of

neutron diffraction to discriminate easily between Li and Fe (-1.9 and 9.4 fm respectively) and Fe and Mn (9.4 and -3.7 fm respectively) and the ability of X-ray diffraction to distinguish readily between the light Li and the heavy transition metals was utilized. A complete picture of the cation order/disorder for all three cations could thus be obtained. The XRD and neutron diffraction patterns and refined data for $LiFe_{0.8}Mn_{0.2}SO_4F$ are shown in **Figure 3.15** as an example. The results of the Rietveld refinement are summarized in **Table 3.5**.

Considered as a whole, the diffraction studies reveal that there is no significant ordering of Li/Fe/Mn on the two M1 and M2 sites in any of the materials. For $LiFe_{0.2}Mn_{0.8}SO_4F$, the refinement reveals a slight ordering of 0.57 Li (site 2)/0.43 Li (site 1), which is a little more developed in $LiFe_{0.1}Mn_{0.9}SO_4F$ to give an ordering of 0.59 Li (site 2)/0.41 Li (site 1). This is not that different from ‘‘fully’’ (i.e. 50/50) disordered triplite $LiMnSO_4F$ (**Table 3.5**). A previous Mössbauer study on natural triplite $(Mn,Fe)_2PO_4F$ and related minerals also found a lack of significant ion ordering on the M1 and M2 sites.[192] That study detected that the smaller ion had a slight preference for the M2 site, in accord with our refinement results where the smallest ion (Li^+) shows a minor preference for the M2 site. In short, although we observe a distinct, very non-linear trend that shows that Li prefers site 2 as the Fe content increases this is far from the degree of ordering that we might expect would strongly affect Li-ion mobility. The fact that the pure iron triplite phase $LiFeSO_4F$ which has the highest theoretical gravimetric capacity of the series exhibits the least practical capacity suggests that other factors are also at play (see below).

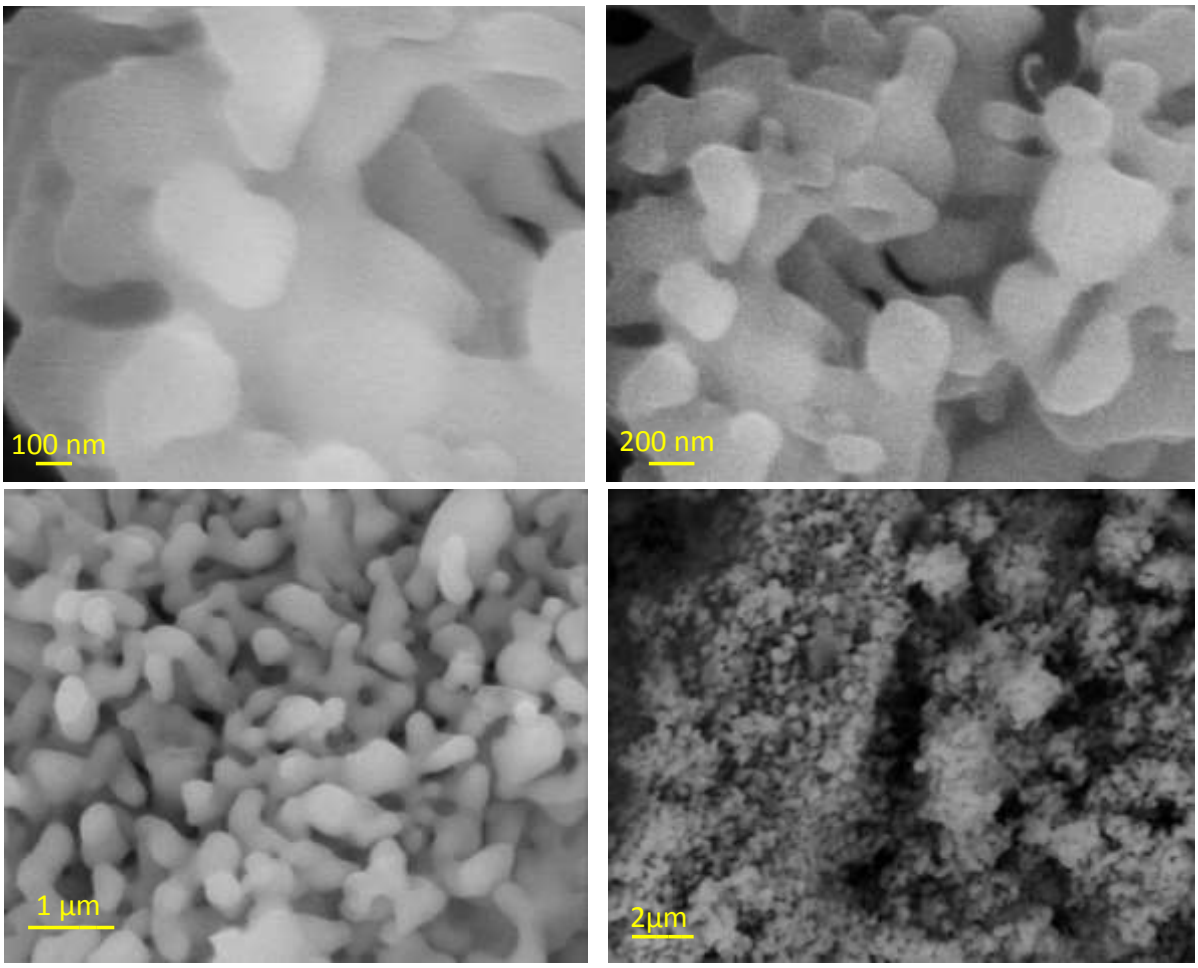

Figure 3.14 SEM images of triplite type $LiFeSO_4F$ obtained by microwave assisted process.

Table 3.3 Structure data obtained by refinement from powder XRD pattern of triplite $LiFeSO_4F$

Triplite-LiFeSO4F						
Space group: *C* 2/*c* (#15), Monoclinic M_w = 177.85 g/mol D = 3.330 g cm^{-3}						
a = 13.0328(1) Å *b* = 6.3936(1) Å *c* = 9.8413 (1) Å *β* = 119.750(3)° V = 711.960(8) $Å^3$						
Atom	**Wyck.**	***x/a***	***y/b***	***z/c***	**Occ.**	U_{iso}(Å^2)
Fe(1)	8*f*	0.6469(2)	0.8947(4)	0.8475(3)	0.574(2)	0.0215(8)
Fe(2)	8*f*	0.9473(3)	0.2482(5)	0.0007(4)	0.426(2)	0.027(1)
S(1)	8*f*	0.3279(2)	0.5923(4)	0.1967(3)	1.0	0.0271(7)
O(1)	8*f*	0.2150(3)	0.63399(4)	0.1929(3)	1.0	0.0430(1)
O(2)	8*f*	0.5792(3)	0.5354(4)	0.1443(3)	1.0	0.0239(8)
O(3)	8*f*	0.6928(2)	0.4155(5)	0.4138(3)	1.0	0.0236(8)
O(4)	8*f*	0.6350(3)	0.7720(4)	0.3589(3)	1.0	0.0234(8)
F(1)	8*f*	0.9867(3)	0.4037(6)	0.6091(4)	1.0	0.0209(7)
Li(1)	8*f*	0.6469(2)	0.8947(4)	0.8475(3)	0.426(2)	0.0215(8)
Li(2)	8*f*	0.9473(3)	0.2482(5)	0.0007(4)	0.574(2)	0.0270(1)

Table 3.4 Summary of bond lengths obtained by refinement from PXRD of triplite-type-$LiFeSO_4F$

Atom 1	Atom2	Multiplicity	Bond Length
Fe(2)/Li(2)	F(1)	1x	1.9710(8)
	O(2)	1x	2.0712(6)
	O(1)	1x	2.1165(6)
	O(4)	1x	2.1494(9)
	F(1)	1x	2.1984(8)
	O(1)	1x	2.4335(8)
Li(1)/Fe(1)	F(1)	1x	1.9713(8)
	O(3)	1x	2.0964(8)
	O(2)	1x	2.1077(9)
	O(4)	1x	2.1701(7)
	O(3)	1x	2.2278(5)
	F(1)	1x	2.2591(5)
S(1)	O(4)	1x	1.4457(8)
	O(1)	1x	1.4685(8)
	O(2)	1x	1.5079(6)
	O(3)	1x	1.5120(9)

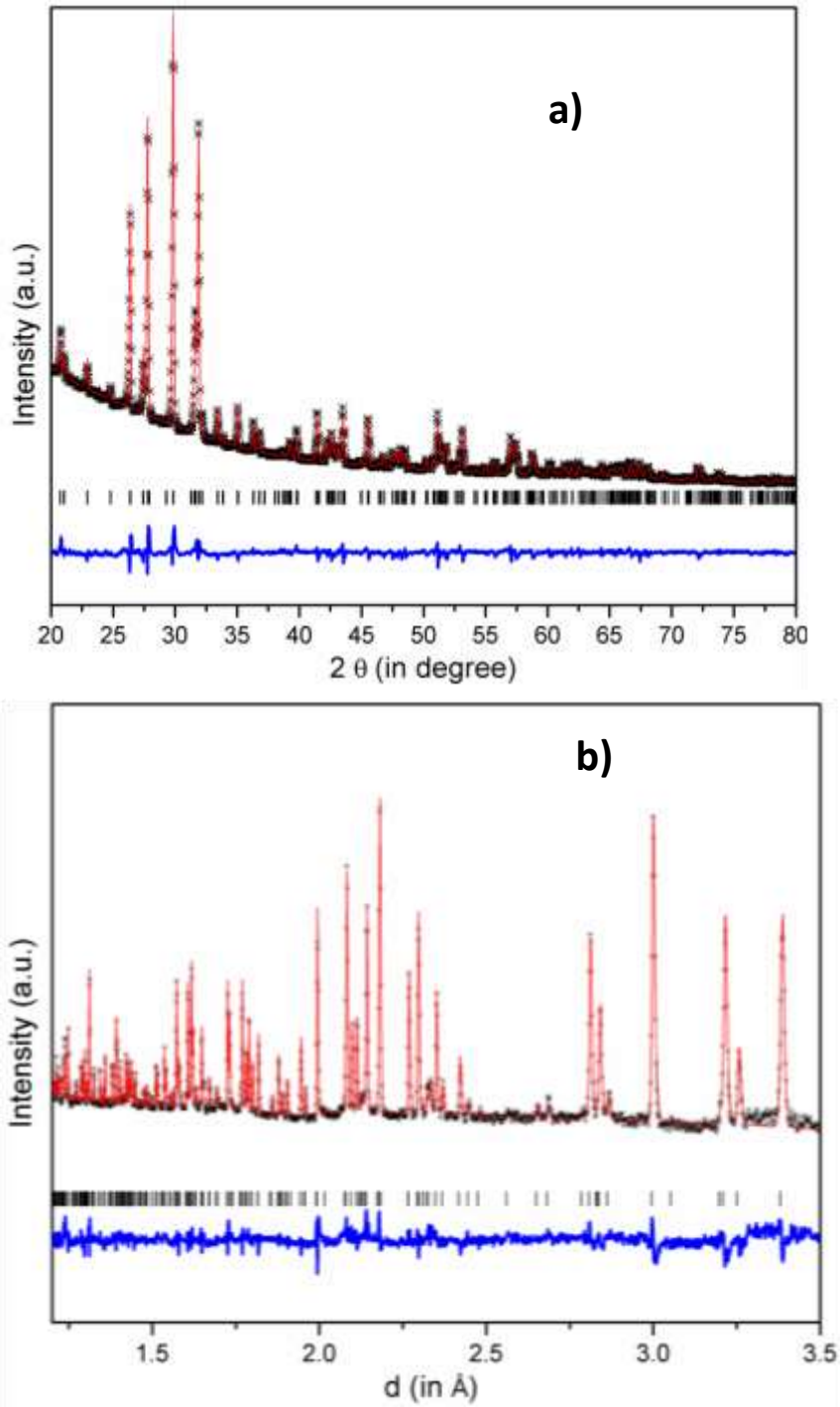

Figure 3.15 Combined a) X-ray and b) neutron refinement of $LiFe_{0.8}Mn_{0.2}SO_4F$. Black points represent experimental data, red solid lines show fitted data while blue lines show the difference map between observed and calculated data. Black bars indicate phase markers. Combined (X-ray and neutron) diffraction agreement factors: R_{wp} = 2.33%, R_p = 1.56%, χ^2 = 5.9.

Table 3.5 Refined structural parameters of $LiMnSO_4F$, $LiFe_{0.5}Mn_{0.5}SO_4F$, $LiFe_{0.8}Mn_{0.2}SO_4F$ and $LiFe_{0.9}Mn_{0.1}SO_4F$. Rietveld analyses of powder neutron and X-ray diffraction data were done in the *C*2/*c* space group.

		$LiMnSO_4F$ 300K XRD	$LiFe_{0.5}Mn_{0.5}SO_4F$ 300K XRD + neutron combined	$LiFe_{0.8}Mn_{0.2}SO_4F$ 300K XRD + neutron combined	$LiFe_{0.9}Mn_{0.1}SO_4F$ 300K XRD + neutron combined
a (Å)		13.2406(2)	13.1150(2)	13.0713(2)	13.0539(8)
b (Å)		6.4082(1)	6.3889(1)	6.3958(1)	6.3945(4)
c (Å)		10.0229(2)	9.9077(2)	9.8735(2)	9.8577(6)
β (deg)		120.499(1)	120.187(1)	119.891(1)	119.830(1)
V (Å^3)		732.76(3)	717.59(3)	715.63(3)	713.8(1)
Li(1)/ Fe(1)/Mn(1)	Occ.	0.484(3)/ 0/0.516(3)	0.433(8)/ 0.318(2)/0.249(2)	0.430(3)/ 0.475(3)/0.095(3)	0.434(4)/ 0.483+0.083(4)
	x/a	0.6474(3)	0.6484(9)	0.6462(2)	0.6462(4)
	y/b	0.8942(5)	0.896(2)	0.8934(5)	0.8935(8)
	z/c	0.8449(3)	0.853(2)	0.8473(3)	0.8470(5)
	U_{iso} (Å^2) Li/(Fe,Mn)	0.029(1)	0.015(1)	0.026(1)	0.036(2)
Li(2)/ Fe(2)/Mn(2)	Occ.	0.516(3)/ 0/0.484(3)	0.567(8)/ 0.182(2)/0.251(2)	0.570(3)/ 0.325(3)/0.105(3)	0.566(4)/ 0.417+0.017(4)
	x/a	0.9481(2)	0.979(4)	0.9475(3)	0.9484(5)
	y/b	0.2526(5)	0.336(6)	0.2516(7)	0.246(1)
	z/c	0.0068(3)	0.036(5)	0.0025(5)	0.0050(7)
	U_{iso} (Å^2) Li/(Fe,Mn)	0.022(1)	0.015 (1)	0.031(1)	0.046(3)
S	*x/a*	0.3271(3)	0.3262(4)	0.3276(3)	0.3287(5)
	y/b	0.5912(4)	0.5923(7)	0.5936(5)	0.5909(8)
	z/c	0.1976(3)	0.1936(5)	0.1966(3)	0.1981(5)
	U_{iso} (Å^2)	0.0280(6)	0.0084(8)	0.0307(9)	0.035(2)
F	*x/a*	0.9849(4)	0.9865(2)	0.9864(3)	0.9828(7)
	y/b	0.4001(8)	0.4053(4)	0.4042(5)	0.408(1)
	z/c	0.6079(4)	0.6093(3)	0.6089(3)	0.6113(8)
	U_{iso} (Å^2)	0.024(1)	0.0159(6)	0.040(1)	0.054(4)
O(1)	*x/a*	0.2132(4)	0.2152(2)	0.2157(3)	0.218(1)
	y/b	0.6426(8)	0.6424(3)	0.6406(4)	0.650(2)
	z/c	0.1857(5)	0.1913(2)	0.1918(3)	0.1863(9)
	U_{iso} (Å^2)	0.023(2)	0.0072(5)	0.0261(8)	0.052(5)
O(2)	*x/a*	0.5811(5)	0.5809(2)	0.5808(2)	0.5826(9)
	y/b	0.5363(8)	0.5344(3)	0.5358(4)	0.530(1)
	z/c	0.1451(6)	0.1456(3)	0.1448(3)	0.143(1)
	U_{iso} (Å^2)	0.020(2)	0.0070(4)	0.0264(8)	0.016(3)

O(3)	*x/a*	0.6949(4)	0.6930(2)	0.6921(2)	0.6961(6)
	y/b	0.4189(8)	0.4164(4)	0.4162(5)	0.415(2)
	z/c	0.4152(5)	0.4132(2)	0.4127(3)	0.4134(9)
	U_{iso} (Å^2)	0.022(2)	0.0072(5)	0.0280(9)	0.024(3)
O(4)	*x/a*	0.6338(4)	0.6345(2)	0.6352(2)	0.6386(8)
	y/b	0.7765(8)	0.7756(3)	0.7744(4)	0.774(1)
	z/c	0.3545(5)	0.3588(2)	0.3576(3)	0.3573(9)
	U_{iso} (Å^2)	0.019(2)	0.0070(5)	0.0242(8)	0.014(3)
χ^2		2.31	2.79	5.90	5.66
R_p (%)		1.50	3.02	1.56	1.31
R_{wp} (%)		1.97	2.09	2.33	1.90

3.3.4 Chemical Delithiation of $LiFeSO_4F$

$LiFeSO_4F$ can be readily oxidized with $NOBF_4$ in acetonitrile to produce the delithiated framework, $FeSO_4F$. The XRD pattern obtained by chemical delithiation of tavorite type $LiFeSO_4F$ is the same as that derived through electrochemical oxidation, but is free of any contaminants arising from the cell. To obtain unequivocal structural information on this phase in order to better understand the electrochemical redox process, a diffraction pattern was collected using a synchrotron source which affords higher intensity and resolution. The diffraction pattern shown in **Figure 3.16** was indexed, and the structure readily refined in a monoclinic cell (space group *C*2/*c*). **Table 3.6** summarizes the data obtained by refinement. The chemical delithiation of triplite type $LiFeSO_4F$ results in slightly different framework than that obtained from the tavorite type compound and the resulting composition after 24 hour chemical delithiation ($Li_{0.45}FeSO_4F$) has been reported by Barpanda *et al.*[193] in *C*2/*c* space group.

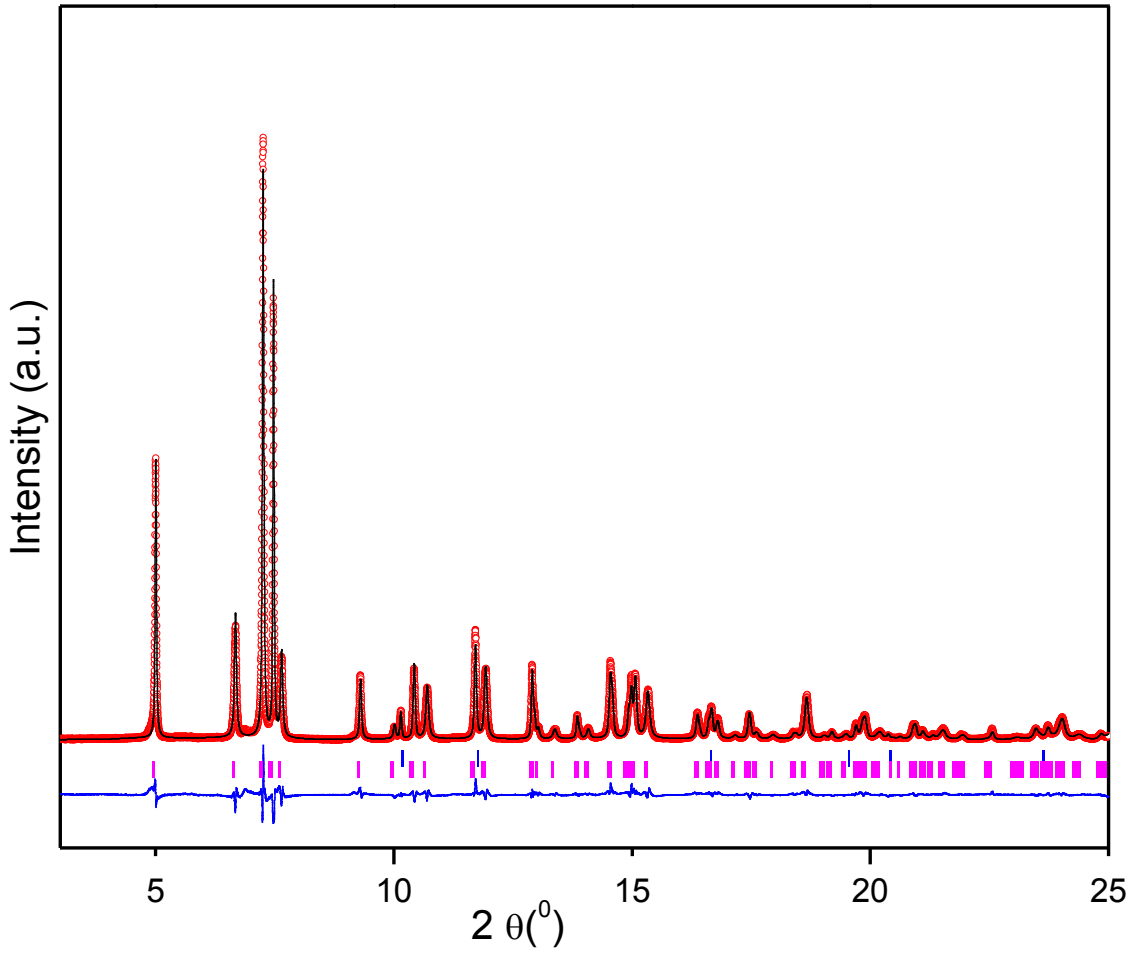

Figure 3.16 Refinement of (λ = 0.4122 Å) of $FeSO_4F$ structure from PXRD of $FeSO_4F$ obtained *via* chemical delithiation of tavorite $LiFeSO_4F$. Black points represent experimental data, red solid lines show fitted data while blue lines show the difference map between observed and calculated data; red bars indicate phase markers. X-ray diffraction agreement factors: R_{wp} = 10.30%, R_p = 8.07, R_F^2 = 9.55%

Table 3.6 Structural data of $FeSO_4F$ synthesized by chemical delithiation of tavorite type $LiFeSO_4F$

$FeSO_4F$						
Space group: *C* 2/*c* (#15), Monoclinic M_w = 170.91 g/mol D = 3.460 g cm^{-3}						
a = 7.3037(1) Å *b* = 7.0753(1) Å *c* = 7.3117(1) Å *β* = 119.758(2)° V = 328.017(8) $Å^3$						
Atom	**Wyck.**	***x/a***	***y/b***	***z/c***	**Occ.**	U_{iso} **(Å^2)**
Fe	4*d*	1/4	-1/4	0	1.0	0.0082(2)
S	4*e*	1/2	0.1357(2)	1/4	1.0	0.0087(3)
O(1)	8*f*	0.3363(3)	0.0173(2)	0.0868(4)	1.0	0.0090(6)
O(2)	8*f*	0.4030(1)	0.2571(3)	0.341(1)	1.0	0.0089(4)
F	4*e*	0	-0.1635(3)	-1/4	1.0	0.0095(7)

3.3.5 Impact of Moisture Exposure

Fluorosulfates are known to be very reactive in the presence of moisture. The impact of exposure of the $LiFe_{0.8}Mn_{0.2}SO_4F$ triplite to the atmosphere was examined, and the results are shown in **Figure 3.17**. Exposure of the tavorite type $LiFeSO_4F$ results in similar reaction. Contact at 60% relative humidity for 8 h results in the appearance of 6.5% (w/w) monohydrate $[Fe,Mn]SO_4 \cdot H_2O$ visible in the XRD pattern (**Figure 3.17**). Note that the triplite structure is closely related to tavorite which in turn is very similar to the monohydrate (‘‘szomolnokite’’) product of this reaction. Thus the reaction is likely to proceed through a transformation where the LiF moiety is replaced with H-OH by reaction of H_2O with the framework. It has been reported[194] recently that air-aging of olivine type positive electrode materials such as $LiFe^{(2+)}PO_4$ results in formation of tavorite type $LiFe^{(3+)}PO_4OH_{0.39}$ In case of fluorosulfates, due to structural

similarities, reaction with H_2O is kinetically favored for the formation of the monohydrate ferrous product before oxidation of the Fe^{2+} to Fe^{3+} occurs. Such ease of hydrolysis presents a significant problem for storage and processing of fluorosulfate materials.

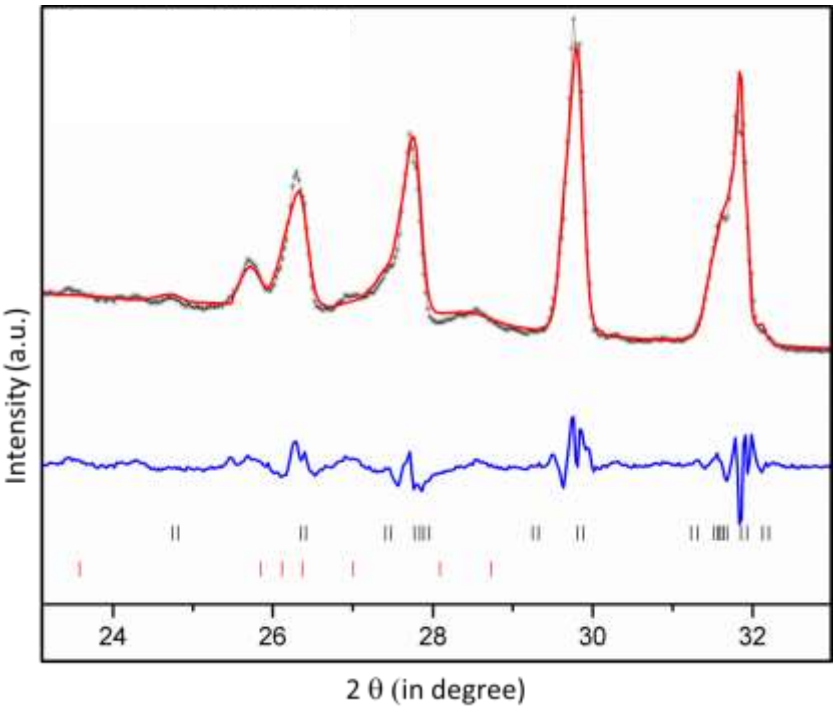

Figure 3.17 X-ray refinement of moisture exposed triplite $LiFeSO_4F$. Black points represent experimental data, red solid lines show fitted data while blue lines show the difference map between observed and calculated data. Black and red bars represent peak positions for triplite and szomolnokite phases. X-ray diffraction agreement factors: R_{wp} = 2.23%, R_p = 1.53%, χ^2 = 4.01.

3.3.6 Electrochemistry

3.3.6.1 Tavorite-Type-$LiFeSO_4F$

The high intercalation voltage and theoretical specific capacity of $LiFeSO_4F$ (151 mA h g^{-1}) has led to its proposal and realization as a suitable new positive electrode material. The electrochemical behavior of the tavorite type $LiFeSO_4F$ synthesized by conventional solvothermal method is shown in **Figure 3.18**. At C/10 rate, a reversible capacity of 0.86 Li (130 mAh g^{-1}) was sustained at an average potential of 3.6 V. This performance is similar to the tavorite type $LiFeSO_4F$ prepared by ionothermal methods.[183] Notable is that the equivalent unit cell volumes of the parent $LiFeSO_4F$ (182.4 $Å^3$), and delithiated ($FeSO_4F$: 164.0 $Å^3$) phases differ by 10.1 %. This is far greater than the volume contraction reported for the olivine $LiFePO_4 \leftrightarrow FePO_4$ of 6.7 %. Coupled with the change in unit cell symmetry, it suggests that considerable strain should be associated with the redox-driven phase transition. However, facile reversible intercalation of Li-ions without any surface carbon coating indicates that good electrochemical properties are the result of higher ionic conductivity displayed by the tavorite than olivine type structure as shown in **Chapter 4**.

3.3.6.2 Triplite-Type-$Li(Fe,Mn)SO_4F$

The electrochemical behavior of triplite type $LiFe_{0.9}Mn_{0.1}SO_4F$ prepared using conventional solvothermal technique is shown in **Figure 3.19**, the best performance is observed for materials with 5 and 10% Mn or Zn content. For $LiFe_{0.9}Mn_{0.1}SO_4F$, the theoretical gravimetric capacity is 150 mA h/ g. At a rate of 0.05C (1 Li in 20 hours) with 70% (w/w) active material in the electrode mixture, 0.70 Li could be reversibly extracted. The resulting reversible gravimetric capacity of 105 mAh g^{-1} is the same as that reported for materials prepared by the solid state

route.[195] Since Mn and Zn are reported to be electrochemically inert, the gravimetric capacity of the material increases with Fe content in the compound. A negligible reversible capacity is observed for samples with more than 50% Mn content. The electrochemistry of the Zn doped sample $LiFe_{0.9}Zn_{0.1}SO_4F$ shows significant improvement (**Figure 3.20**) over the same material prepared by using solid state methods (reversible capacity of 0.70 Li vs. 0.55 Li).[196] This can mainly be attributed to the superior phase purity of the sample obtained under solvothermal conditions, which lacks any unreacted precursors. The electrochemical properties are poorer for unsubstituted triplite type $LiFeSO_4F$ (**Figure 3.21**) prepared by conventional solvothermal synthesis compared to $LiFe_{0.9}Mn_{0.1}SO_4F$, in agreement with previous reports.[195]

The electrochemical properties of triplite type $LiFeSO_4F$ obtained from microwave-tavorite type $LiFeSO_4F$ **(Figure 3.22)** are greatly improved in comparison to the compound prepared by conventional solvothermal method. Nearly 80% of the Li could be reversibly intercalated at C/20 rate which is far better than reported for triplite $LiFeSO_4F$ (~55% Li) prepared by other methods.[193,197] This is the result of the smaller particle size afforded by the microwave process. It is well known that Li de/-intercalation kinetics can be significantly increased by using smaller particles owing to the shorter pathways required for Li-ion transport.[198] This is particularly a factor for triplite because of the disorder on the Li/Fe sites which additionally blocks the Li-migration pathways. In large particles this significantly impacts the Li ion diffusion coefficient.[198] The improvement in electrochemical properties with reduction in particle size is in accord with previous reports of inferior practical gravimetric capacity of 3-4 μm $LiFeSO_4F$ (**Figure 3.22**) compared to 1-2 μm $LiFe_{0.9}Mn_{0.1}SO_4F$ despite lower theoretical capacity of the later. The specific energy of triplite type $LiFeSO_4F$ is high despite the lower gravimetric capacity because of the increased voltage of (de)intercalation compared to other

phosphates. The average charge–discharge voltage is 300 mV higher than tavorite type $LiFeSO_4F$ and 450 mV higher than olivine $LiFePO_4$. This increased potential puts the specific energy density of triplite type $LiFeSO_4F$ on par with tavorite type $LiFeSO_4F$ and olivine type $LiFePO_4$.

Differential capacity curves for both the compounds are shown in **Figure 3.23**. The tavorite $LiFeSO_4F$ shows two oxidation and two reduction peaks in each cycle with long tails. This is in agreement with the behavior observed for ionothermally prepared tavorite sample where the smaller peak was attributed to solid solution behavior displayed by the tavorite compound at the end of oxidation and initial reduction.[193] The triplite compound, on the other hand, clearly shows only one peak indicative of first phase transformation at 3.91 V during oxidation and at 3.88 V during reduction. This is similar to the electrochemical differential capacity curve of the triplite samples prepared by solid state methods.[193] Slight loss in the peak height in both cases after few cycles is in accordance with the capacity loss with cycling shown in the inset of **Figures 3.18** and **3.19.**

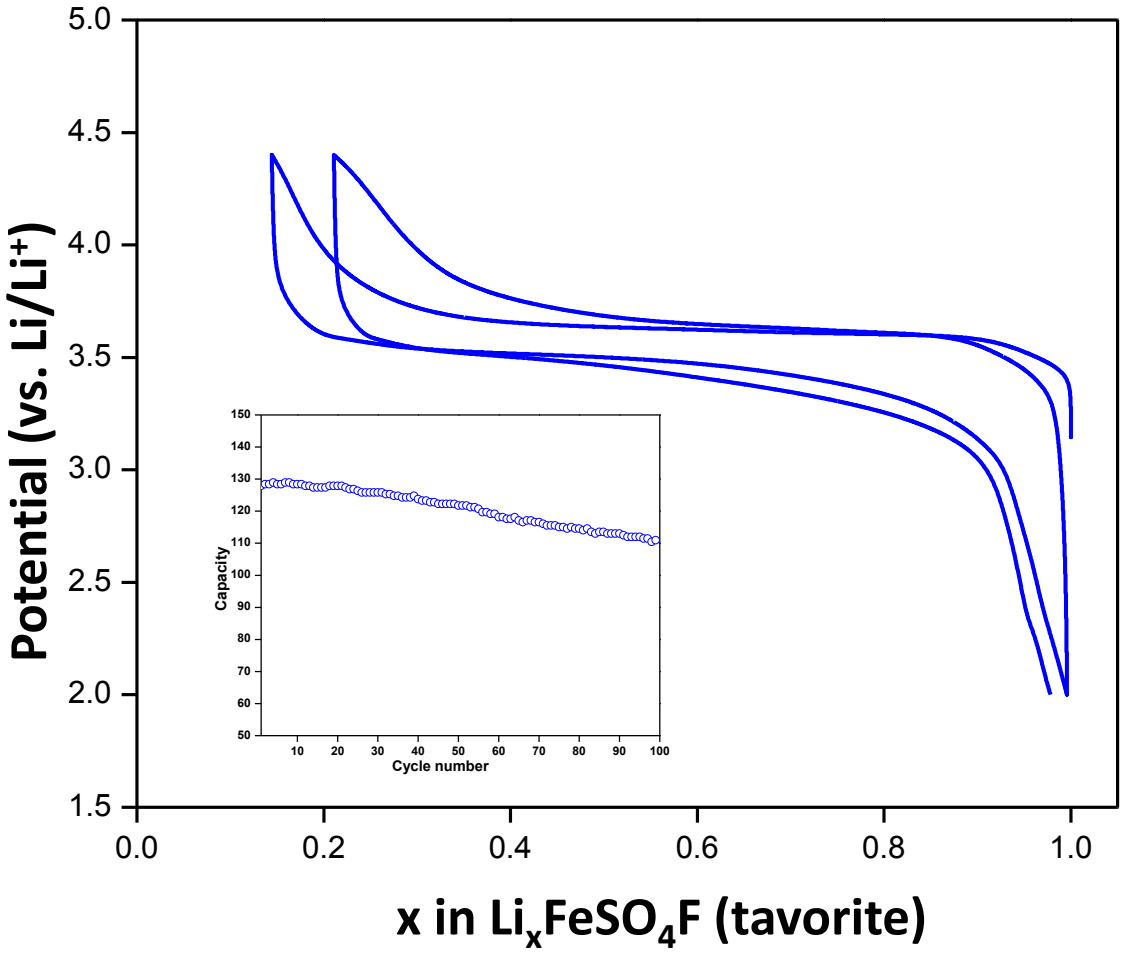

Figure 3.18 Electrochemical charge-discharge curve of tavorite $LiFeSO_4F$ (rate: C/10, active materials 80%, Super P : 20%). Inset shows the capacity retention after cycling.

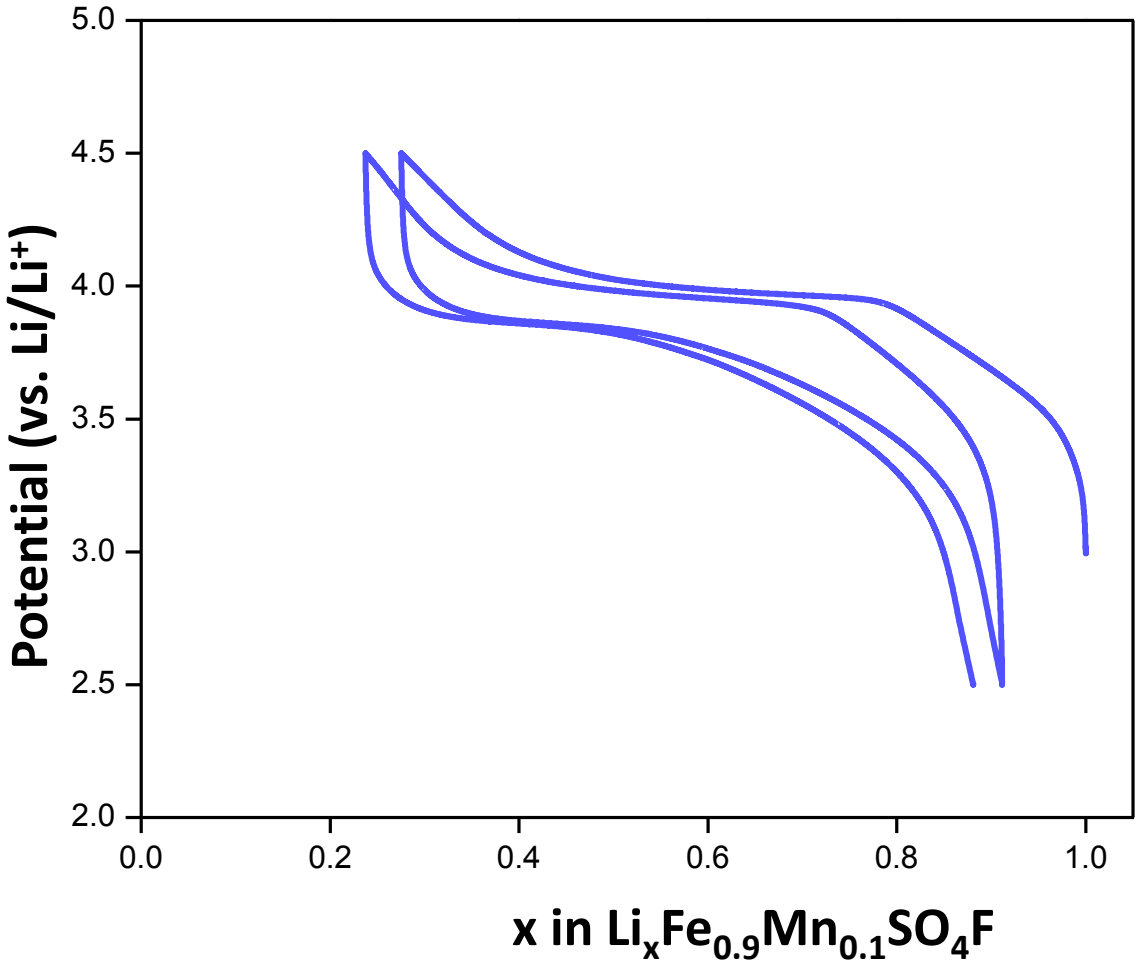

Figure 3.19 Electrochemical charge-discharge curve of triplite $LiFe_{0.9}Mn_{0.1}SO_4F$ (rate: C/10, active materials 70%, Super P :30%)

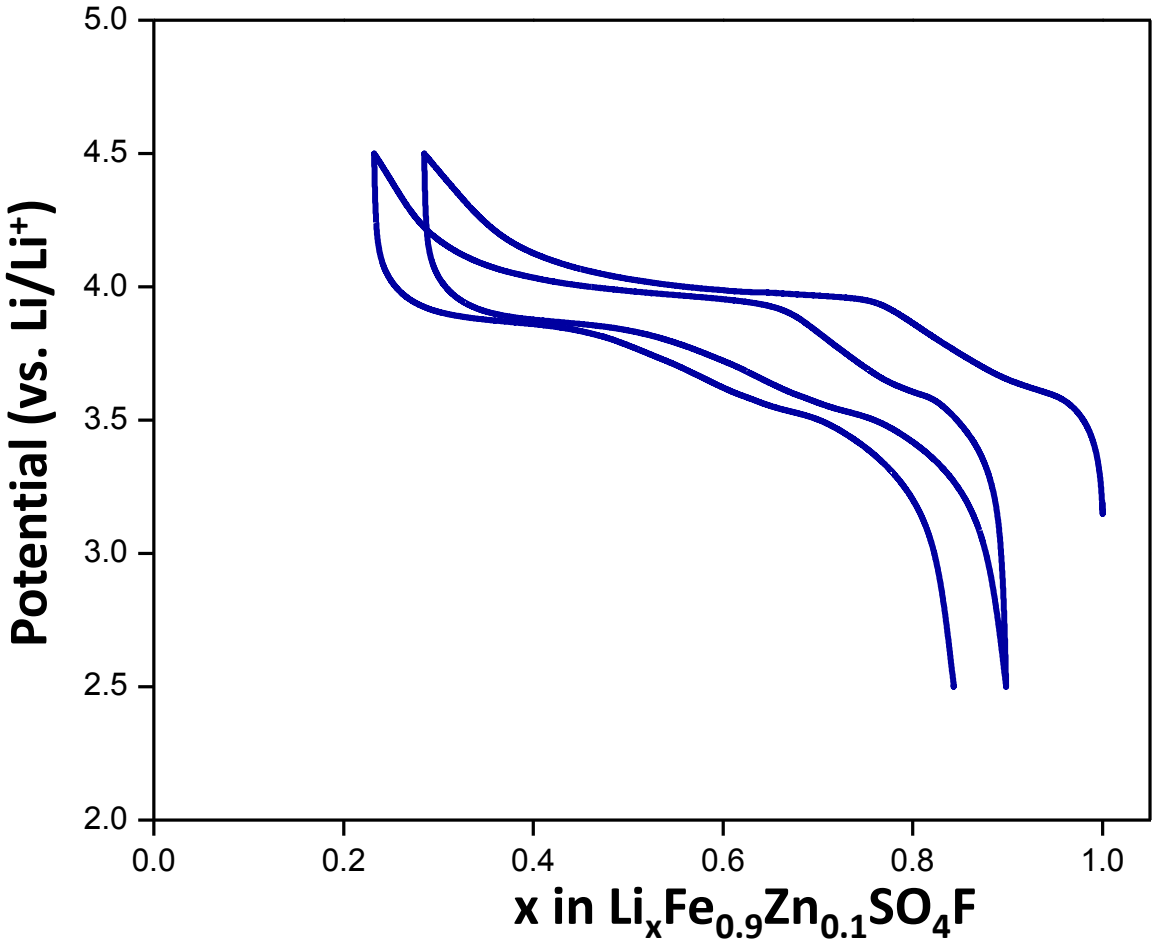

Figure 3.20 Electrochemical charge-discharge curve of triplite $LiFe_{0.9}Zn_{0.1}SO_4F$ (rate: C/20, active materials 70%, Super P :30%)

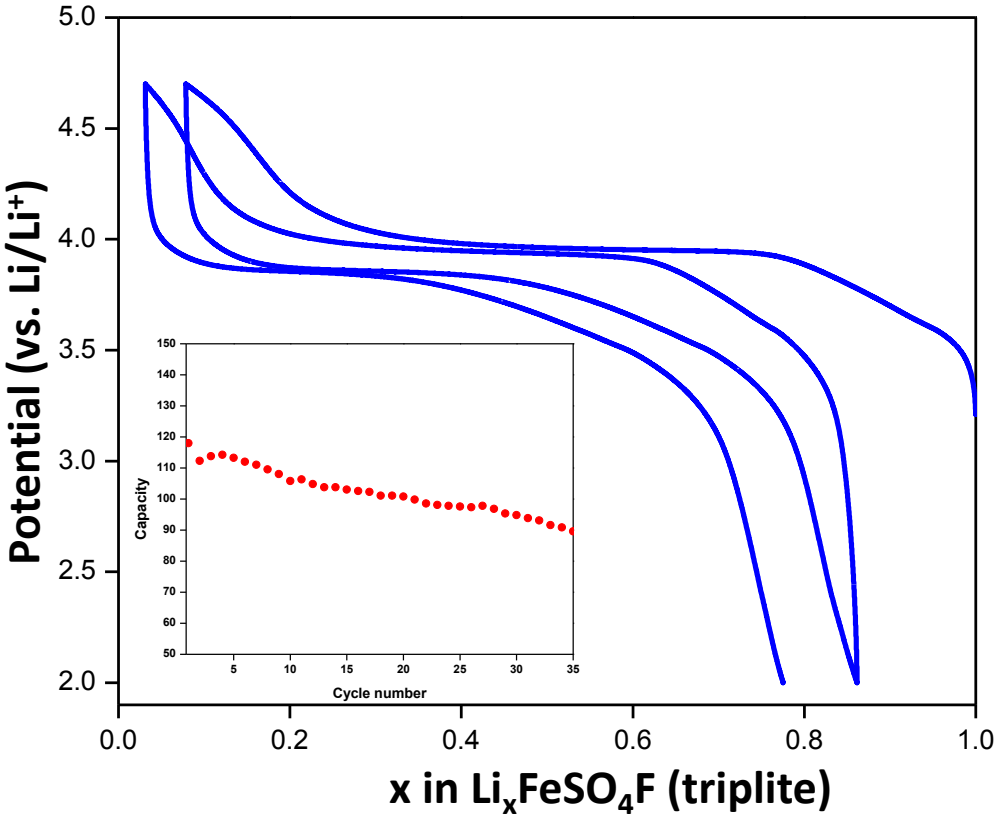

Figure 3.21 Electrochemical charge-discharge curve of triplite $LiFeSO_4F$ prepared *via* microwave assisted synthesis process (rate: C/20, active materials 80%, Super P :20%). Inset shows the capacity retention after cycling.

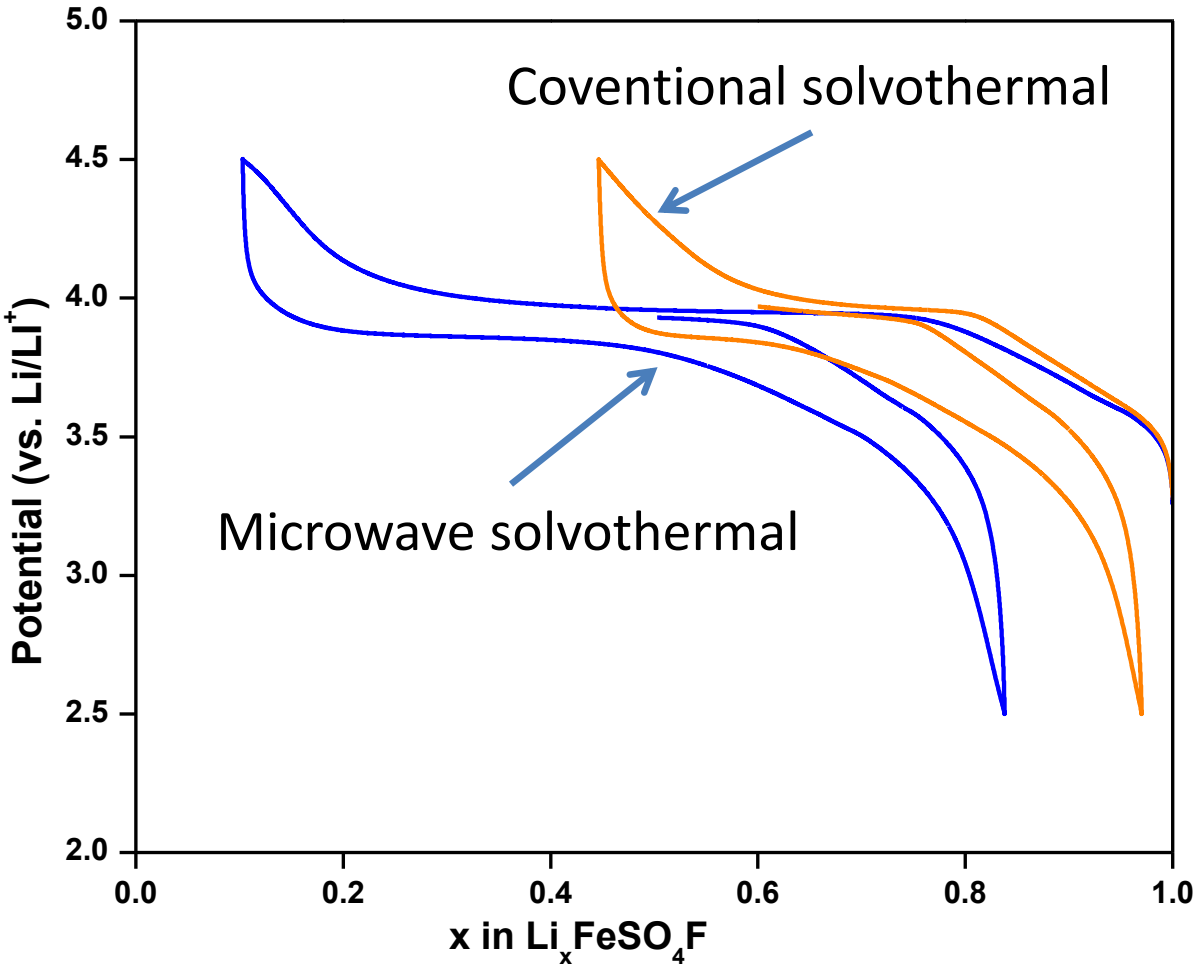

Figure 3.22 Comparison between electrochemical charge-discharge curve of triplite $LiFeSO_4F$ prepared by extended conventional solvothermal and microwave assisted process (rate: C/20, active materials 80%, Super P :20%)

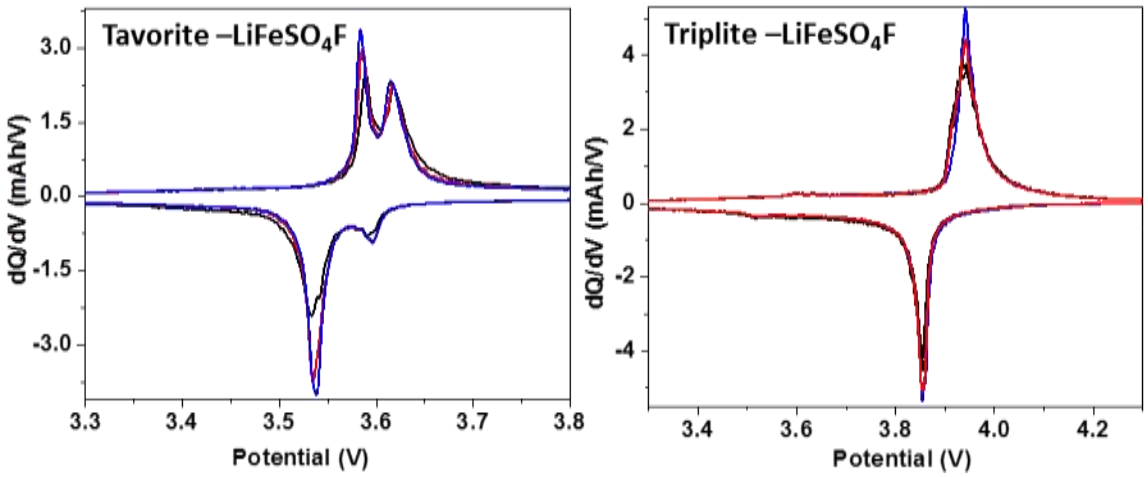

Figure 3.23 Differential capacities *vs.* voltage curves for tavorite and triplite $LiFeSO_4F$. Blue, red and black curves show 2^{nd} , 5^{th} and 10^{th} cycles respectively

3.3.7 Origin of the Voltage Increase

The difference in the intercalation voltage between tavorite and triplite type compound can be understood by considering the differences in framework connectivity in both the structures. In the triplite (unlike the tavorite) the coordination polyhedra of the metal cations share edges with each other. Such an arrangement leads to increased cation–cation repulsion. As a result, the octahedron increases in size to partially counter the decreased proximity between transition metals. In triplite type compound the average bond length around M1 is 2.124 Å while for M2, it is 2.153 Å. For tavorite $LiFeSO_4F$ (corner shared transition metal octahedra) these values are in the range 2.078–2.119 Å. The slightly longer bond lengths for the triplite are indicative of the decreased charge density on the metal site which is in agreement with the 300 mV increase in the redox voltage. A lower charge density is expected to lower the Fermi level and therefore increase the redox voltage.

3.3.8 Origin of the Phase Transition

The phase transition of the tavorite type to the triplite type $LiFeSO_4F$ is considered largely driven by the higher entropy of the disordered triplite phase. However, in the light of the unique phase transition displayed by the microwave prepared tavorite type $LiFeSO_4F$ (as described above), additional characterization of the sample was carried out to understand the reasons behind this phenomenon. **Figure 3.24** shows FTIR spectra collected for both the tavorite and the triplite type $LiFeSO_4F$ polymorphs synthesized using the microwave-assisted and conventional solvothermal methods. Peaks characteristic of the SO_4^{2-} group are present in the region of 1400-400 cm^{-1}, similar to previously reported fluorosulfate compounds.[199] Hydroxyl bands are also visible. The signatures of the OH^- groups associated with inorganic compounds normally appear[200] at 3700-3500 cm^{-1} while OH^- groups associated with the solvent TEG have been reported[201] at ~3400 cm^{-1}. The presence of broad peaks around 3400 cm^{-1} and a shoulder at ~3600 cm^{-1} in the microwave prepared tavorite type $LiFeSO_4F$ therefore indicates the presence of framework OH^- groups along with some glycol on the surface. On conversion to triplite, the framework OH^- disappears, although a trace of glycol remains. Presence of glycol peaks is not unusual even after heat treatment in solvothermally prepared samples[201] with glycol as the solvent. In contrast, lattice hydroxyl is not visible in the conventional solvothermal tavorite which shows only a surface glycol peak contribution at ~3400 cm^{-1}. In short, the microwave tavorite is characterized by a lattice hydroxyl contribution that disappears upon conversion to triplite type polymorph, whereas this feature is absent for the conventional solvothermal tavorite type polymorph of the compound. Another evidence that this is a surface initiated phase transformation, was obtained when microwave prepared tavorite $LiFeSO_4F$ was mixed with sucrose in 2:1 weight ratio and the mixture was heated at 350°C for 1 hour. There was no change

observed in the XRD pattern of the tavorite type $LiFeSO_4F$ and complete conversion to phase pure triplite type polymorph occurs only after 8 hrs. At this stage, it can be safely concluded that the sucrose-tavorite mixture, upon heat treatment, results in small tavorite particles coated with a carbonaceous layer which retards the dehydrogenation of OH^- groups present on the surface of the particles. Therefore, the phase transformation is delayed. A comparison of the TGA curves of both of tavorite and triplite compounds obtained by microwave assisted methods is shown in **Figure 3.25**. Slightly higher weight lost in 300-400°C in tavorite type compound is attributed to loss of OH^- groups. Both the compounds decompose after 400°C to produce a combination of Fe_2O_3, FeS_2, LiF and SO_2 among other products.

Based on the above results **Figure 3.26** presents a possible mechanism for rapid phase transformation from tavorite to triplite. Upon heating, condensation of the surface hydroxyl groups releases H_2O [$Fe\text{-}(OH^-)_2 \rightarrow H_2O + Fe(O^{2-},\square)$], generating oxygen vacancies. The reduced unit cell volume on the surface of the material generates a surface tension along the plane parallel to the surface. The net result of this would be a radial compressive stress generated in a spherical particle. This stress is released by transforming the underlying tavorite type material to the denser atomic packing provided by the triplite type structure that exhibits a ~2% lower unit cell volume per formula unit ($\Delta V/Z$). This provides the trigger for the phase transformation.

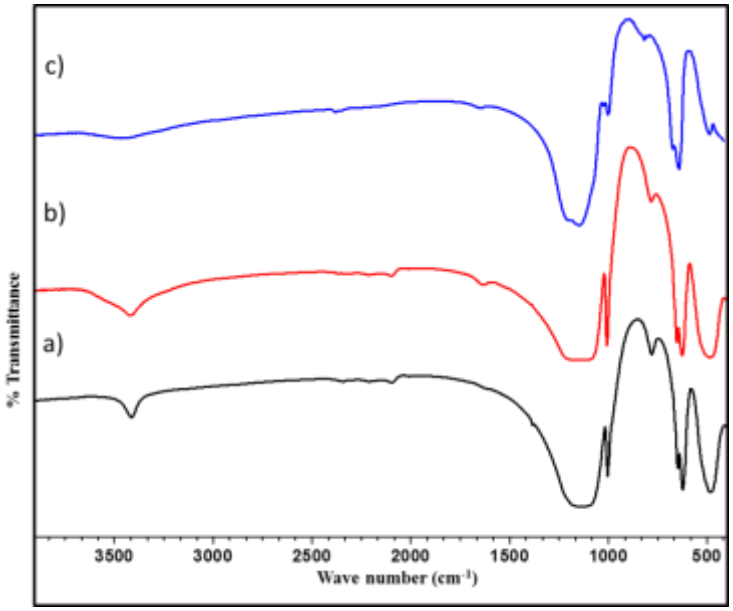

Figure 3.24 FT-IR spectra collected for a) tavorite type $LiFeSO_4F$ prepared by conventional solvothermal b) tavorite type $LiFeSO_4F$ prepared by microwave solvothermal and c) triplite type $LiFeSO_4F$ prepared by heating microwave tavorite sample.

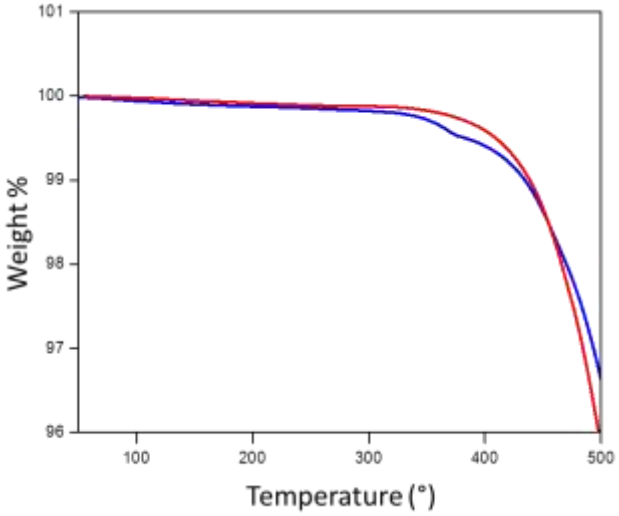

Figure 3.25 TGA curve for triplite (red) tavorite (blue) type $LiFeSO_4F$

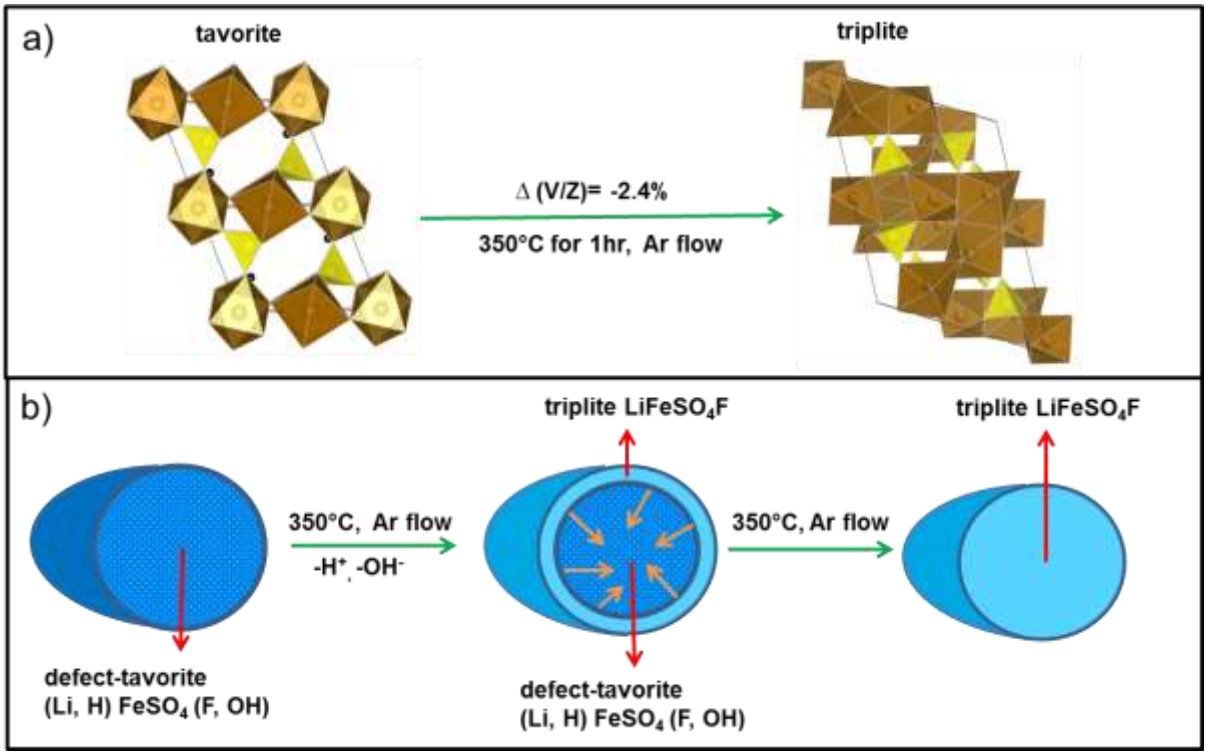

Figure 3.26 Comparison of unit cell volumes of tavorite and triplite; b) phase transition mechanism in MW-$LiFeSO_4F$

3.4 Conclusions

Fascinating and complex structural and electrochemical properties are exhibited amongst the polymorphs of the lithium metal fluorosulfate family. The solvothermal synthesis route provides the most powerful and simple ways to access these materials as phase-pure compounds. Lithium iron fluorosulfate first crystallizes in a cation-ordered tavorite type structure that completely converts to a cation-disordered triplite structure on prolonged heating under solvothermal conditions, a process driven by entropic factors. The combined XRD and neutron study of the triplite type compounds show a complete disorder of the Li over the two cation sites. No preferential segregation is observed on any one site.

Microwave-assisted solvothermal synthesis rapidly generates nanocrystalline $LiFeSO_4F$ tavorite with defects that induce significant microstrain. To date, this is unique to the microwave synthesis method which remains a largely unexplored technique capable of producing unique outcomes. Phase transformation to a more stable triplite framework is quickly triggered by heat, facilitated by the defects and the hydroxyl groups. This provides a quick and scalable route for the synthesis triplite type $LiFeSO_4F$. The electrochemical performance of triplite type $LiFeSO_4F$ is strongly dependent on the particle size whereas no such dependence is observed for the tavorite polymorph owing to its highly ordered structure that provides a clear pathway for Li-ion migration. In contrast, the inherently disordered nature of the triplite structure results in a tortuous high-activation pathway for Li-ion migration, rendering a fraction of Li ions in the core of the material inaccessible even at intermediate rates in micron-sized particles. The nanocrystallite dimensions afforded by the microwave route largely overcome this limitation.

The rapid 3D ion transport characteristics of the framework at the atomic level, and comparable specific energy density to that of $LiFePO_4$ owing to its higher voltage (543 $Wh\,kg^{-1}$ vs. 581 $Wh\,kg^{-1}$) also auger well for future importance of $LiFeSO_4F$ as a practical electrode material. The contrasting electrochemical performance of the two polymorphs presents an excellent opportunity to revisit some of the most debated issues in the field such as framework dependence of ion conduction and electrochemical voltage. More detailed studies of Li-ion conduction in these materials using simulation methods will be presented in the next chapter.

Chapter 4

Alkali-Ion Conduction in Tavorite, Layered and Olivine Type Structures

4.1 Introduction

In Li-ion battery, Li-ions shuttle back and forth between the negative and positive electrode through the middle layer of the electrolyte to counter the charge imbalance created by the flow of electrons in the outer circuit. Therefore, for a fast charge and discharge, ions must be able to quickly move inside the electrode's crystal structure as well as in the electrolyte. Since typically used liquid electrolytes are much better Li-ion conductors than solid electrodes, Li-ion diffusion coefficient in the later is a rate limiting step during charge and discharge of the battery. Similarly, Na-ion batteries (NIB), which operate on the same principle as Li-ion batteries must be able to quickly transport Na-ion from one end to the other for a good charge and discharge rate. According to the classical model of ion conduction, ions migrate in a crystal structure *via* hopping from one crystallographic site to another. In the process, they must pass through an energy barrier since crystallographic sites are energy minima in the energy landscape of the crystal. This energy barrier is known as activation energy for ion diffusion and depends strongly upon the structure and migrating ion type as shown later in this chapter.

Chemical defects are aberrations present in the regular structure of the material. The presence of point defects (*i.e.* vacancies and interstitials) up to a certain concentration is a thermodynamic necessity as they increase the entropy of the material. Concentration of defects in a material depends on the energetics of their formation which can often be controlled by the

choice of synthesis method. For example, theoretical and experimental evidence exists suggesting that the antisite defect concentration (formed by intersite ion exchange) can be tuned in $LiFePO_4$ by using either hydrothermal or solid state synthesis methods.[202,203] Defects can potentially change many properties of the materials including ionic and electronic conductivity. A higher concentration of antisite defects in olivine $LiFePO_4$ has been shown to considerably slow down Li-ion migration kinetics resulting in a poor electrochemical behavior.

Substantial effort has been expended in previous decades to prepare positive electrode materials for Na-ion batteries that can easily intercalate and transport Na-ions at suitable potentials. Recently P2-type $NaFe_{0.5}Mn_{0.5}O_2$ has been shown to be an excellent positive electrode material which can reversibly intercalate Na-ions in 2-4.5 V range with good rates of charge and discharge.[149] Many other oxides such as $NaCoO_2$,[143] $NaCrO_2$,[204] $NaVO_2$[205] and $NaNi_{0.5}Mn_{0.5}O_2$ show good initial reversible gravimetric capacities. However, in general, P2-type $NaMO_2$ compounds in which Na-ion are located in prismatic coordination display higher gravimetric capacity than O3-type in which Na-ions are located in octahedral geometry due to the slightly higher thermodynamic stability of the charged (desodiated) structure in the former case. Electrochemical de-intercalation of Na^+ cations from these oxides occurs *via* phase transitions between multiple intermediate phases, adding to the complexity of ion-migration during charge and discharge. Recently this topic has been examined in detail using computational studies that suggest that Na-ion migration energetics in oxides can be highly favourable.[211] Among polyanion materials $Na_{0.44}MnO_2$,[206,146,147,207] NASICON,[208] $NaVPO_4F$,[153] $NaFePO_4$,[209,158] and Na_2FePO_4F,[155,157,210] intercalate Na-ion in the range of 2.5-4 V thereby providing ideal behavior as positive electrode materials. These materials display a robust framework and better capacity retention than oxides at the expense of poorer conductivity (ionic

and electronic). Unlike the oxides, they usually display flat voltage behavior upon Na-(de)intercalation due to the structural energetics that drives two-phase behavior and formation of a phase boundary between Na-rich and Na-poor phases. While there have been many theoretical and experimental studies of Li-ion migration behavior in such systems only one recent paper has analyzed the energetics of Na-ion migration. [211]

Na_2FePO_4F was synthesized in 2005 by Ellis *et al*. The initial study demonstrated facile and reversible intercalation of Li^+ when the material was used as a positive electrode in a Li cell, *via* rapid exchange of Na^+ in one of the sites with Li^+. Na_2FePO_4F also intercalates Na^+-ion reversibly at an average of 3.0 V, as later demonstrated for both ionothermally[157] and solid state[210,212157] prepared material. Particularly good performance was obtained with as little as 1.3 wt% carbon coating using ascorbic acid as the carbon source, which also had the positive effect of reducing the particle size.[212] The material exhibits only a small volume difference (3.7%) when Na ions are de-intercalated from the 2-D layers of the structure resulting in a stable capacity retention at reasonable current densities (110 mAh/g at 0.1C).[210] Another equally important material olivine $NaFePO_4$ can be synthesized using earth abundant and relatively inexpensive materials. It de/-intercalates Na-ions at 3.2 V.[209,158] The mixed Fe-Mn system $NaFe_{0.5}Mn_{0.5}PO_4$ was also synthesized recently in olivine form and it gives a characteristically different electrochemical curve than isostructural $NaFePO_4$ when cycled in a Na-cell.[158] Conflicting reports have emerged regarding the electrochemical properties of olivine $NaFePO_4$. While the initial study by Moreau *et al*.[209] indicated that carbon coating of the parent material $LiFePO_4$ did not impact the electrochemical performance of the olivine $NaFePO_4$, recent investigations by Wang *et al*.[213] have demonstrated much superior electrochemistry (~100 mAh/g at 0.1C rate). However these

values are still inferior to those of the carbon coated lithium analogue. In contrast with $LiFePO_4$, deintercalation of Na from $NaFePO_4$ occurs *via* intermediate $Na_{0.7}FePO_4$.[209] First stage of Na deintercalation (from $NaFePO_4$) occurs at ~2.9 volt while the second stage occurs at ~3.1 volt (from $Na_{0.7}FePO_4$). However, only single voltage plateau during discharge of the material is observed. Such asymmetry of the charge-discharge has been recently studied using combination of TEM and XRD.[214] The study concludes that all the three phases ($NaFePO_4$ $Na_{0.7}FePO_4$ and $FePO_4$) are simultaneously present during the discharge owing to the large unit cell volume difference between completely charged ($FePO_4$) and other two compounds ($NaFePO_4$ and $Na_{0.7}FePO_4$). During charge (desodiation), small volume difference between $NaFePO_4$ and $Na_{0.7}FePO_4$ restricts the formation of $FePO_4$ until all of $NaFePO_4$ has first converted to $Na_{0.7}FePO_4$.

To fully understand the local structural and transport features influencing the electrochemical behavior of above mentioned materials, it is clear that fundamental knowledge of their underlying defect and transport properties is needed on the atomic scale. Atomistic modeling technique provides a powerful means of investigating these key solid-state issues, but has not been applied to Na-layered type fluorophosphates, (Li,Na) tavorite type fluorosulfates or Na-olivine type materials. This chapter describes energetics of defect formation, alkali ion migration and corresponding activation energy barriers for tavorite ($LiFeSO_4F$, $NaFeSO_4F$), layered (Na_2FePO_4F) and olivine ($NaFePO_4$) type materials.

4.2 Method

As described in **Chapter 2** atomistic scale simulations are based on the energy minimization of the structure by employing interatomic potential parameters.[176] The structure obtained from the X-ray refinement studies was used as input to the General Utility Lattice

Program (GULP) as describe in **Chapter 2**. Interactions between ions in the fluorosulfate, phosphate and fluorophosphate structures consist of a long-range Coulombic term and a short-range component representing electron-electron repulsion and van der Waals interactions. The short-range interactions were modeled using the two-body Buckingham potential (**Table 4.1 and Table 4.2**). An additional three-body term was used for the XO_4^{n-} (X =P, S) units to account for the angle dependent nature of O-X-O bonds, as previously used for other sulfates[215] and phosphates.[79] The well-known shell model[216] was employed to account for the polarizability effects of charged defects on the electronic charge clouds. The Fe-O and Li-O, P-O and O-P-O interatomic potentials were taken from a study on $LiFePO_4$.[79] The Na-O, S-O, O-F, Fe-F and A-F (A= Li, Na) interactions were obtained by refining parameters from previous studies on fluorides and oxyfluorides.[217] For the sulfate component, the interatomic potential model successfully formulated to simulate M_2SO_4 (M = Na, K, Rb and Cs) and XSO_4 (X = Sr, Ca, Ba)[215] was used. A Morse potential was used to describe intra-molecular bond-stretching interactions between S and O ions in the sulfate group.[215] The lattice relaxation about defects (such as Li vacancies) and migrating ions was calculated by an implementation of the Mott-Littleton scheme incorporated in the GULP code.[218] This method partitions the crystal lattice into two regions, where ions in the inner region immediately surrounding the defect (on the order of >700 ions) are relaxed explicitly.

The classic hopping model of ion diffusion was used to calculate the activation energy barrier for migration of the Li or Na –ion in the structure. To find the least energy hopping path, the energy of the structure was calculated for the intermediate ion-vacancy distribution during hopping. To accomplish this, ten points were chosen on the line joining closest Li or Na sites in the structure and energy of simultaneous creation of two vacancies (at either end of the hop) and

the migrating alkali ion interstitial at each of the ten points as their initial position were calculated separately. The position of the alkali ion was allowed to change during simulation and thus minimum energy path was mapped for alkali ion migration between any two sites.

Table 4.1 Short range potential parameters for tavorite type $LiFeSO_4F$ and $NaFeSO_4F$

(a) Buckingham potentials						
Pair	A (eV)	ρ (Å)	C ($eVÅ^6$)	Y(e)	K($eVÅ^{-2}$)	Cutoff (Å)
$Li^+ - O^{0.84-}$	4787.6	0.20	0.00	1.00	99999	20
$Na^+ - O^{0.84-}$	9150.6	0.22	0.00	1.00	99999	20
$Li^+ - F^-$	400.6	0.27	0.00	1.00	99999	20
$Na^+ - F^-$	4000.6	0.22	0.00	1.00	99999	20
$Fe^{2+} - O^{0.84-}$	7500.0	0.22	0.00	2.997	19.26	20
$Fe^{2+} - F^-$	5609.2	0.23	0.00	2.997	19.26	20
$F^- - F^-$	1153.0	0.14	0.00	-2.321	63.58	20
$O^{0.84-} - F^-$	200.0	0.30	8.99	-0.84	99999	20
$O^{0.84-} - O^{0.84-}$	10358	0.20	25.93	-0.84	99999	20

(b) Three body			
Bond	K	Θ_0(°)	Cutoffs R_{ij},R_{ik},R_{jk} (Å)
$O^{0.84-} - S^{1.36+} - O^{0.84}$	15.000	109.47	1.8,1.8,3.2

(c) Morse potential				
Bond	D	B	R_0	Cutoff (Å)
$O^{0.84-} - S^{1.36+} - O^{0.84}$	5.000	1.200	1.505	1.8

Table 4.2 Short-Range Potential Parameters for olivine $Na[Fe,Mn]PO_4$ and layered Na_2FePO_4F

(a) Buckingham potentials						
Pair	A (eV)	ρ(Å)	C(eV·Å^6)	Y	K(eV·Å$^-$	Cutoff
Na^+ - O^{2-}	560	0.32	0.00	1	99999.0	20
Na^+ - O^{2-}	1497.83	0.28748	0	1	99999.0	20
Na^+ - F^-	8000	0.20	0	1	99999.0	20
Fe^{2+} - O^{2-}	1105.25	0.31	0.00	2.99	19.26	20
Mn^{2+} - O^{2-}	1305.25	0.31	0.00	2.99	19.26	20
P^{5+} - O^{2-}	897.25	0.35	0.00	5	99999.0	20
O^{2-}- O^{2-}	22764.3	0.14	44.53	-2.96	65.00	20
O^{2-}—F^-	200	0.3	8.99955	-	-	200
F^- - F^-	1153	0.1365	0	-2.32	63.57	1153

(b) Three body			
Bond	k (eV·rad^{-2})	Θ_0 (°)	Cutoffs R_{ij},R_{ik},R_{jk}
O^{2-}-P^{5+}-O^{2-}	1.322	109.47	1.8,1.8,3.2

4.3 Results and Discussion

4.3.1 Crystal Structure and Potential

The structure of $LiFeSO_4F$ belongs to the tavorite family of mineral structures, crystallizing in the triclinic *P*-1 space group as described in **Chapter 3**. The structure encompasses chains of alternately oriented corner-shared FeO_4F_2 octahedra that run along the *c*-axis and share fluorine located on opposite vertices. Each of the four oxygen atoms in the polyhedron is also bonded to a sulfur atom, forming Fe-O-S-O-Fe chains that cross-link the structure. The separation between the FeO_4F_2 octahedral chains introduced by the corner-sharing SO_4 tetrahedra results in three primary open tunnels along the [100], [010], and [101] directions in the structure that house the Li ions (**Figure 4.1**). In $NaFeSO_4F$, the connectivity between atoms is essentially the same, as seen in the structure illustrated in **Figure 4.2** (and **Chapter 5**). However, the lattice adopts a higher symmetry space group ($P2_1/c$) compared to that of

$LiFeSO_4F$ and thus there are subtle differences. Most importantly, the corresponding crystallographic directions between the two structures are different. They can be correlated by noting that the tunnels along the [100] and [010] directions in the $LiFeSO_4F$ correspond to the [110] and [-110] directions in the $NaFeSO_4F$. The starting structural parameters of the current simulation study were the observed crystal structure, in which the $LiFeSO_4F$ structure has been refined experimentally with two half-occupied Li sites. This was modeled in a *P-1* supercell with alternate occupation of these two sites, where Li_A and Li_B represent the alternate full occupancy of the Li1 and Li2 sites respectively. The potential parameters used in this study were used to simulate optimized structures, with a direct comparison of the experimental and the calculated structures reported in **Table 4.3**, **Table 4.5** and **Table 4.6** . The calculated *a*, *b* and *c* unit cell parameters deviate from experiment by at most 0.07 Å, and in most cases much less.

In the olivine $NaMPO_4$ structure (space group: *Pnma*), MO_6 octahedra link to each other *via* corner sharing in the *ab* plane. Sandwiched between these planes are PO_4 tetrahedra which share corners and edges with the MO_6 octahedra. Such a framework provides open channels along *b*-axis in which Na ions are located (**Figure 4.5**). In the layered-Na_2FePO_4F structure, iron is located on two crystallographic sites (Fe1 and Fe2) and the coordination polyhedra around them are connected to form face shared bi-octahedron units (**Figure 4.7**). These units are connected in the *a*-direction to from Fe-F-Fe chain. The chains are connected to each other by PO_4 tetrahedra along the *c*-direction, forming a layer of $Fe_2O_6F_3$-PO_4 units in the *ac* plane. Na ions reside in these interlayer spaces. Calculated lattice parameters and comparison to the experimentally reported values for olivine $NaMPO_4$ and layered Na_2FePO_4F are shown in **Table 4.4** and **Table 4.7**. Lattice parameters (unit cell lengths and angles) for all four compounds could be simulated within a maximum difference of 0.09 Å from experimentally reported values. Bond

lengths were also very similar. The successful reproduction of the complex crystal structures provide additional support that the potential models can be used reliably in the defect and migration calculations.

Table 4.3 Calculated and experimental structural parameters for $AFeSO_4F$ (A=Li, Na)

Lattice Parameters	$LiFeSO_4F$			$NaFeSO_4F$		
	Calc.	Exp.	Δ	Calc.	Exp.	Δ
a (Å)	5.102	5.174	-0.072	6.648	6.673	-0.025
b (Å)	10.919	10.988	-0.068	8.676	8.699	-0.022
c (Å)	7.184	7.222	0.038	7.252	7.187	0.065
α (°)	105.878	106.522	-0.643	90.000	90.000	0.000
β (°)	107.210	106.485	0.724	111.839	113.524	-1.684
γ (°)	96.746	97.791	-1.044	90.00	90.00	0.00

Table 4.4 Calculated and experimental structural parameters for Na_2FePO_4F and $NaFePO_4$

Lattice parameters	*a* (Å)	*b* (Å)	*c* (Å)
$NaFePO_4$			
Expt.	10.410	6.228	4.952
Calculated	10.316	6.163	4.929
Δ	-0.094	-0.065	-0.022
$NaMnPO_4$			
Expt.	10.557	6.335	4.996
Calculated	10.666	6.302	4.960
Δ	0.109	-0.034	-0.035
$NaFe_{0.5}Mn_{0.5}PO_4$			
Expt.	10.493	6.296	4.980
Calculated	10.462	6.218	4.944
Δ	-0.032	-0.078	-0.037
Na_2FePO_4F			
Expt.	5.220	13.854	11.779
Calculated	5.231	13.847	11.744
Δ	-0.011	0.008	0.034

Table 4.5 Comparison of selected bond lengths of experimental and calculated tavorite $LiFeSO_4F$ structure

Atom 1	Atom 2	Count	Distances ([Å], (Experimental))	Distances ([Å], Calculated)
Fe(1)	F(1)	2x	2.02	2.03
	O(3)	2x	2.13	2.13
	O(4)	2x	2.15	2.14
Fe(2)	F(1)	2x	2.01	2.02
	O(1)	2x	2.14	2.12
	O(2)	2x	2.23	2.15
S(1)	O(1)	1x	1.47	1.45
	O(4)	1x	1.47	1.47
	O(2)	1x	1.48	1.45
	O(3)	1x	1.50	1.45
Li(1)	O(1)	1x	2.51	2.20
	O(3)	1x	1.84	2.05
	F(1)	1x	1.90	1.81
	O(4)	1x	2.03	2.08
	O(2)	1x	2.25	2.13
Li(2)	F(1)	1x	1.84	1.81
	O(2)	1x	1.95	2.13
	O(3)	1x	2.07	2.05
	O(1)	1x	2.25	2.20
	O(4)	1x	2.54	2.08

Table 4.6 Comparison of selected bond lengths of experimental and calculated tavorite $NaFeSO_4F$ structure

Atom 1	Atom 2	Count	Distances ([Å], (Experimental))	Distances ([Å], Calculated)
Na	F(1)	1x	2.17	2.02
	O(2)	1x	2.30	2.47
	O(3)	1x	2.39	2.50
	O(4)	1x	2.54	2.57
	O(1)	1x	2.48	2.55
Fe	F(1)	1x	1.92	1.97
	F(1)	1x	2.02	1.98
	O(4)	1x	2.13	2.14
	O(1)	1x	2.17	2.15
	O(3)	1x	2.25	2.15
	O(2)	1x	2.27	2.16
S	O(2)	1x	1.46	1.47
	O(1)	1x	1.50	1.47
	O(3)	1x	1.51	1.47
	O(4)	1x	1.53	1.47

Table 4.7 Comparison of selected bond lengths of experimental and calculated layered Na_2FePO_4F structure

Atom 1	Atom 2	Count	Distances ([Å], (Experimental))	Distances ([Å], Calculated)
Fe(1)	F(2)	1x	2.04	2.01
	O(1)	1x	2.10	2.07
	O(4)	1x	2.12	2.08
	F(1)	1x	2.14	2.10
	O(4)	1x	2.17	2.18
P(1)	O(2)	1x	1.51	1.51
	O(1)	1x	1.53	1.54
	O(4)	1x	1.55	1.56
	O(3)	1x	1.56	1.57
Na(1)	F(1)	1x	2.35	2.37
	O(2)	1x	2.36	2.38
	O(3)	1x	2.41	2.41
	O(1)	1x	2.42	2.46
	O(2)	1x	2.46	2.46
	F(2)	1x	2.52	2.59
Na(2)	O(2)	1x	2.29	2.28
	F(1)	1x	2.32	2.36
	O(3)	1x	2.38	2.38
	F(2)	1x	2.41	2.45
	O(4)	1x	2.41	2.47
	O(1)	1x	2.29	2.28

Table 4.8 Comparison of selected bond lengths of experimental and calculated olivine $NaFePO_4$ structure

Atom 1	Atom 2	Count	Distances ([Å], (Experimental))	Distances ([Å], Calculated)
Na(1)	O(1)	2x	2.29	2.30
	O(2)	2x	2.33	2.30
	O(3)	2x	2.41	2.45
Fe(1)	O(2)	1x	2.05	2.02
	O(3)	2x	2.13	2.11
	O(1)	1x	2.15	2.14
	O(3)	2x	2.32	2.26
P(1)	O(3)	2x	1.54	1.52
	O(2)	1x	1.55	1.56
	O(1)	1x	1.55	1.57

4.3.2 Intrinsic atomic defects

The isolated defect (vacancy and interstitial) energies were calculated for $LiFeSO_4F$, $NaFeSO_4F$, $NaMPO_4$ and Na_2FePO_4F which were then combined to determine the formation energy for Frenkel and Schottky-type intrinsic defects. The following equations represent the reactions involving these defects (using Kröger-Vink notation; A = Li or Na):

A Frenkel: $A_A^x \rightarrow V_A^{'} + A_i^{\bullet}$ (3)

M Frenkel $M_M \rightarrow M_i^{\bullet\bullet} + V_M^{//}$ (4)

F Frenkel $F_F^x \rightarrow V_F^{\bullet} + F_i^{'}$ (5)

AF Schottky-type: $A_A^x + F_F^x \rightarrow V_A^{'} + V_F^{\bullet} + AF$ (6)

FeF_2 Schottky-type: $Fe_{Fe}^x + F_F^x \rightarrow V_{Fe}^{''} + 2V_F^{\bullet} + FeF_2$ (7)

A/Fe "anti-site" pair defect which involves the interchange of an A^+ ion with an Fe^{2+}/Mn^{2+} ion, was also examined. This is worth investigating since Li/Fe "cation exchange" effects have been a significant topic of discussion for $LiFePO_4$.[79] This process can be described by the following equation:

Anti-site: $$A_A^x + M_M^x \rightarrow A_{Fe}^{'} + M_A^{\bullet} \quad (8)$$

Examination of the resulting defect energies in tavorite type structures, listed in **Table 4.9** reveal two main predictions. First, the formation of all Frenkel and Schottky defects is unfavorable in both of the tavorite type $AFeSO_4F$ (A= Li. Na) structures. Interestingly, the results suggest that fluoride vacancies and fluoride interstitials are unlikely to exist in the pure (undoped) materials. Second, the anti-site energies are also relatively high which indicates that there would be no significant concentration of Fe on A sites at operating temperatures in the tavorite-type fluorosulfates. These results suggest that "blocking" effects involving Fe on Li or Na sites are much less likely in the tavorite type $AFeSO_4F$ positive electrode materials than in olivine type $LiFePO_4$.[79]

The calculated defect energies for $NaMPO_4$ (M = Fe, Mn, $Fe_{0.5}Mn_{0.5}$) are shown in **Table 4.10**. A positive energy of formation indicates that all of the Frenkel and Schottky defects are unfavorable in olivine type materials. Therefore, their concentration in the bulk is not expected to be significant. This trend is similar to the energy of defect formation previously reported for the olivine type $LiFePO_4$ using atomistic simulation methods.[79] In contrast, antisite defects are found to be the most favorable (lower energy of formation than corresponding values in olivine type $LiFePO_4$) which indicates that these are most frequently occurring defects in the olivine type $NaMPO_4$. The lower energy of antisite defect formation is in agreement with the observation that upon heat treatment, olivine $NaFePO_4$ transforms to maricite[209] structure in which metal sites are

completely switched as compared to the olivine structure i.e. M1 site is occupied by the transition metal and M2 site is occupied by the Na. The different connectivity of the Fe and Na octahedra in maricite compared to olivine does not provide a facile Na-ion migration pathway (as confirmed by preliminary calculations that suggest the alkali diffusion barrier is very high)[211] and results in a structure that is not amenable to Na^+ (de)insertion. In its thermodynamically stable form, $NaMnPO_4$ adopts the maricite structure, although in another polymorph of $NaMnPO_4$, natrophilite, the M1 and M2 sites are both half occupied by Mn^{2+} (0.83 Å) and Na^+. As a result, the only method for preparing electrochemically active olivine $NaMPO_4$ relies on the topotactic conversion of olivine $LiMPO_4$ (for M= Fe) *via* a delithiation-sodiation process or a low temperature synthesis method involving a topotactic conversion of $NH_4Fe_xMn_{1-x}PO_4 \cdot H_2O$ in $NaFe_xMn_{1-x}PO_4$.[158] The fact that direct methods cannot be used to prepare crystalline olivine $NaFePO_4$ confirms the highly metastable nature of this phase and consequently its tendency for cation disorder. The topotactic synthesis method ensures that the obtained product forms with a minimum concentration of antisite defects. However, the extraction of Na during electrochemical charge may trigger the formation of antisite defects as has been observed for $Li_{0.90}Ni_{0.45}Ti_{0.5}5O_2$ obtained from $Na_{0.90}Ni_{0\cdot45}Ti_{0.55}O_2$.[219] The anti-site defects can block diffusion paths for alkali ion migration and force additional diffusion directions ultimately raising the energy barrier for Na/Li ion migration in the structure. This results in a poor electrochemical performance for 1-D ion conductors of the olivine type. Like olivine $NaFePO_4$, in the layered Na_2FePO_4F as well (**Table 4.10**) all the Frenkel and Schottky defects are unfavorable. The energy of formation of antisite defects is much lower. This will result in a small but significant percentage of the Fe on the Na sites and vice versa. However, this is not expected to impact the Na-ion migration in the material as discussed below.

Table 4.9 Energy of formation of intrinsic defects in $AFeSO_4F$ (A=Li, Na):

Disorder type	Energy (eV)	
	$LiFeSO_4F$	$NaFeSO_4F$
A Frenkel	3.79	2.99
Fe Frenkel	7.60	10.09
F Frenkel	4.84	3.10
AF Schottky-type	4.22	4.10
FeF_2 Schottky-type	8.38	8.23
A/M antisite	2.50	2.40

Table 4.10 Energy of formation of intrinsic defects in Na_2FePO_4F and $NaFePO_4$

Defects	$NaFePO_4$	$NaFe_{0.5}Mn_{0.5}PO_4$	$NaMnPO_4$	Na_2FePO_4F
Na-Frenkel	2.25	2.29	2.35	3.22
Fe- Frenkel	6.60	5.01	-	5.24
Mn- Frenkel	-	4.91	7.28	-
Na_2O Schottky	10.05	10.06	9.71	10.78
FeO Schottky	7.31	7.48	-	5.19
FeF_2 Schottky	-	-	-	4.31
MnO Schottky	-	9.79	9.38	-
Na/Fe Antisite pair (isolated)	0.86	0.86	-	1.00
Na/Mn Antisite pair (isolated)	-	1.02	1.06	-

4.3.3 Li-ion Migration in Tavorite-Type-$LiFeSO_4F$

In the $LiFeSO_4F$ unit cell, there are two Li sites occupy two diametrically disposed positions in the tunnels that run along either the [100] or [010] directions, as shown in **Figure 4**. From this, main migration paths between adjacent Li sites were identified. There are three possible Li-Li hop distances along [100] and three Li-Li hop distances along [010] as shown in **Figure 4.1a**. These hops (L1-L6) represent all the possible migration paths between adjacent Li sites.

The calculated activation energies for Li ion migration in $LiFeSO_4F$ are included in **Figure 4.1** (and listed in **Table 4.11**), revealing three main points. First, the lowest migration energies are 0.36 – 0.46 eV for hops involving paths L3 to L6. Such relatively low values suggest high Li mobility in the $LiFeSO_4F$ material, important for good electrochemical behavior. Second, the results indicate that the favorable Li migration paths are a combination of two diagonal hops. These diagonal or zig-zag hops form continuous pathways through the structure and allow long-range diffusion along the tunnels in the [100], [010] and [111] directions, with the lowest energy path along [111]. The 3D-view of the structure (**Figure 4.3**) reveals that four unique hops (L3-L6) are possible for each Li ion which leads to continuous interconnecting paths and effective 3D transport of Li ions. Note that L1 and L2 are hops between symmetry-equivalent sites (i.e., Li_A-Li_A), along the [100] and [010] directions respectively, and are found to have high and unfavorable activation energies (> 1.0 eV); this is probably due to the migrating Li ion coming into close proximity to the FeO_4F_2 octahedra. Finally, although direct comparison with Li-ion conductivity data is not straightforward, the calculated values of about 0.4 eV is consistent with experimental activation energies for Li diffusion in other related framework materials.[220]

Table 4.11 Calculated activation energies for most favorable paths of alkali ion migration in $LiFeSO_4F$

Net diffusion direction	Jumps involved	Activation energy (eV)
[100]	L3 + L4	0.46
[010]	L5 + L6	0.44
[001]	L3 + L6	0.46
[101]	L4 + L6	0.44
[011]	L3 + L5	0.46
[111]	L4 + L5	0.36

Depending upon synthesis conditions, experimental values of the activation energy for Li ion mobility in fluorosulfate tavorites measured by impedance spectroscopy are reported to be in the range 0.77-0.99 eV for $LiFeSO_4F$[183,221] and 0.94 eV for $LiMgSO_4F$.[182] An estimated diffusion coefficient using such values of the activation energy would be of the order of ~ 10^{-19} cm^2/s, implying extremely limited ion mobility. These values are in contrast to the excellent electrochemical and ion-conducting behavior exhibited by these two materials. $LiFeSO_4F$ is known to have low thermal stability, therefore, inability to hot press the material leads to a poor particle-particle contact. This may heavily impede ionic motion in the samples leading to high activation energy values obtained by impedance measurements. A minimum value of 0.3 eV for $LiFeSO_4F$ has been calculated along an unspecified direction using DFT methods.[222] The discrepancy between the calculated and experimentally measured activation energies have been rationalized[222] by including Li vacancy formation energy in stoichiometric $LiFeSO_4F$. However, this is unlikely as the thermodynamic minimum, guided by the entropy of the system always

exists at a certain non-zero point defect concentration. Thus such systems will always have a finite concentration of Li vacancies.

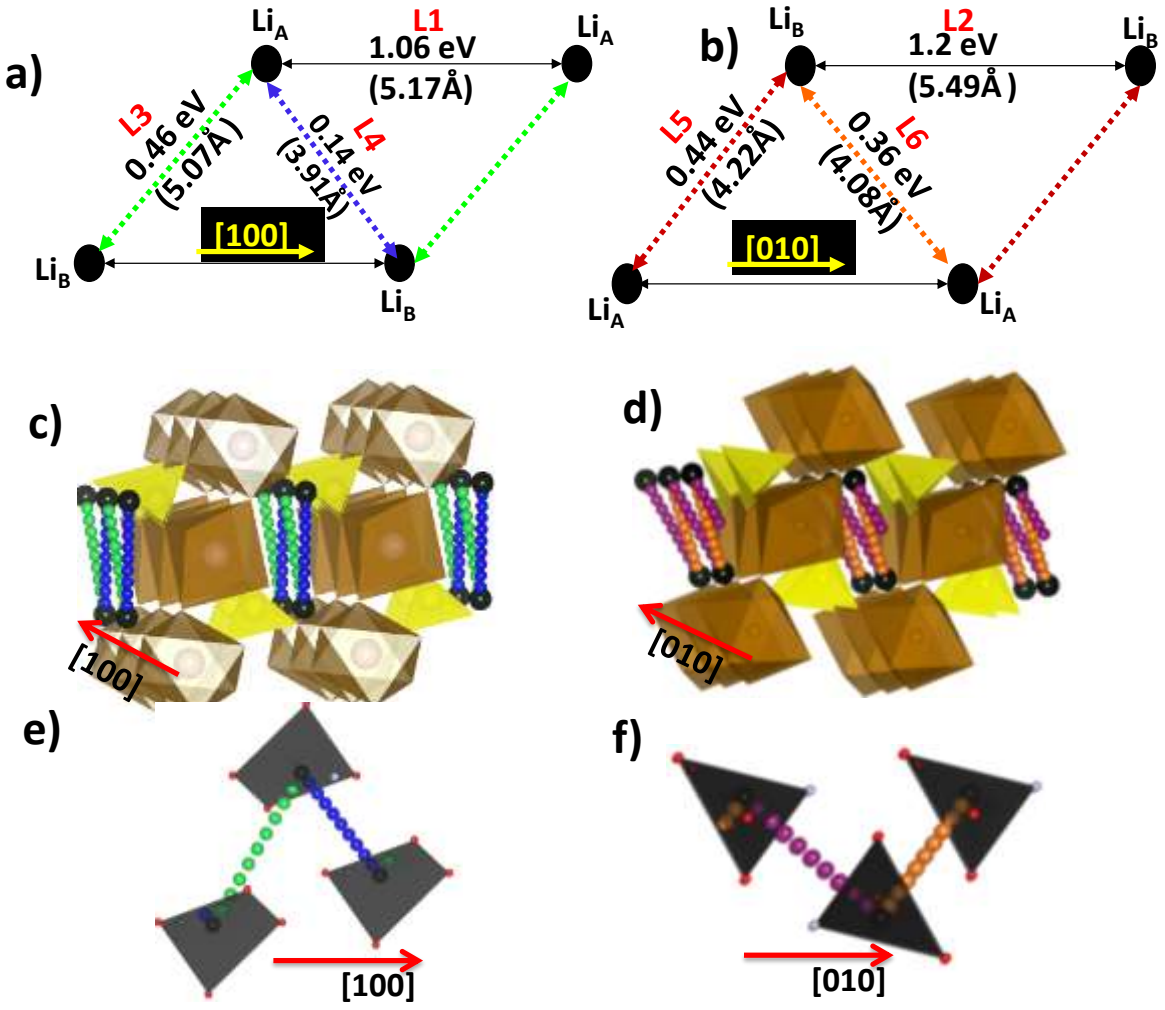

Figure 4.1 Schematic illustrating the various Li distances in tavorite $LiFeSO_4F$ along the primary tunnels a). [100] and b). [010]. The preferable Li ion hopping paths are shown where each color belongs to a unique hop with distinct activation energy. Corresponding long range transports within the lattice are shown in c) and d); e) and f) show coordination polyhedra around Li and hopping window for Li-ion migration. The same color code is followed as in (a).

4.3.4 Na- ion Migration in Tavorite-Type-$NaFeSO_4F$

$NaFeSO_4F$ crystallizes in a different space group ($P2_1/c$) to $LiFeSO_4F$ ($P\text{-}1$) with only one Na^+ ion site in the unit cell (**Figure 4.2,** see **Chapter 5** for structural details). Hence, the two intersecting tunnels, that are inequivalent in $LiFeSO_4F$ (along [100] and [010] directions) become equivalent in $NaFeSO_4F$ (i.e., along [110] and [-110] directions) and therefore only one schematic is shown in **Figure 4.2**. As with the $LiFeSO_4F$, the main migration paths in $NaFeSO_4F$ between adjacent Na sites were identified. The calculated activation energies for Na ion migration in $NaFeSO_4F$ are included in **Figure 4.2** (and listed in **Table 4.12**), indicating two key results. First, the lowest migration energy is 0.6 eV for hops involving paths N4 and N5, with other paths (N3-N5) involving short Na-Na distances (< 4.5Å) having activation energies of about 0.9 eV. Hence, the Na migration energy in $NaFeSO_4F$ is higher than that for Li migration in $LiFeSO_4F$, which suggests lower Na mobility. Second, the favorable Na migration paths are also a combination of diagonal or zig-zag hops forming continuous diffusion pathways through the structure. This large difference in magnitude indicates that Na^+ ion diffusion in $NaFeSO_4F$ is effectively one dimensional. The tunnel-structured material $Na_4TiP_2O_9$ has been reported to be a Na-ion conductor with activation energy as high as 1 eV, based on single crystal experiments.[223] The 3D-view of the structure (**Figure 4.4**) reveals that the lowest energy hop (0.6eV) leads to continuous interconnecting paths but only through the [101] tunnel and effective 1D Na^+ transport. As in the $LiFeSO_4F$, the highest energy migration path (1.9eV) involving N1 and N2 is close to the FeO_4F_2 octahedra, which is probably due to stronger steric interactions with the larger Na^+ ion. Overall, these simulations suggest that the ionic conductivity of $NaFeSO_4F$ should be lower than $LiFeSO_4F$. It has been pointed out earlier that split site occupancy of Li ions as opposed to fixed Na ion site may indicate higher Li ion mobility in the structure and this

is also confirmed by comparing bond sums (0.99 in $LiFeSO_4F$ vs. 1.16 in $NaFeSO_4F$). However, direct comparison with electrochemical behavior is not straightforward. Indeed, electrochemical (de)insertion in any electrode does not solely depend on the ionic conductivity. These may be nested in the two-phase driven (de)intercalation process (with a 14.5% volume difference in the end-member phases in case of $NaFeSO_4F$), which adds a substantial additional phase boundary migration energy term.

Table 4.12 Calculated activation energies for most favorable paths of alkali ion migration in $NaFeSO_4F$

Net diffusion direction	Jumps involved	Activation energy (eV)
[100]	N3 + N4 + N5	0.91
[010]	N3 + N4 or N3 + N5	0.91
[001]	N5	0.91
[110]	N3 + N4 + N5	0.91
[-110]	N3 + N4 + N5	0.91
[101]	N4 + N5	0.60

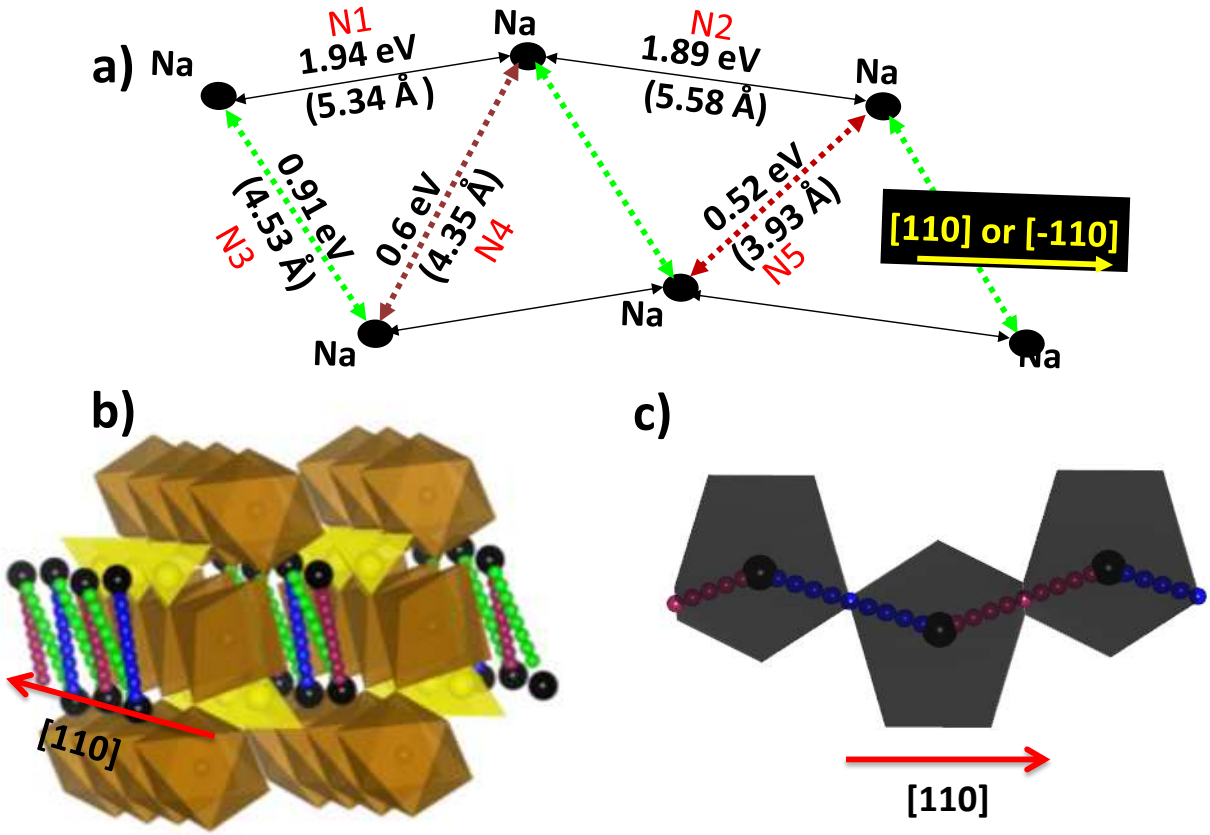

Figure 4.2 Schematic showing the various Na-Na distances in $NaFeSO_4F$ along the primary tunnels a). [110] or [-110]; The preferable Na ion hopping paths are depicted in color, where each color belongs to an unique hopping activation energy; b) Corresponding long range transport within the lattice; c) Coordination polyhedra around Na site and corresponding hopping window for Na-ion diffusion. Same color code is followed as in (a).

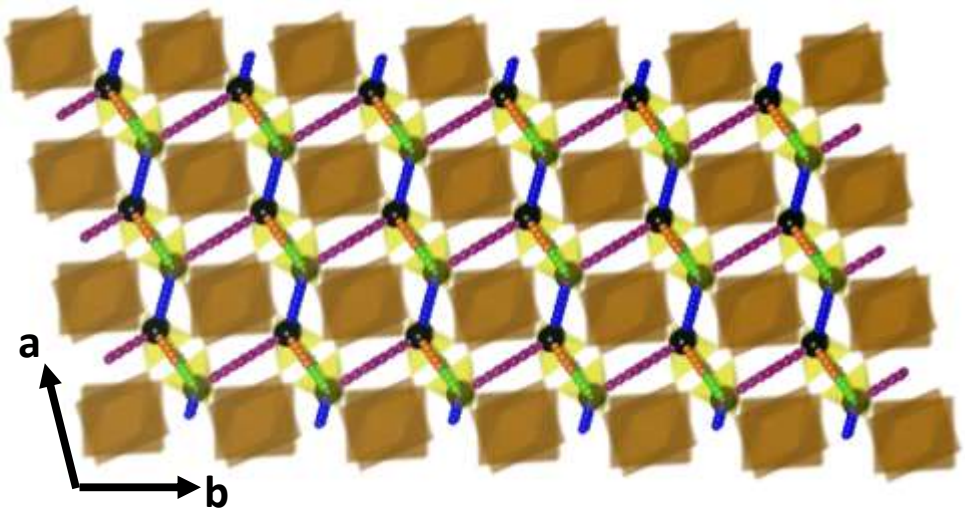

Figure 4.3 Full view of the structure and ion conduction pathways : 3D Li ion conduction in $LiFeSO_4F$.

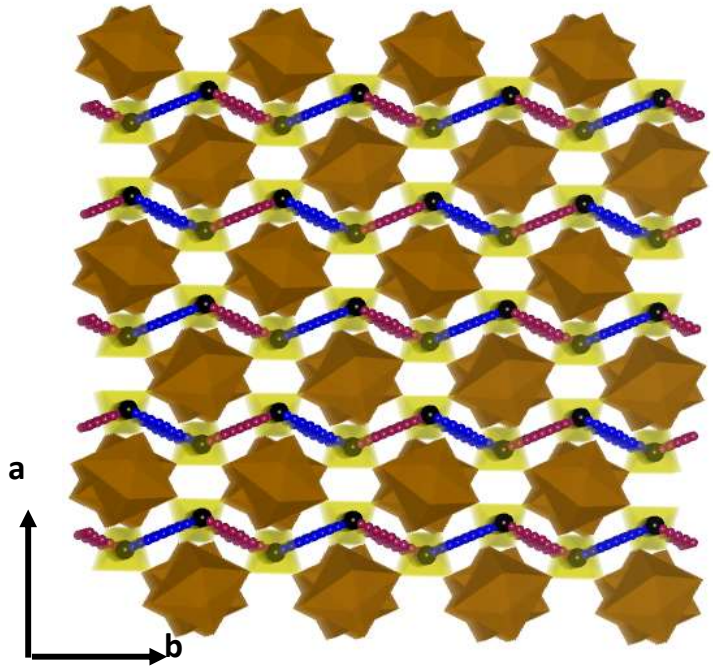

Figure 4.4 Full view of the structure and ion conduction pathways : 1D Na ion conduction in $NaFeSO_4F$

4.3.5 Na-ion Migration in Olivine $NaMPO_4$ (M=Fe, Mn, $Fe_{0.5}Mn_{0.5}$)

As described previously, the olivine structure is formed by edge and corner sharing octahedra and tetrahedra in orthorhombic space group *Pnma* (no. 62). Such arrangement of cations in the structure provide tunnel like features along *b* axis in which alkali ion (Li or Na) is located. To study the Na ion migration in olivine $NaMPO_4$ the pathways similar to already identified[79] for the most facile migration of Li in olivine $LiFePO_4$ were chosen for the investigation. It is expected that being the same crystal structure; least-hindered paths for alkali ion migration will be similar in both the compounds. These paths are: 1) along [010], 2) along [001], and 3) along [101]. Path along the *b*-axis [010] of the structure provides facile channels for Na ion migration. Along path "[001]", Na-atoms are placed at relatively far distances from each other and coordination polyhedra surrounding Fe and P provide a narrow window for ion migration. Path along [101] bisects *a* and *c*-axes and passes through a narrow window formed by MO_6 and PO_4 polyhedra. **Figure 4.5** presents the hopping activation energy values. Activation energy along [001] and [101] are relatively much higher in energy and therefore these are unfavorable for Na ion migration. This is similar to what was reported for Li ion migration in olivine $LiFePO_4$. The activation energy along [010] is lowest and it is even lower than the activation energy calculated for Li ion migration along the same path in the corresponding Li-olivine compound. **Figure 4.6** shows minimum energy migration path way for Na ions. For half substituted $NaFe_{0.5}Mn_{0.5}PO_4$, migration energy barriers are slightly increased (**Table 4.11**). However they still remain much smaller than their Li analogues ($LiFe_{0.5}Mn_{0.5}PO_4$). These trends continue for $NaMnPO_4$. The activation energy barrier for Na ion migration in this compound along *b*-axis is highest among the Na-olivines but lower than its Li-analogue $LiMnPO_4$. It is noteworthy that along [101] axis, activation energy barriers actually decrease upon substitution

of Fe by Mn in the composition (unlike their Li-analogues) but they still remain much higher than along the *b*-axis.

Higher mobility of Na in $NaFePO_4$ in comparison to Li in isostructural $LiFePO_4$ can be attributed to much longer average Na-O bond lengths (2.34 Å) than Li-O (1.96 Å). As a result, tunnels along b-axis are wider in Na-compounds (**Figure 4.5**) but naturally the size of the Na^+ cation is also larger than that of Li^+. **Figure 4.5c** shows two edge shared NaO_6 polyhedra both of which are slightly tilted towards each other thereby opening the faces below shared edge considerably. Such distortion clearly adds to the migration space for the curved path by providing larger opening for Na-hopping from one site to another. In addition, it is known that polarizability effects are important in which there are differences between the transport behavior of highly polarizing cations such as Li^+ and that of less polarizing cations such as Na^+.

4.3.6 Na-ion Migration in Layered Na_2FePO_4F

Layered Na_2FePO_4F unit cell consists of 6 unique Na-Na distances (numbered N1 to N6). Possible hopping directions for Na-ion migration are shown in **Figure 4.7** (cutoff length = 4 Å)**.** As shown, the smallest repeating unit of the sodium consists of 8 atoms. Calculations were restricted to all possible inter-atomic hopping of Na ions/vacancies among these atoms of which 4 are on Na1 site and the other four are on Na2 site. **Figure 4.7c** and **d** show examples of hopping window available for migration of Na along *a* and *c*-axes. Na –polyhedra connected by hops N2, N5 and N6 share edge with each other and polyhedra connected by hop N3 share faces while those connected by N4 share edges. **Figure 4.8** shows the least activation energy migration path for the Na ion and activation energy barrier (in eV) for Na_2FePO_4F. Ion migration in the *c*-direction occurs through N4-N3-N6 (0.3 eV) hop sequences, and along the *a*-direction occurs through a N2-N3-N5-N6 pathway (0.44 eV). These results show that there should be high Na^+

mobility within the *a*-axis and *c*-axis channels, and 2D Na migration in the *ac* plane. This behaviour contrasts with that of $NaFePO_4$, which only allows Na^+ migration along 1D channels parallel to the *b* axis. Most importantly, ion blocking by anti-site defects is much less likely to make a significant difference to Na–ion migration in Na_2FePO_4F than it does in olivine materials exhibiting 1D diffusion. It is interesting that the calculated energy barriers in Na_2FePO_4F are almost the same as in olivine $NaMPO_4$ (~ 0.3 eV), but much lower than the values found for tavorite-type $NaFeSO_4F$ (> 0.6 eV) using similar simulation methods.

Table 4.13 Calculated activation energies (in eV) for most favorable paths of alkali ion migration in Na-olivines

Direction	E_a , $NaFePO_4$	E_a , $NaFe_{0.5}Mn_{0.5}PO_4$	E_a , $NaMnPO_4$
[010]	0.32	0.36	0.46
[001]	2.73	2.90	3.10
[101]	3.03	1.50	1.51

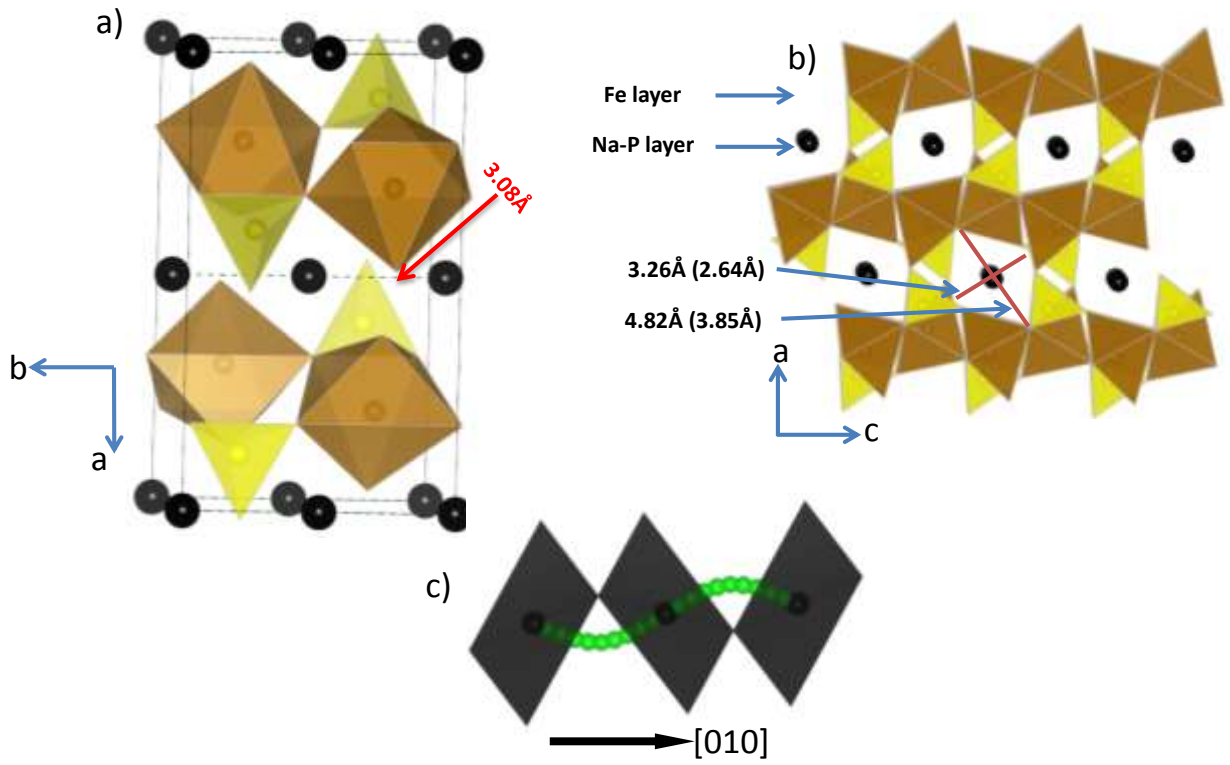

Figure 4.5 a) Unit cell of olivine type $NaFePO_4$ (brown polyhedra: FeO_6 and yellow polyhedra: PO_4, Black atoms represent Na) and Na-Na distance along *b*-axis b) tunnel dimensions for olivine $NaFePO_4$ are (numbers in brackets show these lengths for isostructural $LiFePO_4$). c) coordination polyhedra (dark grey) around Na-site and examples of hopping window for long range Na migration along b-axis in olivine $NaMPO_4$.

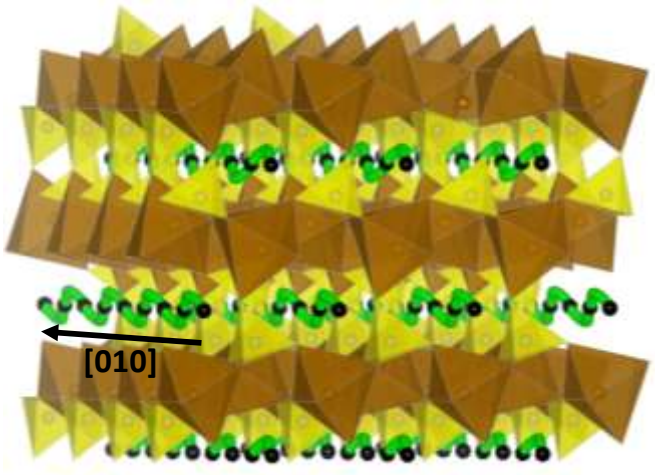

Figure 4.6 Na ion migration path along *b*-axis in olivine type $NaMPO_4$. Black atoms represent Na in the olivine structures and most facile pathway for Na-ion hopping is represented by green colored atoms. MO_6 and PO_4 polyhedra are represented in brown and yellow color respectively.

Table 4.14 Calculated activation energies (in eV) for most favorable paths of alkali ion migration in olivine Na_2FePO_4F.

Direction	Jumps involved	E_a
[100]	N3+N5	0.29
[001]	Various combinations of N2, N3, N4 and N5	0.44
[010]	-	>2

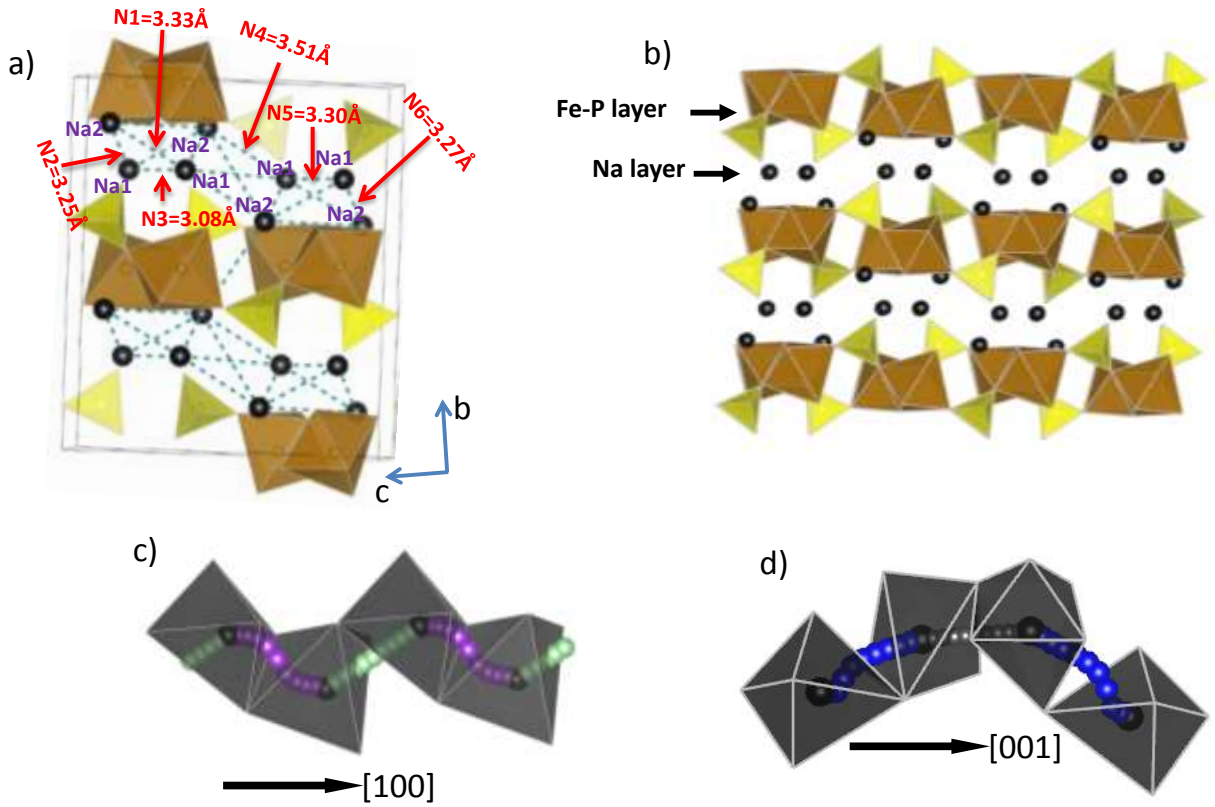

Figure 4.7 a) Unit cell of layered Na_2FePO_4F (brown polyhedron: FeO_6 and yellow polyhedron: PO_4, Black atoms represent Na) and Na-Na distance (cutoff distance: 4Å) b) Fe and Na layers in layered Na_2FePO_4F. Coordination polyhedron around Na-site in Na_2FePO_4F and hopping windows for long range Na migration path c) along *a*-axis; and d) along *c*-axis.

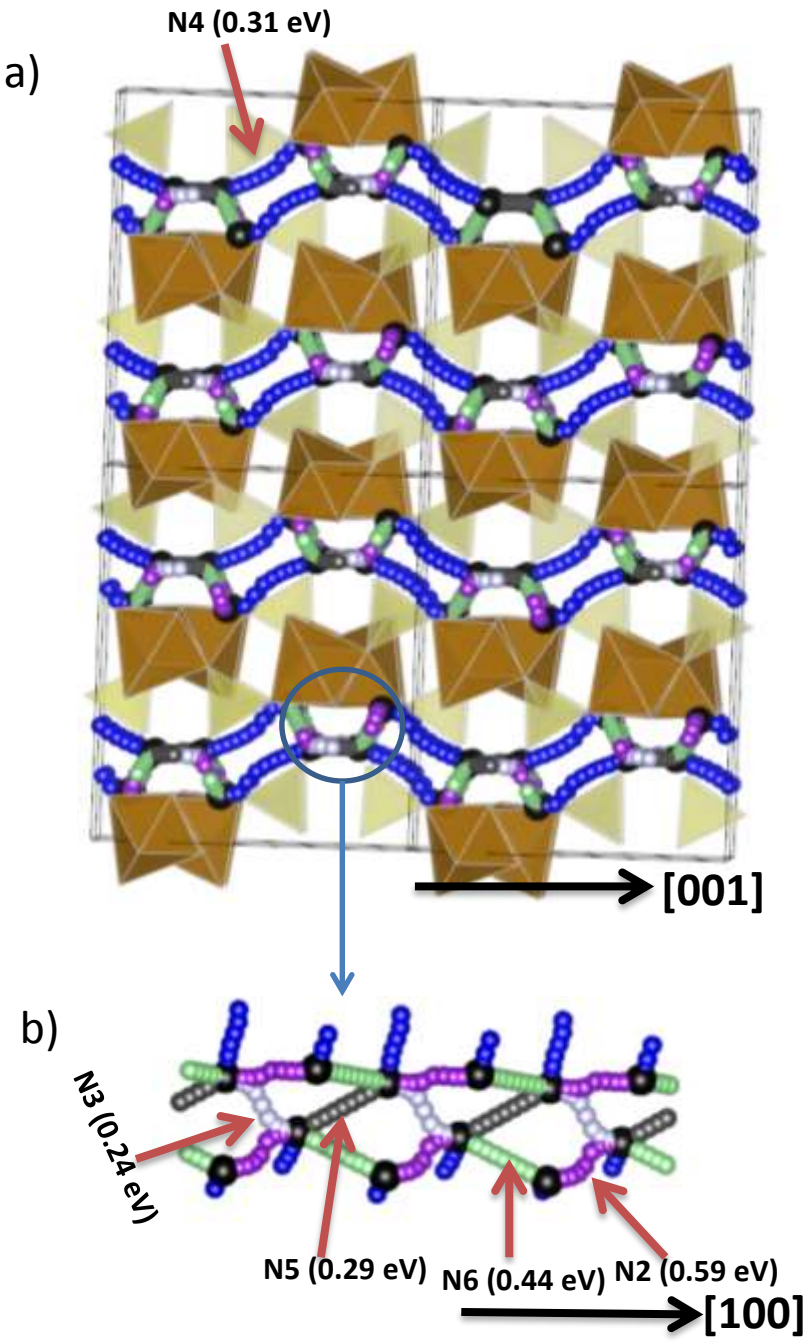

Figure 4.8 Na-ion migration path along *a* and *c*-axes in Na_2FePO_4F, octahedra FeO_4F_2 and tetrahedra PO_4 are represented by brown and yellow color respectively. a) along *c*-axis; long range migration path is formed by combination N4-N3-N6. b) along *a*-axis Na-ions migrate by a combination of N3-N5 hops.

4.3.7 Estimation of Diffusion Coefficient

The diffusion coefficient of any diffusion hop according to the dilute diffusion theory can be estimated using:[224] $D = g\Gamma a^2$ where D is the chemical diffusion coefficient, g is the geometric factor, "a" the hop distance and Γ the hopping rate defined according to transition state theory:[225] $\Gamma = \nu^* \exp^{(-E_a/KT)}$ where ν is the attempt frequency and E_a is the migration activation energy. Thus, the activation energy gives a direct estimate for the diffusion coefficient over a specific hop distance. For calculations in the current thesis, g is taken as 1 (spherical particle) and ν as 10^{13} s^{-1} which is typically used for framework materials.[225]

Dilute diffusion theory can be assumed to be reasonably valid for fluorosulfate, fluorophosphates and phosphate materials since (de)lithiation/sodiation in all of these material occurs *via* a two phase process over most of the compositional range. In this case, the new phase formed upon (de)lithiation remains nearly stoichiometric in nature, thus giving a very dilute, and therefore non-interacting, concentration of the charge carrying defects (Li^+, Na^+ ions or vacancies). Along the most facile ion transport path in $LiFeSO_4F$, diffusion coefficients for Li are estimated to be in the range of 10^{-8} -10^{-10} cm^2/s and for Na ion diffusion in $NaFeSO_4F$ that value is $7.14*10^{-13}$ cm^2/s. For olivine $NaFePO_4$ Na-ion diffusion coefficient along the tunnel (*b*-axis) was estimated to be ~ $5*10^{-8}$ cm^2/s and in Na_2FePO_4F, these values are ~ $7.5*10^{-8}$ and ~ $4.3*10^{-7}$ cm^2/s along *c* and *a* directions respectively. Using electrochemical methods, the diffusion coefficient of Li in nearly stoichiometric $LiFeSO_4F$ has been determined to be of the order of 10^{-12} cm^2/s.[226]

4.3.8 Electrochemical Behavior *vs.* Ionic Conduction

Activation energy barriers in Na_2FePO_4F are similar to olivine type $NaMPO_4$ materials and much lower than the values calculated for tavorite type $NaFeSO_4F$. Na-de-/intercalation from

Na_2FePO_4F has been observed to be much more facile than olivine $NaFePO_4$ and tavorite type $NaFeSO_4F$. This can be explained partially by invoking phase separation observed between charged and discharged phases during cycling. All of these compounds form a phase boundary between oxidized and reduced phases during charge/discharge which imposes an additional activation energy barrier that corresponds to the movement of the phase front in the material. Electrochemical performance is controlled by the amount of strain generated in this phase boundary, as well as by the activation energy barrier (E_a) for ion transport. Strain generated in the phase boundary is proportional to the difference in the unit cell volume (ΔV) of the oxidized and reduced phases which is ~17% for $NaFePO_4$, ~14% for $NaFeSO_4F$ but only ~3.7% for Na_2FePO_4F. In the case of olivine type $NaFePO_4$, it has been recently pointed out that the stress generated by formation of the phase boundary is the root cause for different electrochemical profiles during charge and discharge.[214] For mixed transition metal phosphate $NaFe_{0.5}Mn_{0.5}PO_4$, it has been reported that no phase boundary is formed upon Na de/-intercalation.[158] However, a very large strain in the material can still be expected during the charge-discharge process as unit cell volume difference between fully oxidized and fully reduced compositions is 21%. A large volume change between the end members also induces very significant polarization during charge and discharge as seen for olivine $NaMPO_4$. In contrast, polarization is almost absent in the case of carbon coated layered Na_2FePO_4F.[210] This may explain the poor electrochemical performance of $NaFeSO_4F$ (E_a=0.60-0.91 eV, ΔV=14.3%) and $NaFePO_4$ (E_a = 0.32 eV, ΔV=15%) as compared to Na_2FePO_4F (E_a= 0.30-0.44eV eV, ΔV=3.7%). In the case of Li-intercalation electrodes the volume difference for $LiFeSO_4F$ is ~10% as compared to ~6.7% of $LiFePO_4$. Better electrochemical performance of $LiFeSO_4F$ indicates that in this case strain

generated by ~3% larger unit cell volume change at the phase boundary is easily overcome by very high 3-D diffusion coefficient of Li in the tavorite structure of $LiFeSO_4F$.

4.4 Conclusions

The atomistic scale simulations show good reproduction of the observed structure of all the tavorite ($LiFeSO_4F$ and $NaFeSO_4F$), olivine ($NaMPO_4$, M= Fe, Mn, $Fe_{0.5}Mn_{0.5}$) and layered (Na_2FePO_4F) materials. Formation of Frenkel and Schottky defects was found to be unfavorable in all cases. The Li/Fe and Na/Fe anti-site energies in tavorite type materials suggest that there would be no significant intrinsic concentration of Fe on Li or Na sites at operating temperatures in these fluorosulfates. Antisite defect formation energy in olivine $NaMPO_4$ is much smaller than $LiFePO_4$ suggesting a higher degree of Na on Fe sites in accordance with the known metastability of the ordered $NaMPO_4$ phases.

Investigation of the transport paths in $LiFeSO_4F$ indicates relatively low migration energies (~0.4eV), suggesting high Li mobility, which is important for good rate capability and capacity retention. The Li migration paths are a combination of diagonal jumps that form continuous diffusion pathways in the open tavorite structure. Li^+ transport is found to be effectively 3D in $LiFeSO_4F$ with diffusion along tunnels in the [100], [010] and [111] directions, with the lowest energy path along [111]. The Na ion transport in the monoclinic $NaFeSO_4F$ is also mediated by a combination of zig-zag jumps, but with higher activation energies (~0.9eV) than that for Li migration in $LiFeSO_4F$. The estimated diffusion coefficient for the most favorable migration path through the [101] tunnel is at least six orders of magnitude higher than in any other direction, suggesting that $NaFeSO_4F$ is effectively a 1D Na-ion conductor. Activation energy barrier for Li-ion transport measured using impedance spectroscopy are much higher than reported here. This discrepancy is mainly attributed to inability of obtaining dense pellets of tavorite $LiFeSO_4F$,

required for an accurate measurement of impedance, which mainly stems from the fact that the material can not be sintered above 400°C.

Activation energy barrier for the Na-ion conduction in phosphate olivine framework is much lower than for the Li-ion in similar framework. For layered Na_2FePO_4F, Na-ion conduction is largely 2-D in *ac* plane with diffusion coefficient being slightly lower along a-direction. Smaller activation energy barriers in the layered Na_2FePO_4F indicate that this compound as good ionic conductor as olivine type $NaFePO_4$.

The relationship between ionic transport and electrochemical properties among these materials highlights the crucial importance of the volume expansion-induced strain on de(intercalation), which is more substantial for the larger Na^+ (*vs* Li^+) ion. This has also been highlighted recently by others.[213] The strain contributes significantly to the overall energy for redox phase transformation, and hence materials with a high volume difference between the end member phases will invariably lead to poor rate capability and also faster capacity fade owing to electrochemical "grinding" which induces amorphization of the active material during charge and discharge. Where this is coupled with high activation energy for Na-ion transport (e.g. ≥ 0.8 eV) extremely poor electrochemical properties can be predicted, an example being $NaFeSO_4F$ which exhibits almost zero intercalation capacity despite having an open tavorite-like framework that is favorable for cation migration. High volume expansion combined with good ion transport gives better, but still poor properties for 1D conductors such as $NaFePO_4$, where antisite defects present additional barriers to Na^+ diffusion. However, very promising electrochemical properties can be anticipated for Na^+ ion materials with low volume expansion on redox - and where good electrical conduction is supported - since activation energy migration barriers can be low, as in the case of Na_2FePO_4F. Although the interplay of all the above factors is clearly complex and

still under investigation, these findings provide guidelines for the future design and synthesis of high rate positive (and negative) electrodes for intercalation batteries. .

Chapter 5

Synthesis and Crystal Structures of $AMSO_4F$ (A= Na, NH_4 , M= Fe, Mn)

5.1 Introduction

Electrochemical properties of electrode materials are closely related to their crystal structure. This has led to multiple attempts in the past to design various synthetic control parameters to obtain the desired structure for a given composition. For example, some of the layered oxides based on transition metals ($LiMO_2$, M=Mn, Ni) that cannot be synthesized in the ordered layered polymorph using traditional synthesis methods, have been obtained using ion-exchange from $NaMO_2$. Remarkable improvements in the electrochemical performance are seen in co-substituted materials $LiMn_{0.5}Ni_{0.5}O_2$ when obtained using ion-exchange methods from $NaMn_{0.5}Ni_{0.5}O_2$.[227] The olivine $LiMPO_4$ are not thermodynamically stable as Li is replaced by Na.[228] $NaMPO_4$ crystalizes in maricite framework when synthesized using conventional solid state methods and does not show any electrochemical activity. Recently, however, it has been shown that olivine $NaFe_{1-x}Mn_xPO_4$ can be prepared by ion exchange method from $NH_4Fe_{1-x}Mn_xPO_4 \cdot H_2O$.[158] The replacement of Li by Na-ions in well-known positive electrode materials for Li-ion batteries is a very popular technique for finding good electrode materials for Na-ion batteries. In most cases, Na-analogues display completely different thermodynamic stability regimes and electrochemistry due to large ionic radius and greater mass of Na^+ compared to Li^+.

This chapter describes the synthesis and crystal structure of various Na^+ and NH_4^+ based transition metal fluorosulfate $AMSO_4F$ (A=Na^+, NH_4^+; M=Fe, Mn). Similar methods, as

described in previous chapters have been used to prepare these materials followed by PXRD and SEM characterizations. Rietveld refinements were carried out to determine structural details for each compound using TOPAS 4.2 and GSAS on EXPGUI platform.

5.2 Experimental

Synthesis methods described in **Chapter 2** and **Chapter 3** were used to prepare all the compounds described in this chapter. NaF (Sigma-Aldrich) or NH_4F (Sigma-Aldrich) and $MSO_4 \cdot H_2O$ (M=Fe, Mn) were used as precursors in order to synthesize $NaMSO_4F$ or NH_4MSO_4F respectively. NH_4FeSO_4F could also be synthesized by using $FeSO_4 \cdot 7H_2O$ instead of $FeSO_4 \cdot H_2O$ as the precursor. For the synthesis of $NaMSO_4F$ compounds, precursors were ball milled in a planetary ball mill (Fritsch pulverisette 5) under Ar atmosphere with typically 1:30 weight ratio of precursors to agate balls (10mm diameter) in an agate container for 10 hours. The ball milled mixture was transferred into a 43 ml Teflon^{TM}-lined Parr reactor along with 30 ml of the tetraethylene glycol (TEG) and stirred for 30 min. The reactor was then placed in an oven preheated to 220°C for the synthesis of $NaMSO_4F$. After 40 hours of heating, the reactor was taken out of the oven and cooled down on a lab bench to room temperature. No ball-milling of precursors was required for the synthesis of NH_4MSO_4F compounds, and in this case, they were separately added to the solvent tetraethylene glycol (TEG). The solution was transferred into a solvothermal reactor which was placed in a preheated oven at 200°C for 10 hours. Products were washed with dry acetone or tetrahydrofuran (THF) three times and vacuum filtered in a bench top glove-box filled with nitrogen followed by overnight drying in a vacuum oven at 100°C before characterization.

5.3 Results and Discussion

5.3.1 $NaFeSO_4F$

Following a topotactic reaction between NaF and $FeSO_4 \cdot H_2O$ in the glycol medium, $NaFeSO_4F$ precipitates after 40 hours of the reaction at 220°C under the conventional solvothermal conditions. The X-ray pattern is shown in **Figure 5.1** and displays all the characteristic peak of a tavorite-like compound**.** As shown in the SEM micrograph **Figure 5.1 (inset),** the particle size is much smaller than tavorite type $LiFeSO_4F$ (see **Chapter 3**), despite identical iron monohydrate precursor used in preparing both the materials. This can be explained by considering the topotactic reaction mechanism, since replacement of H^+ by bigger ion i.e. Na^+ in the precursor $MSO_4 \cdot H_2O$ creates much larger interfacial strain at the reactant-product phase boundary as compared to smaller Li^+ cation and leads to multiple fragmentation of the parent crystallites as the product $NaFeSO_4F$. Overall, framework connectivity in the structure remains the same as the tavorite type structure of the $LiFeSO_4F$, where FeO_4F_2 octahedra are corner shared *via* Fe-F-Fe link and share other corners with the SO_4 tetrahedra. PXRD pattern is indexed in a monoclinic space group ($P2_1/C$). Due to similar symmetry and lattice parameters, $CaTi(Ge_{0.336}Si_{0.663})O_5$ ($P2_1/a$, SG: 14) was chosen as the initial model for the refinement. The initial atomic positions of Ca, Ti, Ge/Si and one of the bridging O were replaced by Na, Fe, S and F atoms, and the setting was transformed to the standard $P2_1/c$ model. The structural details and bond lengths are listed in **Tables 5.1** and **5.2**. The differences with tavorite type $LiFeSO_4F$ in the relative rotation and disposition of the framework polyhedra give rise to slightly non-equivalent pathways for ion migration. Bond lengths in Fe-coordination (**Table 5.2**) are slightly longer on average than tavorite type $LiFeSO_4F$ and Na-X (X=O, F) distances are much longer than Li-X due to the bigger size of the Na^+ cation.

5.3.2 Electrochemistry of $NaFeSO_4F$

The results of electrochemical cycling of $NaFeSO_4F$ in a Li-electrolyte cell cycled between 2.5 V and 4.5 V vs. Li/Li^+ at a rate of C/20 are shown in **Figure 5.2**. On the initial charge cycle, a large overpotential is sustained up to 4.5 V, and there is no indication of a two-phase region indicative of Na extraction. Nonetheless, upon discharge, a plateau near 3.55 V is observed (as in $LiFeSO_4F$) and 55% of the theoretical capacity is achieved. We conclude that half the Na^+ is removed from the $NaFeSO_4F$ lattice on charge, possibly *via* ion-exchange with Li^+ in the electrolyte as the first step. The fraction of $FeSO_4F$ generated on charge becomes active for subsequent reversible Li^+ insertion, and the second charge cycle is different from the first. The re-inserted Li^+ is extracted near 3.65 V, and the same capacity is obtained as on first discharge. Additional overcharge to 4.5V on the second charge does not increase the capacity of the subsequent discharge step (**Figure 5.2**), indicating that some portion of the material is poorly accessible. Na^+ could be completely extracted from $NaFeSO_4F$ using an oxidizing agent, but more forcing conditions (1M $NOBF_4$ in acetonitrile for 4 days) were required compared to $LiFeSO_4F$.

Table 5.1 : Structural data obtained by refinement from powder XRD pattern of tavorite type $NaFeSO_4F$

$NaFeSO_4F$						
Space group: $P2_1/c$ (#14), Monoclinic M_w = 193.89 g/mol D = 3.35 g cm^{-3}						
a=6.6836(2) Å *b*=8.7054(3) Å *c*=7.1912(2) Å *β*=113.5236(3)° V = 383.64(3) $Å^3$						
Atom	**Wyck.**	***x/a***	***y/b***	***z/c***	**Occ.**	***B_{eq}* (Å^2)**
Na(1)	4*e*	0.2560(2)	0.0876(6)	0.7189(2)	1	3.82(8)
Fe(1)	4*e*	0.7493(2)	0.2489(1)	0.0067(2)	1	2.27(9)
S(1)	4*e*	0.2501(3)	0.43027(5)	0.7457(2)	1	2.41(2)
F(1)	4*e*	0.7617(3)	0.33915(8)	0.7528(3)	1	2.41(2)
O(1)	4*e*	0.4144(4)	0.3300(3)	0.9035(3)	1	2.41(2)
O(2)	4*e*	0.1006(4)	0.3283(3)	0.5987(3)	1	2.41(2)
O(3)	4*e*	0.3656(4)	0.5245(3)	0.6373(3)	1	2.41(2)
O(4)	4*e*	0.1398(4)	0.5258(3)	0.8527(3)	1	2.41(2)

Table 5.2 Selected bond lengths obtained by refinement from powder XRD pattern of tavorite type $NaFeSO_4F$

Atom 1	Atom 2	Multiplicity	Length (Å)
Na(1)	F(1)	1x	2.1793(9)
	O(2)	1x	2.3804(3)
	O(3)	1x	2.4050(3)
	O(1)	1x	2.4892(2)
	O(4)	1x	2.5594(3)
Fe(1)	F(1)	1x	1.9557(2)
	F(1)	1x	1.9669 (3)
	O(4)	1x	2.1346(3)
	O(1)	1x	2.1937(3)
	O(3)	1x	2.2333(3)
	O(2)	1x	2.2519(3)
S(1)	O(2)	1x	1.4749(3)
	O(1)	1x	1.4975(2)
	O(3)	1x	1.4331(3)
	O(4)	1x	1.5106(3)

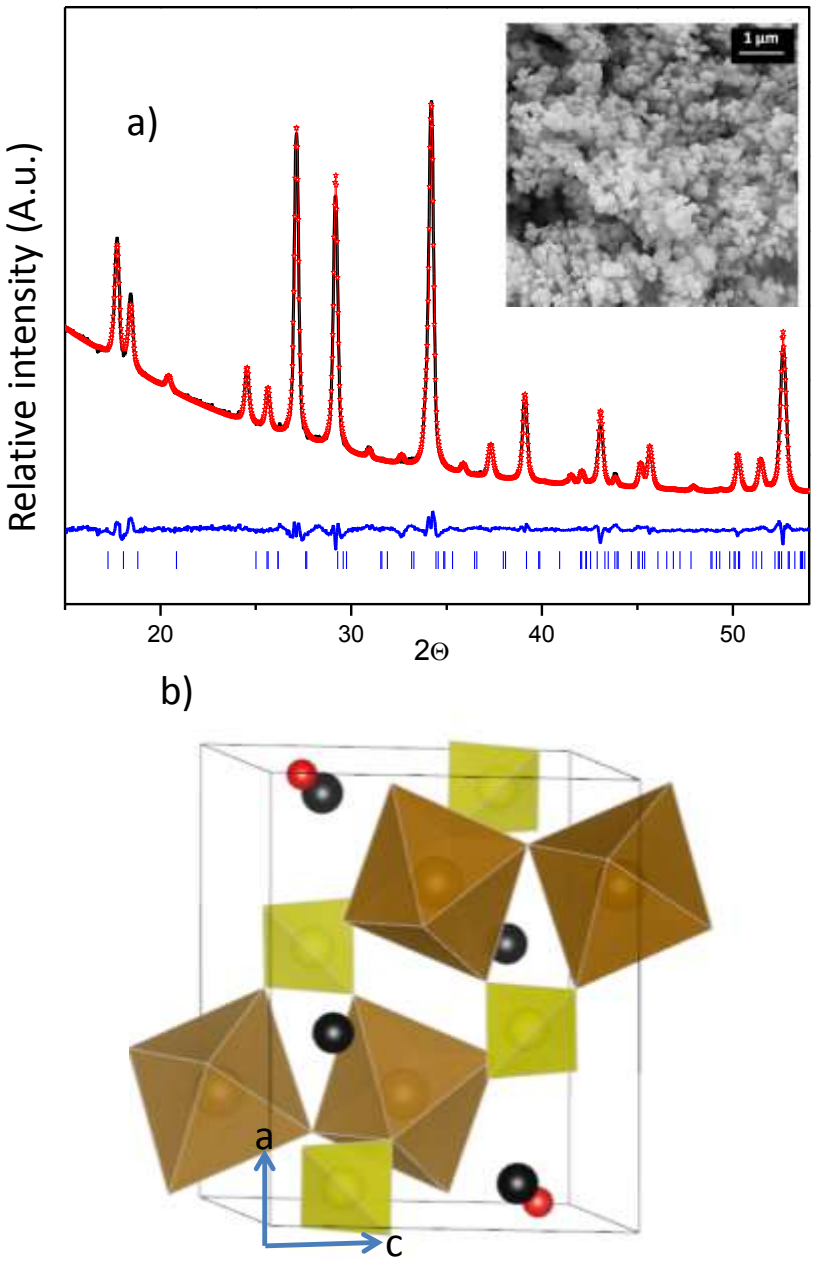

Figure 5.1 a) PXRD pattern of $NaFeSO_4F$. Black points represent experimental data, red solid lines show fitted data while blue lines show the difference map between observed and calculated data. Blue bars indicate the phase markers. X-ray diffraction agreement factors: R_{wp} = 2.91%, R_p = 2.19% χ^2= 2.11. b) Unit cell of $NaFeSO_4F$ obtained from the refinement (brown octahedra: FeO_4F_2, yellow tetrahedra: SO_4, red atoms: O, black atoms : Na).

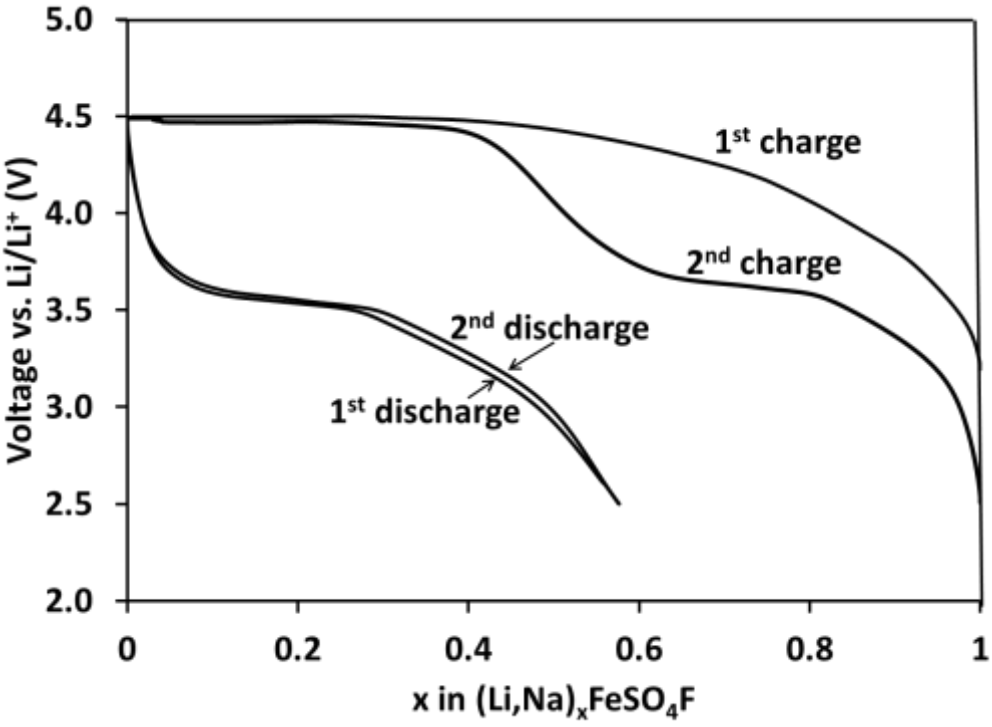

Figure 5.2 Electrochemical charge-discharge curve of tavorite $NaFeSO_4F$ (rate: C/20, active materials 80%, Super P : 20%).

5.3.3 $NaMnSO_4F$

$NaMnSO_4F$ was prepared by reacting NaF and $MnSO_4 \cdot H_2O$ at 220°C for 40 hours under solvothermal conditions with tetraethylene glycol (TEG) as the solvent. The X-ray pattern is shown in **Figure 5.2** along with the SEM micrograph (inset). $NaMnSO_4F$ is isostructural to the triplite type $LiMnSO_4F$ and the Rietveld refinement was carried out starting with this structural model in Bruker-AXS TOPAS 4.2 (**Figure 5.2**). The structural details and bond lengths obtained from the refinement are listed in **Tables 5.3** and **5.4**. Na and Mn are distributed over two sites; however, Mn is slightly more concentrated on the M1 site. This is in contrast with earlier conclusions that smaller atoms in triplites tend to occupy M2 site.[192] Bond lengths around metal sites are much longer than $LiMSO_4F$ triplites reported in **Chapter 3** due to larger size of the Na^+ cation.

Table 5.3 Structural data obtained by refinement from powder XRD pattern of triplite type $NaMnSO_4F$

$NaMnSO_4F$						
Space group: *C2/c* (#15), Monoclinic M_w = 192.99 g/mol D = 3.18 g cm^{-3}						
a=13.7657(9) Å *b*=6.6355(4) Å *c*=10.3446(7) Å *β*=121.4631(3)° V = 805.98(9) $Å^3$						
Atom	**Wyck.**	***x/a***	***y/b***	***z/c***	**Occ.**	***B_{eq}*(Å^2)**
Mn(1)	8*f*	0.64663(4)	0.90407(9)	0.83966(5)	0.5907(9)	4.48(2)
Na(1)	8*f*	0.64663(4)	0.90407(9)	0.83966(5)	0.4093(9)	4.48(2)
Mn(2)	8*f*	0.94901(4)	0.25351(9)	0.01104(5)	0.4093(9)	3.58(2)
Na(2)	8*f*	0.94901(4)	0.25351(9)	0.01104(5)	0.5907(9)	3.58(2)
S(1)	8*f*	0.32476(5)	0.5876(1)	0.19693(6)	1	3.87(1)
F(1)	8*f*	0.99312(8)	0.4119(1)	0.61533(9)	1	4.00(1)
O(1)	8*f*	0.21347(9)	0.6272(2)	0.1864(1)	1	4.00(1)
O(2)	8*f*	0.5905(1)	0.5238(1)	0.1487(1)	1	4.00(1)
O(3)	8*f*	0.69215(8)	0.4046(2)	0.4068(1)	1	4.00(1)
O(4)	8*f*	0.63571(8)	0.7526(2)	0.3500(1)	1	4.00(1)

Table 5.4 Selected Bond lengths obtained by refinement from powder XRD pattern of triplite type $NaMnSO_4F$

Atom 1	Atom 2	Multiplicity	Length (Å)
Mn(1)/Na(1)	O(3)	1x	2.1484(2)
	F(1)	1x	2.1758(8)
	F(1)	1x	2.2035(2)
	O(1)	1x	2.2194(2)
	O(4)	1x	2.2893(2)
	O(3)	1x	2.3933(9)
Mn(2)/Na(2)	F(1)	1x	2.1296(1)
	O(1)	1x	2.2432(1)
	O(4)	1x	2.2752(2)
	O(2)	1x	2.2912(1)
	O(2)	1x	2.3397(1)
	F(1)	1x	2.4037(1)
S(1)	O(4)	1x	1.4164(2)
	O(2)	1x	1.4647(1)
	O(1)	1x	1.5012(2)
	O(3)	1x	1.5554(2)

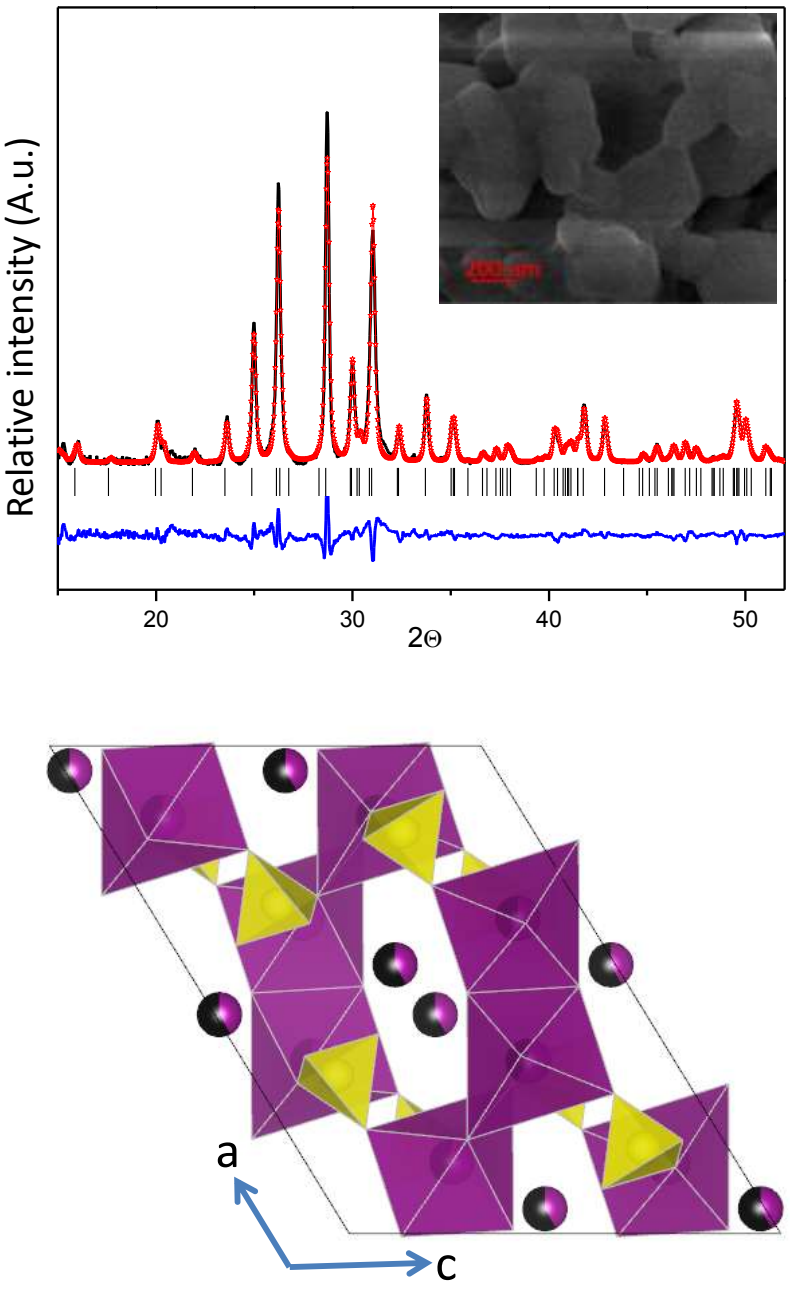

Figure 5.2 a) PXRD pattern of $NaMnSO_4F$ (black), the Rietveld refinement fit (red) and the difference map (blue) along with phase markers (black). X-ray diffraction agreement factors: R_{wp} = 3.49%, R_p = 2.53%, χ^2= 2.14. b) Unit cell of $NaMnSO_4F$ obtained from the refinement (pink octahedra: (Mn, Na)O_4F_2, yellow tetrahedra: SO_4, pink atoms: Mn, black atoms : Na),

5.3.4 NH_4FeSO_4F and NH_4MnSO_4F

NH_4FeSO_4F can be synthesized by reacting NH_4F and $FeSO_4 \cdot H_2O$ or $FeSO_4 \cdot 7H_2O$ at 200°C using solvothermal reaction conditions for 10 hours under conventional heating. Clearly, this is not a topotactic reaction as $FeSO_4 \cdot 7H_2O$ adopts a completely different structure than the product. The reactants used for NH_4MnSO_4F were NH_4F and $MnSO_4 \cdot H_2O$. The diffraction pattern and the refinement for NH_4FeSO_4F are shown in **Figure 5.3.** NH_4FePO_4F, which adopts orthorhombic space group $Pna2_1$, was used as the starting model for the refinement.[229] These compounds belong to the $KTiOPO_4$ (KTP) structure type.[230] Combined analysis obtained from single crystal diffraction and Mössbauer study of NH_4FePO_4F has been reported to conclude that these compounds display strict ordering[229] of O-F anions in this structure type. The structural details and bond lengths obtained from partial refinement of the pattern is reported in **Table 5.5** and **Table 5.6**. The refinement was limited to only lattice parameters and atomic positions occupied by transition metal and S atoms to obtain reasonable bond lengths. The structure is constructed by corner shared zig-zag chain of MO_4F_2 octahedra in [011] and [0-11] directions and two fluorine atoms in the same octahedra are in *cis* position for the M1 site and in *trans* position for the M2 site. Other four corners of the octahedra are shared with SO_4 tetrahedra. NH_4^+ cations are located in the tunnels which are oriented along *a* and *b* directions (**Figure 5.3**). NH_4MnSO_4F adopts similar structure as NH_4FeSO_4F (**Figure 5.4**). Structural details obtained from the refinement of the PXRD pattern of NH_4MnSO_4F are listed in **Table 5.7** and **Table 5.8**. Attempts of topotactic ion exchange in these materials in order to produce $NaFeSO_4F$ or $LiFeSO_4F$ did not produce single phase materials. To the best of my knowledge compounds NH_4FeSO_4F and NH_4MnSO_4F have never been reported before.

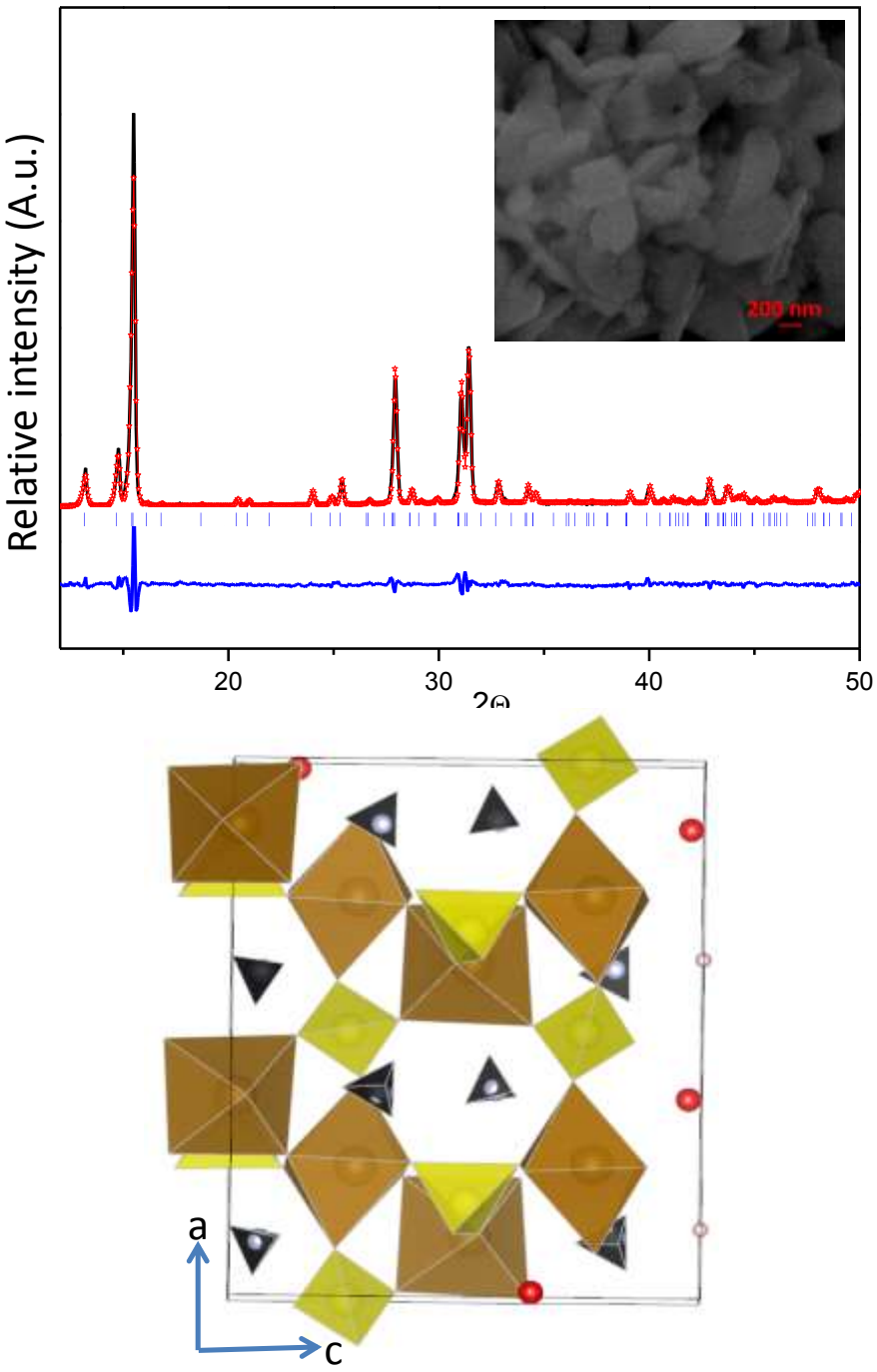

Figure 5.3 a) PXRD pattern of NH_4FeSO_4F (black), the Rietveld refinement fit (red) and the difference map (blue) along with phase markers (blue). X-ray diffraction agreement factors: R_{wp}=4.27%, R_p=1.92% χ^2=2.22. b) Unit cell of NH_4FeSO_4F obtained from the refinement (brown octahedra: FeO_4F_2, yellow tetrahedra: SO_4, red atoms: O, black tetrahedra :NH_4^+).

Table 5.5 Structural data obtained by refinement from powder XRD pattern of NH_4FeSO_4F

NH_4FeSO_4F						
Space group: *Pna*2_1 (#33), Orthorhombic M_w = 188.94 g/mol D = 2.61 g cm^{-3}						
a=13.2628(2) Å *b*=6.6525(7) Å *c*=10.8651(1) Å V = 958.63(2) $Å^3$						
Atom	**Wyck.**	***x/a***	***y/b***	***z/c***	**Occ.**	***B_{eq}*(Å^2)**
Fe(1)	4*a*	0.3774(7)	0.4953(4)	0.0155(2)	1	2
Fe(2)	4*a*	0.2509(2)	0.2662(2)	0.2693(2)	1	2
S(1)	4*a*	0.5046(4)	0.3394(2)	0.2476(3)	1	2
S(2)	4*a*	0.1754(2)	0.4982(5)	0.4986(4)	1	2
F(1)	4*a*	0.2748	0.4717	0.1298	1	2
F(2)	4*a*	0.2279	0.0327	0.3801	1	2
O(1)	4*a*	0.4867	0.4729	0.1355	1	2
O(2)	4*a*	0.5168	0.4686	0.3659	1	2
O(3)	4*a*	0.4037	0.2024	0.2694	1	2
O(4)	4*a*	0.5964	0.1893	0.2304	1	2
O(5)	4*a*	0.1164	0.3098	0.532	1	2
O(6)	4*a*	0.1166	0.6904	0.4756	1	2
O(7)	4*a*	0.2538	0.5487	0.6163	1	2
O(8)	4*a*	0.2552	0.457	0.3889	1	2
N(1)	4*a*	0.3897	0.7825	0.3131	1	2
N(2)	4*a*	0.0996	0.678	0.0646	1	2
H(1)	4*a*	0.393	0.91	0.327	1	4
H(2)	4*a*	0.39	0.761	0.235	1	4
H(3)	4*a*	0.335	0.733	0.344	1	4
H(4)	4*a*	0.441	0.724	0.346	1	4
H(5)	4*a*	0.132	0.672	0	1	4
H(6)	4*a*	0.117	0.584	0.11	1	4
H(7)	4*a*	0.039	0.666	0.05	1	4
H(8)	4*a*	0.11	0.785	0.099	1	4

Table 5.6 Selected bond lengths obtained by refinement from powder XRD pattern of triplite NH_4FeSO_4F

Atom 1	Atom 2	Multiplicity	Length (Å)
Fe(1)	F(1)	1x	1.8440(2)
	O(1)	1x	1.9494(2)
	F(2)	1x	2.0375(2)
	O(6)	1x	2.0719(3)
	O(5)	1x	2.0979(3)
	O(2)	1x	2.1530(2)
Fe(2)	O(8)	1x	1.8110(2)
	F(2)	1x	1.9828(2)
	F(1)	1x	2.0581(2)
	O(3)	1x	2.0686(3)
	O(4)	1x	2.1108(3)
	O(7)	1x	2.1965(2)
S(1)	O(1)	1x	1.5199(3)
	O(2)	1x	1.5482(3)
	O(4)	1x	1.5837(4)
	O(3)	1x	1.6343(4)
S(2)	O(6)	1x	1.5160(3)
	O(5)	1x	1.5189(3)
	O(8)	1x	1.6120(3)
	O(7)	1x	1.6762(3)

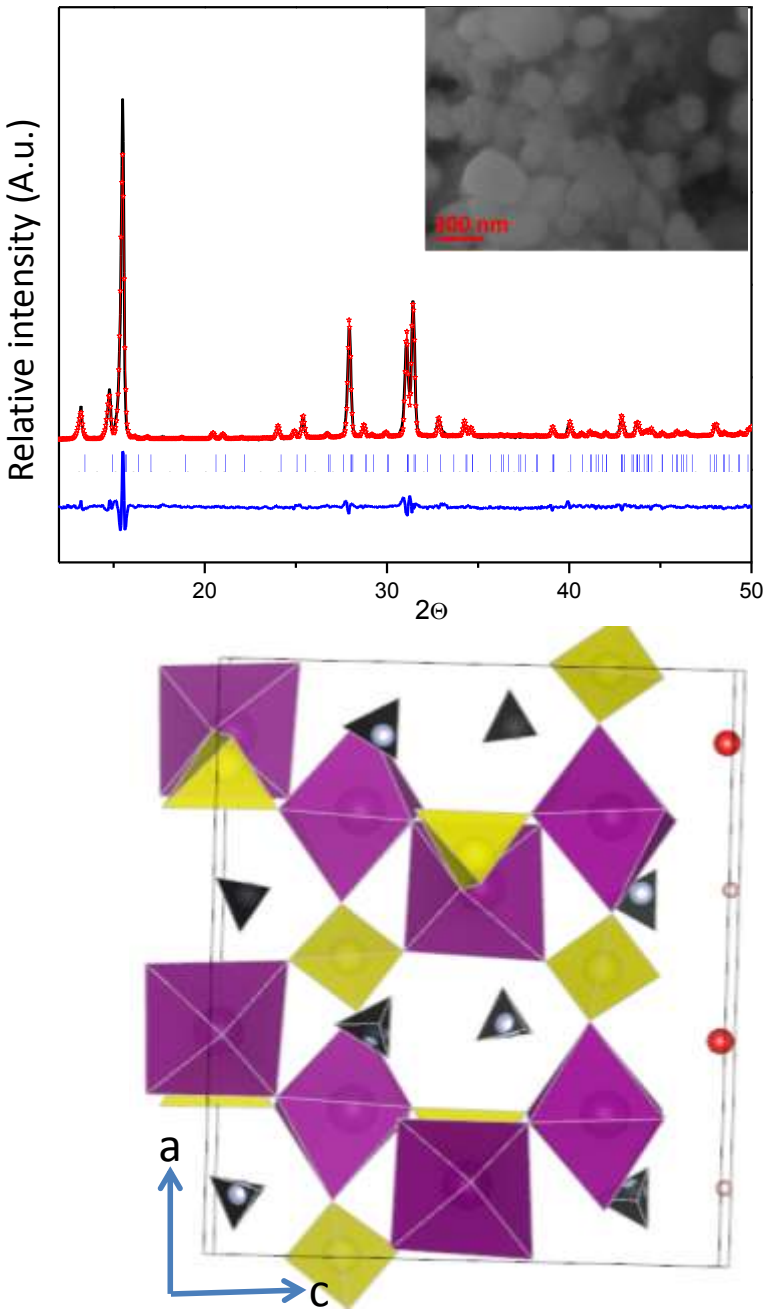

Figure 5.4 a) PXRD pattern of NH_4MnSO_4F (black), the Rietveld refinement fit (red) and the difference map (blue) along with phase markers (blue). X-ray diffraction agreement factors: R_{wp}=10.13%,R_p=3.48% χ^2 = 2.91. b) Unit cell of NH_4FeSO_4F obtained from the refinement (pink octahedra: MnO_4F_2, yellow tetrahedra: SO_4, red atoms: O, black tetrahedra :NH_4^+),

Table 5.7 Structure data obtained by refinement from powder XRD pattern of NH_4MnSO_4F

NH_4MnSO_4F						
Space group: *Pna*2_1 (#33), Orthorhombic Mw = 188.03 g/mol D = 2.50 g cm^{-3}						
a=13.3963(1) Å *b*=6.7181(8) Å *c*=11.0854(1) Å V = 997.66(2) $Å^3$						
Atom	**Wyck.**	***x/a***	***y/b***	***z/c***	**Occ.**	**B_{eq}(Å^2)**
Mn(1)	4*a*	0.3728(7)	0.4899(4)	0.0168(3)	1	2
Mn(2)	4*a*	0.2508(2)	0.2642(3)	0.2652(2)	1	2
S(1)	4*a*	0.5051(4)	0.3391(3)	0.2480(4)	1	2
S(2)	4*a*	0.1842(1)	0.5025(7)	0.4976(4)	1	2
F(1)	4*a*	0.26932	0.50888	0.12653	1	2
F(2)	4*a*	0.23811	0.05966	0.38256	1	2
O(1)	4*a*	0.48833	0.45012	0.13215	1	2
O(2)	4*a*	0.51456	0.46239	0.36467	1	2
O(3)	4*a*	0.41624	0.2227	0.27405	1	2
O(4)	4*a*	0.59618	0.20125	0.23202	1	2
O(5)	4*a*	0.12839	0.31557	0.53242	1	2
O(6)	4*a*	0.1164	0.67685	0.48034	1	2
O(7)	4*a*	0.24493	0.53686	0.61906	1	2
O(8)	4*a*	0.2532	0.45676	0.38833	1	2
N(1)	4*a*	0.3897	0.7825	0.3131	1	2
N(2)	4*a*	0.0996	0.678	0.0646	1	2
H(1)	4*a*	0.393	0.91	0.327	1	4
H(2)	4*a*	0.39	0.761	0.235	1	4
H(3)	4*a*	0.335	0.733	0.344	1	4
H(4)	4*a*	0.441	0.724	0.346	1	4
H(5)	4*a*	0.132	0.672	0	1	4
H(6)	4*a*	0.117	0.584	0.11	1	4
H(7)	4*a*	0.039	0.666	0.05	1	4
H(8)	4*a*	0.11	0.785	0.099	1	4

Table 5.8 Selected bond lengths obtained by refinement from powder XRD pattern of NH_4MnSO_4F

Atom 1	Atom 2	Multiplicity	Length (Å)
Mn(1)	F(1)	1x	1.8483(2)
	O(5)	1x	2.0257(2)
	O(6)	1x	2.1458(3)
	F(2)	1x	2.1541(2)
	O(1)	1x	2.1940(2)
	O(2)	1x	2.2859(2)
Mn(2)	F(2)	1x	1.8805(3)
	O(8)	1x	1.8995(3)
	O(3)	1x	2.1168(3)
	O(7)	1x	2.2267(3)
	F(1)	1x	2.2362(3)
	O(4)	1x	2.2637(3)
S(1)	O(4)	1x	1.4533(4)
	O(1)	1x	1.5018(4)
	O(2)	1x	1.5408(4)
	O(3)	1x	1.5419(4)
S(2)	O(6)	1x	1.4942(4)
	O(7)	1x	1.5113(4)
	O(8)	1x	1.5543(4)
	O(5)	1x	1.5899(4)

5.4 Conclusions

$NaFeSO_4F$, $NaMnSO_4F$, $NH_4MnSO4F$ and NH_4FeSO_4F have been synthesized using solvothermal techniques by employing conventional solvothermal method. $NaFeSO_4F$ adopts a tavorite like structure but with higher order of symmetry than tavorite like $LiFeSO_4F$. $NaMnSO_4F$ is isostructural to $LiMnSO_4F$ with almost equal distribution of Na and Mn on the two metal sites. Unlike other Mn and Fe based fluorosulfates ($LiFeSO_4F$-$LiMnSO_4F$ and $NaFeSO_4F$-$NaMnSO_4F$), NH_4FeSO_4F and NH_4MnSO_4F are isostructural and both adopt $KTiOPO_4$ structure type. Attempts of ion exchange of NH_4^+ with Na^+ or Li^+ in NH_4MSO_4F ions did not succeed.

Chapter 6

Summary and Future Outlook

Fluorosulfate based materials present an exciting opportunity to review and enrich our understanding of the basic electrochemistry-structure correlations in a metastable framework. The polymorphism displayed by $LiFeSO_4F$ is intriguing yet remarkably rewarding in terms of the electrochemical diversity. The tavorite type $LiFeSO_4F$ provides very facile Li-ion diffusion along multiple channels leading to a 3-D ionic conduction. This is a significant improvement over the last generation of phosphate materials, namely the olivines, without much compromise on specific energy density since the loss in capacity is almost completely compensated by an increase in the voltage (3.45 V – 170 mAh/g in olivine *vs*. 3.6 V – 151 mAh/g in tavorite). The change in the structure of tavorite type $LiFeSO_4F$ following a heat treatment or an extended reaction time is accompanied by a significant change in the lithium intercalation voltage (3.6 V-3.9 V) and Li^+ transport, which manifest in a Li-ion cell in the form of higher specific energy density but inferior rate capability. Cationic disorder in the triplite type compound also leads to a very well connected framework with relatively high density of atoms which minimizes the volume change upon Li-deintercalation.

$LiFeSO_4F$ can only be synthesized by using szomolnokite type $FeSO_4 \cdot H_2O$ as the precursor due to its metastability and that limits the synthetic access to this material. However, as reported in the current thesis, much studied solvothermal methods can be used to scale up the production of highly electrochemically active powders. Microwave heating can be used to produce slightly disordered tavorite type compound and surprisingly this can be converted to the triplite type

polymorph by a quick heat treatment. This unique phase transition, which is not observed in the tavorite type $LiFeSO_4F$ synthesized by other methods, provides the shortest and a very easy route for obtaining the triplite type $LiFeSO_4F$. In addition, microwave-assisted- method provides highly divided triplite type $LiFeSO_4F$, in contrast to the material obtained by conventional solvothermal technique. The fraction of lithium that can be reversibly intercalated in the triplite compounds is much higher for smaller size particles due to shortening of the lithium diffusion path lengths. However, more detailed study of the Li-intercalation process, long term cycling stability in a Li-ion cell and development of coating techniques to improve long term storage stability is required to further establish the credentials of these materials as positive electrodes.

The layered and olivine type Na-ion battery positive electrode materials are highly promising due to the abundant availability of the raw materials and their environmental friendliness. The atomistic scale simulations indicate that Na-ion conduction in the olivine type $NaMPO_4$ compounds occur along characteristic channel of the structure but with lower activation energy barrier than Li-ion in the olivine type $LiFePO_4$. The activation energy barrier for Na-ion diffusion is similar for the layered-Na_2FePO_4F but due to the distinct layered structural features, Na-ion conduction occurs along the *ac* plane. As a result, the presence of antisite defects in the layered-Na_2FePO_4F does not impact its electrochemical performance while in the olivine type compounds, these defects can be a major cause for the sluggish kinetics and irreversible capacity loss. In the tavorite type $NaFeSO_4F$, Na-ion conduction is restricted along the 1-D channels with twice activation energy barrier than that of the olivine type or layered materials. This renders the material with almost negligible electrochemical activity. Another important contributing factor to the electrochemical performance is volume change observed upon Na-de/-intercalation. In the olivine and tavorite type materials this becomes the dominating factor since both of them

undergo more than 10% volume change upon Na-de/-intercalation. In the layered Na_2FePO_4F, a more interconnected framework and the fact that only one Na is electrochemically extracted renders the framework much more robust which can sustain more cycling stability at higher rates.

Next generation of high specific energy density electrode materials must be designed to meet the growing needs for energy storage in the transport sector specifically. In order to allow industrial production, such materials must be made of environmentally friendly and abundantly available raw constituents. Since Li or Na and a transition metal are the basic constituents, an ideal candidate should be made of combination of some or all of the following elements: Li, Na, Fe, Mn, Ni, P, Si, S, and O. Some of the promising candidates built from this list are silicates and phosphates. However, assuming one lithium intercalation per transition metal, capacity and voltage are somewhat lower for the compounds from either of these groups. For silicate compounds such as Li_2MSiO_4 (M=Mn, Fe), theoretically, it should be possible to extract two lithium per transition metal. Three parameters of primary importance here are the intercalation voltage, Li-ion diffusion kinetics and the reversible capacity (gravimetric and volumetric). As shown in the current work and by many other examples in the literature, all of these three are at least partially dependent on the crystal structure of the compound. The commonly adopted tetrahedra based structure (Li_3PO_4 type) for silicates becomes unstable after delithiation and shows rapid capacity fade. Therefore, possibility of new structural polymorphs in silicates needs to be thoroughly explored in order to find a better framework that can address the rapid capacity fading in these materials. Low temperature synthesis methods including the solvothermal and the microwave solvothermal provide a temperature and pressure region which is still relatively

unexplored for inorganic synthesis of the functional materials and they should be vigorously pursued in order to synthesize new compounds for energy storage.

List of publications in peer reviewed journals from this research work

1) Scalable Synthesis of Tavorite $LiFeSO_4F$ and $NaFeSO_4F$ Cathode Materials, **Rajesh Tripathi**, T. N. Ramesh, Brian L. Ellis, Linda F. Nazar, *Angew. Chem. Int. Ed*., 2010, 49, 8738–8742.

2) Alkali-ion Conduction Paths in $LiFeSO_4F$ and $NaFeSO_4F$ Tavorite-Type Cathode Materials, **Rajesh Tripathi**, Grahame R. Gardiner, M. Saiful Islam, Linda F. Nazar, *Chem. Mater*., 2011, 23, 2278–2284

3) Lithium metal fluorosulfate polymorphs as positive electrodes for Li-ion batteries: Synthesis strategies and effect of cation ordering, **Rajesh Tripathi**, Guerman Popov, Brian L. Ellis, Ashfia Huq , Linda F. Nazar, *Energy Environ. Sci.*, 2012, 5, 6238-6246.

4) Ultrarapid microwave assisted synthesis of tavorite and triplite $LiFeSO_4F$, **Rajesh Tripathi**, Guerman Popov, Xioaqi Sun, Dominic H. Ryan, Linda F. Nazar, *J. Mater. Chem. A*, 2013, 1, 2990-2994

5) Na ion diffusion in Olivine $Na[Fe,Mn]PO_4$ and layered Na_2FePO_4F, **Rajesh Tripathi**, S.M. Wood, Saiful M. Islam, Linda F. Nazar, *Energy Environ. Sci*., 2013, 6, 2257-2264

References:

1 J.B. Goodenough *Report of the Basic Energy Science Workshop* Department of energy, April **2007**.

2 Nakecenovic, N. *World energy assessment: energy and the challenge of sustainability, chapter 9: energy scenarios,* United Nations Development Program, December **2000**.

3 Dunn, B.; Kamath, H.; Tarascon, J. M. *Science* **2011**, 334, 928.

4 Goodenough, J. B.; Kim, Y. *Chem. Mater*. **2010,** 22, 587.

5 Tarascon, J. M. ; Armand, M. *Nature* **2001,** 414, 359.

6 Whittingham, M. S. *Science* **1976**, *192*, 1126.

7 Whittingham, M. S.; Chianelli, R. R. *J. Chem. Educ.* **1980**, *57*, 569.

8 Whittingham, M. S. *Chemtech* **1979**, *9*, 766.

9 Holleck, G. L.; Driscoll, J. P. *Electrochim. Acta* **1977**, *22*, 647.

10 Thompson, A. H. *Phys. Rev. Lett.* **1975**, *35*, 1786.

11 Whittingham, M. S. *J. Electrochem. Soc.* **1976**, *123*, 315.

12 Haering, R. R.; Stiles, J. A. R.; Brandt, K. *U.S. Patent 4* **1980**, 224.

13 Whittingham, M. S. *Prog. Solid State Chem.* **1978**, *12*, 41.

14 Delmas, C.; Cognac-Auradou, H.; Cocciantelli, J. M.; Menetrier, M.; Doumerc, J. P. *Solid State Ionics* **1994**, *69*, 257

15 Walk, C. R.; Margalit, N. *J. Power Sources* **1997**, *68*, 723.

16 Mizushima, K.; Jones, P. C.; Wiseman, P. J.; Goodenough, J. B. *Mater. Res. Bull*. **1980**, 15, 783.

17 Ohzuku, T.; Ueda, A. *J. Electrochem. Soc.* **1994**, 141, 2972.

18 Yang, X. Q.; Sun, X.; McBreen, J. *Electrochem. Commun*. **2000**, 2, 100.

19 Reimers, J. N.; Dahn, J. R. *J. Electrochem. Soc.*, **1992**, 139, 2091.

20 Van der Ven, A.; Aydinol, M. K.; Ceder, G. *J. Electrochem. Soc*. **1998,** 145, 2149.

21 Chen, Z. H.; Lu, Z. H.; Dahn, J. R. *J. Electrochem. Soc*. **2002**, 149, A1604.

22 Rossen, E.; Reimers, J. N.; Dahn, J. R. *Solid State Ionics* **1993**, 62, 53.

23 Amatucci, G. G.; Tarascon, J. M.; Klein, L. C. *J. Electrochem. Soc.* **1996**, 143, 1114.

24 Nagaura, T.; Tozawa, K. *Prog. Batteries Solar Cells* **1990**, 9, 209.

25 Ozawa, K. *Solid State Ionics* **1994**, 69, 212.

26 http://www.cpsc.gov/cpscpub/prerel/prhtml07/07011.html

27 Delmas, C. *Mater. Sci. Eng.* **1989,** B3, 97.

28 Endo, E.; Yasuda, T.; Kita, A.; Yamaura, K.; Sekai, K. *J. Electrochem. Soc.* **2000**, 147, 1291.

29 Chembiam , R.V. ,. Kannan, A.M ; Prado, F.; Manthiram, A. *Electrochem. Comm.* **2001**, 3, 624.

30 Dahn, J. R.; Fuller, E. W.; Obrovac, M.; von Sacken, U *Solid State Ionics* **1994**, 69,265.

31 MacNeil, D.D.; Dahn, J.R. *J. Electrochem. Soc.* **2001**,148, A1205.

32 MacNeil, D.D.; Dahn, J.R. *J. Electrochem. Soc*. **2002**,149, A912.

33 Jung, Y.S.; Cavanagh, A. S.; Dillon, A. C.; Groner, M. D.; George, S. M.; Lee, S.H. *J. Electrochem. Soc.* **2010**, 157, A75.

34 Rougier, A.; Gravereau, P.; Delmas, C. *J. Electrochem*. Soc. **1996**, 143, 1168.

35 Conry, E.T.; Mehta, A.; Cabana, J.; Doeff, M.M. *Chem. Mater.* **2012**, 24 , 3307.

36 MacNeil, D.D.; Lu, Z.; Chen, Z.; Dahn, J.R. *J. Power Sources* **2002**, 1, 8.

37 Armstrong, A.; Bruce, P.G. *Nature* **1996**, 381, 499.

38 Lu, Z.; MacNeil, D.D.; Dahn, J.R. *Electrochem. Solid-State Lett.* **2001**, 12, A200.

39 Ohzuku, T.; Naoaki, Y. *J. Power Sources* **2003**, 119, 171.

40 Hwang, B. J.; Tsai, Y. W.; Carlier, D.; Ceder, G. *Chem. Mater.* **2003**, 15, 3676.

41 Kim, J. M.; Chung, H. T. *Electrochim. Acta* **2004**, 49, 937.

42 Yabuuchi, N.; Makimura, Y.; Ohzuku, T. *J. Electrochem. Soc.* **2007**, 154, A314.

43 Choi, J.; Manthiram, A. *J. Electrochem. Soc.* **2005**, 152, A1714.

44 Yin, S. C.; Rho, Y. H.; Swainson, I.; Nazar, L. F. *Chem. Mater.* **2006**, 18, 1901.

45 Kobayashi, H.; Arachi, Y.; Emura, S.; Kageyama, H.; Tatsumi, K.; Kamiyama, T. *J. Power Sources* **2005**, 146, 640.

46 Whitfield, P. S.; Davidson, I. J.; Cranswick, L. M. D.; Swainson, I. P.; Stephens, P. W. *Solid State Ionics* **2005**, 176, 463.

47 Reale, P.; Privitera, D.; Panero, S.; Scrosati, B. *Solid State Ionics* **2007**, 178, 1390.

48 Cahill, L. S.; Yin, S. C.; Samoson, A.; Heinmaa, I.; Nazar, L. F.; Goward, G. R. *Chem. Mater.* **2005**, 17, 6560.

49 Wang, Y. D.; Jiang, J. W.; Dahn, J. R. *Electrochem. Commun.* **2007**, 9, 2534.

50 Yabuuchi, N.; Ohzuku, T. *J.Power Sources* **2003**, 119, 171.

51 Thackeray, M. M.; David W.I.F.; Goodenough, J.B. *Mater. Res. Bull.* **1982 ,**17, 785.

52 Thackeray, M., M.; David, W.I.F.; Bruce, P.G.; Goodenough, J.B. *Mater. Res. Bull.* **1983,**18,461.

53 Thackeray, M. M. *Prog. Solid State Chem* **1997**, *25*, 1.

54 Yonemura, M.; Yamada, A.; Kobayashi, H.; Tabuchi, M.; Kamiyama, T.; Kawamoto, Y.; Kanno, R. *J. Mater. Chem.* **2004**, *14*, 1948.

55 Hunter, J. C. *J. Solid State Chem.* **1981,** 39, 142.

56 Barker, J.; Pynenburg R.; Koksbang, R. *J. Power Sources* **1994**, 52, 185.

57 Tarascon, J.M.; Wang, E.; Shokoohi, F.K ; McKinnon,W.R.; Colson, S. *J. Electrochem. Soc.***1991,** 138, 2859.

58 Ohzuku, T.; Kitagawa, M.; Hirai, T. *J. Electrochem. Soc.* **1990,** 137,769

59 Thackeray, M.M.; Johnson, P.J.; De Picciotto, L.A.; Bruce P.G. ; Goodenough, J.B. *Mater. Res Bull.* **1984**, 179

60 Thackeray, M. M. *Prog. Solid State Chem***. 1997**, 25, 71.

61 Gummow, R. J.; Kock, A.D., Thackeray, M.M. *Solid State Ionics* **1994**, 69, 59.

62 Bittihn, R.; Herr. R.; Hodge, D. *J. Power Sources* **1993**, 43, 223.

63 Zhong, Q.; Bonakdarpour, A.; Zhang, M.; Gao Y.; Dahn, J.R. *J Electrochem Soc.* **1997**, 144, 205.

64 Gao, Y.; Myrtle, K.; Zhang, M.; Reimers, J.N.; Dahn, J. R. *Phys. Rev.* **1996**, 54,16670.

65 Amine, K.; Tukamoto, H.; Yasuda, H.; Fujita, Y. *J. Electrochem. Soc* **1996**, 143, 1607.

66 Russouw M. H.; Thackeray, M. M. *Mater. Res. Bull.* **1991**, 26, 46.

67 Padhi, A.K.; Nanjundaswamy, K.S.; Masquelier, C.; Okada S.; Gooclenough J. B. *J. Electrochem. Soc.* **1997**,144, 1610.

68 Padhi, A.K.; Manivannan, V.; Goodenough, J. B. *J. Electrochem. Soc.* **1998**,145, 1518.

69 Padhi, A. K.; Nanjundaswamy, K. S.; Masquelier, C.; Goodenough, J. B. *J. Electrochem. Soc.* **1997**, 144, 2581.

70 Huang, H.; Yin, S.C.; Nazar, L.F. *Electrochem. Solid-State Lett*. **2001,** 4, A170.

71 Chen, Z. H.; Dahn, J. R. *J. Electrochem. Soc.* **2002**, 149, A1184.

72 Prosini, P. P.; Zane, D.; Pasquali, M. *Electrochim. Acta,* **2001**, 46, 3517.

73 Yamada, A.; Chung, S. C.; Hinokuma, K. *J. Electrochem. Soc.* **2001**,148, A224.

74 Herle, P. S.; Ellis, B.L.; Coombs, N.; Nazar, L. F. *Nature Mater*. **2004,** 3, 147.

75 Dominko, R.; Bele, M.; Gaberscek, M.; Remskar, M.; Hanzel, D.; Pejovnik, S.; Jamnik, J. *J. Electrochem. Soc* **2005**,152, A607.

76 Delacourt, C.; Poizot, P.; Levasseur, S.; Masquelier, C. *Electrochem. Solid-State Lett.* **2006,** 9, A352.

77 Striebel, K.; Shim, J.; Srinivasan, V.; Newman, J. *J. Electrochem. Soc.* **2005**, 152, A664.

78 Ellis, B.L.; Perry, L.K.; Ryan, D.H.; Nazar, L.F. *J. Am. Chem. Soc.* **2006**, 128, 11416.

79 Islam, M. S.; Driscoll, D. J.; Fisher, C. A. J. ; Slater, P. R. *Chem. Mater.* **2005,** 17, 5085.

80 Amin, R.; Maier, J.; Balaya, P.; Chen, D. P.; Lin, C. T. *Solid State Ionics,* **2008**, 179, 1683.

81 Srinivasan, V.; Newman, J. *J. Electrochem. Soc.* **2004,** 151, 10.

82 Delmas, C.; Maccario,M.; Croguennec, L.; Le Cras, F.; Weill, F. *Nature Mater.* **2008** 7, 665.

83 Gibot, P.; Casas-C.-M.; Laffont, L.; Levasseur, S.; Carlach, P.; Hamelet, S.; Tarascon, J-M.; Masquelier, C. *Nature Mater.* **2008**, 7,741.

84 Yamada, A.; Koizumi, H.; Nishimura, S-I.; Sonoyama, N.; Kanno, R.; Yonemura, M.; Nakamura, T.; Kobayashi, Y. *Nature Mater* **2006**,5,357.

85 Malik, R.; Zhou F.; Ceder G. *Nature Mater.* **2011**, 10, 587.

86 Delacourt, C.; Poizot, P.; Morcrette, M.; Tarascon, J.-M.; Masquelier, C. *Chem. Mater.* **2004**,16,93.

87 Delacourt, C.; Laffont, L.; Bouchet, R.; Wurm, C.; Leriche, J.-B.; Morcrette, M.; Tarascon, J.-M.; Masquelier, C. *J. Electrochem. Soc.* **2005**,152,A913.

88 Martha, S. K.; Grinblat, J.; Haik, O.; Zinigrad, E.; Drezen, T.; Miners, J.H.; Exnar, I.; Kay A.; Markovsky, B.; Aurbach, D. *Angew. Chem. Int. Ed*. **2009**, 48, 8559.

89 Srinivasan, V.; Newman, J. *Electrochem. and Solid State Lett*. **2006**, 9, A110.

90 Dominko, R.; Bele, M.; Gaberscek, M.; Meden, A.; Remskar, M.; Jamnik,J. *Electrochem. Comm.* **2006**, 8,217.

91 Kokalj, A.; Dominko, R.; Mali, G.; Meden, A.; Gaberscek, M.; Jamnik, J. *Chem. Mater.* **2007**, 19, 3633.

92 Nyten, A.; Kamali, S.; Haeggstroem, L.; Gustafsson, T.; Thomas, J. O. *J. Mater. Chem.* **2006,** 16, 2266.

93 Islam , M.S.; Dominko, R.; Masquelier, C.; Sirisopanaporn,C.; Armstrong, R. A.; Bruce, P.G. *J. Mater. Chem.* **2011**, 21, 9811.

94 Eames, C.; Armstrong A.R.; Bruce, P.G.; Islam M.S. *Chem. Mater.* **2012,** 24, 2155.

95 Arroyo-de Dompablo, M. E.; Armand, M.; Tarascon, J. M.; Amador, U. *Electrochem. Comm.* ***2*006,** 8, 1292.

96 Zaghib, K.; Ait Salah, A.; Ravet, N.; Mauger, A.; Gendron, F.; Julien, C. M *J. Power Sources* **2006**, 160, 1381.

97 Nishimura S.-I.; Hayase, S.; Kanno, R.; Yashima, M.; Nakayama, N.; Yamada, A. *J. Am. Chem. Soc.***2008**,130,13212.

98 Larsson, P.; Ahuja, R.; Nyten, A.; Thomas, J.O. *Electrochem. Comm*. **2006**, 8, 797.

99 Armstrong, A. R; Lyness, C.; Menetrier, M.; Bruce, P. G. *Chem. Mater*. **2010**, 22, 1892.

100 He, G.; Nazar, L.F. *Chem. Mater*. **2013** , 25, 1024.

101 Sirisopanaporn, C.; Boulineau, A.; Hanzel, D.; Dominko, R.; Budic, B.; Armstrong, A. R.; Bruce, P. G.; Masquelier, C. *Inorg. Chem*. **2010**, 49 , 7446.

102 Muraliganth, T.; Stroukoff, K. R.; Manthiram A. *Chem. Mater*. **2010,** 22, 5754.

103 Rangappa, D.; Murukanahally, K. D.; Tomai, T.; Unemoto, A.; Honma, I. *Nano Lett.* **2012,** 12, 1146.

104 Barker, J.; Saidi, M. Y.; Swoyer, J. L. J. *J. Electrochem. Soc*. **2003**, 150, A1394.

105 Ellis, B. L.; Makahnouk, W. R. M.; Rowan-Weetaluktuk, W. N.; Ryan, D. H.; Nazar, L. F. *Chem. Mater*. **2010**, 22, 1059.

106 Pizarro-Sanz, J. L.; Dance, J. M.; Villeneuve, G.; Arriortua-Marcaida, M. I. *Mater. Lett.* **1994**, 18, 327.

107 Barker, J.; Gover, R. K. B.; Burns, P.; Bryan, A.; Saidi, M. Y.; Swoyer, J. L. *J. Power Sources* **2005**, 146, 516.

108 Ramesh, T. N.; Lee, K.T.; Ellis, B. L.; Nazar, L.F. *Electrochem. Solid-State Lett.* **2010,** 13, A43.

109 Recham, N.; Chotard, J-N.; Jumas, J-C.; Laffont , L.; Armand M.; Tarascon, J.-M. C*hem. Mater*. **2010**, 22, 1142.

110 Aurbach, D. *ITE Letters on Batteries, New Technologies & Medicine* **2001**, 2, B42.

111 Aurbach, D.; Moshkovich, M. *J. Electrochem. Soc.* **1998**, 145, 2629.

112 Dahn J. R., Zheng, T.; Liu, Y.; Xue J.S. *Science* **1995,** 270, 590.

113 Dahn, J.R. ; Sleigh, A. K.; Shi, H.; Reimers, J.N.; Zhong, Q.; Way B.M. *J. New Mat. Electrochem. Systems* **1993**, 38, 1179.

114 Ohzuku, T.; Iwakoshi, Y.; Sawai, K.; *J. Electrochem. Soc.* **1993** 140, 2490.

115 Sato, K.; Noguchi, M.; Demachi, A.; Oki N.; Endo, M. *Science* **1994**, 264, 556.

116 Kambe, N.; Dresselhaus, M. S.; Dresselhaus, G.; Basu, S.; McGhie, A. R.; Fischer, J. E. *Materials Sci.and Eng.***1979,** 40, 1.

117 Dahn J. R. *Phy. Rev. B.* **1995**, 44, 17.

118 Mao, O.; Dunlap, R.A.; Dahn J.R. *J. Electrochem. Soc.***1999,** 146, 405.

119 Ji, L.; Lin, Z.; Alcoutlabi, M. ; Zhang, X. *Environ. Sci*. **2011**, 4, 2682.

120 Obrovac, M. N.; Christensen, L.; Ba, L. D.; Dahn, J. R. *J. Electrochem. Soc*. **2007**, 154, A849.

121 Zhang, W-J *J. Power sources* **2011**, 196,13.

122 Kasavajjulaa, U.; Wanga, C.; Appleby, A.J. *J. Power sources*, **2007**,163,1003.

123 Chevrier, V. L.; Zwanziger, J. W.; Dahn, J. R. *J. Alloys and Comp.* **2010,**496,25.

124 Limthongkul, P.; Jang, Y.I.; Dudney, N.J.; Chiang, Y.M. *Acta Materialia* **2003**, 51, 1103.

125 Beattie, S. D. ; Larcher, D.; Morcrette, M.; Simon, B.; Tarascon, J.-M. *J. Electrochem. Soc.* **2008,** 155, A158.

126 Graetz, J.; Ahn, C. C.; Yazami, R.; Fultz, B. *Electrochem. Solid-State Lett.* **2003**, 6, A194.

127 Hertzberg, B.; Alexeev , A.; Yushin, G. *J. Am. Chem. Soc.* **2010**, 132 , 8548.

128 Evanoff, K. ; Magasinski, A.; Junbing, Y.; Yushin, G. *Adv. Energy Mater*. **2011**, 1,495.

129 Yi, R.; Dair, F.; Mikhail, L. G.; Chem, S.; Wang, D. *Adv. Energy Mater*. **2013,** 3, 295.

130 Obrovac, M. N.; Christensen, L. *Electrochem. Solid-State Lett.* **2004**, 7, A93.

131 Li, J.; Dahn, J.R. *J. Electrochem. Soc.* **2007**, 154 , A156.

132 Key, B.; Bhattacharyya, R.; Morcrette, M.; Seznéc, V.; Tarascon, J.M.; Grey, C. P. *J. Am. Chem. Soc*. **2009,** 131, 9239.

133 Chan, K.C.; Ruffo, R.; Hong, S.S.; Huggins, R.A.; Cui, Y. *J. Power sources* **2009,** 189, 34.

134 Chan, K.C.; Peng, H.; Liu, G.; McIlwrath, K.; Zhang,X.F.; Huggins, R.A.; Cui, Y. *Nature Nanotech.* **2008**, 3, 31.

135 Kovalenko, I.; Bogdan, Z.; Magasinski, A.; Benjamin, H.; Milicev, Z.; Burtovyy, R.; Luzinov, I.; Yushin, G. *Science* **2011**, 334, 75.

136 Ferg, E.; Gummow, R. J.; de Kock, A.; Thackeray, M. M. *J. Electrochem. Soc.* **1994**,141, L147.

137 Ohzuku, T. ; Ueda, A.; Yamamoto N. *J. Electrochem. Soc.* **1995,** 142, 1431.

138 Slater, D.M.; Kim , D.M.; Lee, E.; Johnson, C.S. *Adv. Funct. Mater.* **2013**, 23, 947.

139 Palomares, V.; Serras, P.; Villaluenga, I.; Hueso, K.; Carretero-Gonzalez, J.; Rojo, T. *Energy and Env. Sci.* **2012**,5,5884.

140 Parant, J.P.; Olazcuaga, R.; Devalette, M.; Fouassier, C.; Hagenmuller, P. *J. Solid State Chem.* **1971**, 3, 1.

141 Mendiboure, A.; Delmas, C; Hagenmuller, P *J Solid State Chem* **1985,** 57, 323.

142 Ma, X.; Chen, H.; Ceder , G. *J. Electrochem. Soc*. **2011** , 12 , A1307.

143 Delmas, C.; Braconnier, J. J.; Fouassier, C.; Hagenmuller, P. *Solid State Ionics* **1981**, 3-4, 165.

144 Braconnier, J. J.; Delmas, C.; Fouassier, C.; Hagenmuller, P. *Mater. Res. Bull.* **1980**, 15, 1797.

145 Carlier, D.; Cheng, J. H., Berthelot, R.; Guignard, M.; Yoncheva M.; Stoyanova R. *Dalton Trans* **2011**, 40, 9306.

146 Doeff, M. M.; Richardson, T. J.; Kepley, L. *J. Electrochem. Soc.* **1996**,143, 2507.

147 Lee, J.-H; Black, R.; Popov, G.; Pomerantseva, E.; Nan, F.; Botton, G. A.; Nazar, L. F. *Energy and Env. Sci.***2012**,11,9558.

148 Cao, Y.; Xiao, L.; Wang, W.; Choi, D.; Nie, Z.; Yu, J. *Adv. Mater.* **2011,** 23, 3155.

149 Yabuuchi, N.; Kajiyama,M.; Iwatate, J.; Nishikawa, H.; Hitomi, S.; Okuyama, R.; Usui, R.; Yamada, Y.; Komaba, S. *Nature Mater.* **2012**, 11, 512.

150 Kim, D.; Kang, S. H.; Slater, M.; Rood, S.; Vaughey, J.T.; Karan, N.;Balasubramanian, M.; Johnson, C.S. *Adv. Energy Mater.* **2011,** 1, 333.

151 Plashnitsa, L. S.; Kobayashi, E.; Noguchi, Y.; Okada S. ; Yamaki, J.-I. *J. Electrochem. Soc.* **2010**, 157, A536.

152 Patoux, S; Rousse, G; Leriche, J-B; Masquelier, C. *Chem Mater* **2003,** 3, 2084.

153 Barker, J.; Saidi, M.Y.; Swoyer , J. L. *Electrochem. Solid-State Lett.* **2003** ,6 , A1.

154 Meins, J. Le *J. Solid State Chem*. **1999**, 148, 260.

155 Ellis, B.L.; Makahnouk, W.R.M.; Makimura, Y.; Toghill K.; Nazar, L.F. *Nature Mater.* **2007,**6, 749.

156 Berthelot R., Carlier D., Delmas C. *Nature Mater.* **2011**, 10, 74.

157 Recham N., Chotard J-N., Dupont L., Djellab K., Armand M., Tarascon J-M. *J Electrochem Soc* **2009,** 156:, A993.

158 Lee, K.T.; Ramesh, T.N.; Nan, F.; Botton, G.; Nazar, L.F. *Chem. Mater*. **2011**, 23, 3593.

159 Doeff, M.M.; Ma, Y.; Visco, S.J.; De Jonghe, L.C. *J. Electrochem. Soc.* **1993,**140, L169.

160 Stevens, D.A.; Dahn, J.R. *J. Electrochem. Soc.* **2000,** 147, 1271.

161 Wenzel, S.; Hara, T.; Janek, J.; Adelhelm, P. *Energy Environ Sci* **2011,**4, 3342.

162 Xiong, H.; Slater, M. D.; Balasubramanian, M.; Johnson , C. S.; Rajh , T. *J. Phys. Chem. Lett.* **2011** , 2 , 2560.

163 Senguttuvan, P.; Palacín, M.R. *Chem. Mater.* **2011**, 23, 4109.

164 Park, S.I.; Gocheva, I.; Okada, S.; Yamaki, J.-I. *J. Electrochem. Soc.* **2011,**158, A1067.

165 Walton, R.I. *Chem. Soc. Rev*. **2002**, 31, 230.

166 Demazeau, G. *J. Mater. Chem.* **1999**, 9, 15.

167 Feng, S.; Xu, R. *Acc. Chem. Res.* **2001**, 34, 239.

168 Baghbanzadeh, M.; Carbone, L.; Cozzoli, P.D.; Kappe C.O. *Angew. Chem. Int. Ed.* **2011**, 50, 2.

169 Carriazo, D.;Rossell, M.D.;Zeng, G.B.;Bilecka, I.;Erni, R;Niederberger, M. *Small* **2012**, 8, 2231.

170 Murugan, A. V.; Muraliganth, T.; Manthiram, A. *J. Phys. Chem. C* **2008**, 112, 14665.

171 Bilecka, I.; Hintennach, A.;Rossell, M. D.; Xie, D.;N. Petr.; Niederberger, M. *J. Mater. Chem.* **2011**, 21, 5881.

172 http://www.iucr.org/__data/assets/pdf_file/0010/721/chap4.pdf

173 Larson, A.C.; Von Dreele; R.B. *Los Alamos National Laboratory Report* **2004**, LAUR 86-748.

174 Toby, B.H. *J. Appl. Cryst.* **2001**, 34, 210.

175 Islam, M. S.; Slater, P. R. *MRS Bulletin* **2009**, 34, 935.

176 Gale, J.D. *J. Chem. Soc. Faraday Trans* **1997**, 93, 629.

177 Catlow, C. R. A. *Computer Modeling in Inorganic Crystallography* Academic Press: San Diego, CA, **1997**.

178 Gale, J.D *User Manual: General Utility Lattice Program : Version 4.0*

179 Ewald. P.P. *Ann. Phys*. **1921**, 64, 253.

180 Gale, J.D *Philosophical Magazine B* **1996**, 73, 3.

181 Kuganathan, N.; Islam, M. S. *Chem. Mater*. **2009**, 21, 5196.

182 Sebastian, L.; Gopalakrishnan, J.; Piffard, Y. *J. Mater. Chem*. **2002**, 12, 374.

183 Recham, N.; Chotard, J. N.; Dupont, L.; Delacourt, C.; Walker, W.; Armand, M.; Tarascon, J.-M. *Nature Mater*. **2010**, 9, 68.

184 Ati, M.; Walker, T.W.; Djellab, K.; Armand, M.; Recham, N.; Tarascon, J-M. *Electrochem. Solid-State Lett.* **2010**, 13, A150.

185 Harrison, K.L.; Manthiram, A.; *Inorg.Chem.* **2011**, 50, 3613.

186 Chen, M.; Xie, Y.; Lu, J.; Xiong, Y.; Zhang, S.; Qian, Y.; Liu, X. *J. Mater. Chem*. **2002**,12, 748.

187 Tang, K. B.; Qian, Y. T.; Zeng, J. H.; Yang, X. G. *Adv. Mater*. **2003**, 15 , 448

188 Yakubovich, O. V.; Urusov, V. S *Geokhimiya* **1997**, 7, 720.

189 Beitone, L.; Guillou, N.; Millange, F.; Loiseau, T.; Ferey, G *Solid State Sci.* **2002**, 4, 1061.

190 Barpanda, P.; Chotard, J.-N.; Delacourt, C.; Reynaud, M.; Filinchuk, Y.; Armand, M.; Deschamps M.; Tarascon, J. M. *Angew. Chem., Int. Ed.* **2011**, 50, 2526.

191 Liu, L., Zhang,B.; Huang, X.J. *Prog. In Nat. sciences: Mater. International* **2011**, 21, 211.

192 Kostiner, E. *Am. Mineral*. **1972**, 57, 1109.

193 Barpanda, P.; Ati, M.; Melot, B. C.; Rousse, G.; Chotard, J.-N.; Doublet, M.-L.; Sougrati, M. T.; Corr, S. A.; Jumas, J.-C; Tarascon, J.M. *Nature Mater*. **2011**, 10, 772

194 Cuisinier, M.; Martin, J.-F;. Dupre, N.; Yamada, A.; Kanno, R;. Guyomard, D. *Electrochem. Commun*. **2010**, 12, 238.

195 Ati, M.; Melot, B. C.; Chotard, J. N.; Rousse, G.; Reynaud, M.; Tarascon, J. M. *Electrochem. Comm.* **2011**, 13, 1280.

196 Ati, M.; Melot, B. C.; Chotard, J.-N.; Rousse, G.; Barpanda, P.; Tarascon, J.M. *Angew. Chem. Int. Ed.* **2011**, 50, 10574.

197 Sathiya, M.; Boulineau, S.; Reynaud, M.; Abakumov, A.; Rousse, G.; Melot, B.; Van Tendeloo, G.; Tarascon, J.M. *J. Am. Chem. Soc.* **2012**, 134, 18380.

198 Malik, R.; Burch, D.; Bazant, M.; Ceder, G. *Nano Lett.* **2010**, 10, 4123.

199 Ati, M.; Sougrati, M.-T; Rousse, G.; Recham, N.; Doublet, M.-L.; Jumas, J.-C.; Tarascon, J.M. *Chem. Mater.* **2012**, 24, 1472.

200 Nakamoto K.; *Infrared and Raman spectra of inorganic and coordination compounds part A: Theory and Applications in inorganic chemistry , 5th edition*; John wiley and sons Inc. **1997,** 160-161.

201 Azib, T.; Ammar, S.; Nowak,S.; Lau-Truing,S; Groult,H.; Zaghib,K.; Mauger,A.; Julien C.M. *J. Power Sources* **2012,** 217,220.

202 Chen, J.; Gratez, J. *Appl. Mater. Interfaces* **2011**, 3, 1380.

203 Chung, S.Y.; Choi, S.Y.; Yamamoto, T.; Ikuhara, Y. *Phys. Rev. Lett*. **2008,** 100,125502.

204 Komaba, S., Takei, C., Nakayama, T., Ogata, A. Yabuuchi, N. *Electrochem. Commun.* **2010**,12, 355.

205 Didier, C. *Electrochem. Solid-State Lett.* **2011**, 14, A75.

206 Doeff, M. M.; Peng, M. Y.; Ma, Y. P.; Dejonghe, L. C. *J. Electrochem. Soc.* **1994**, 141, L145.

207 Braconnier, J. J.; Delmas, C.; Hagenmuller, P. *Mater. Res. Bull* **1982**, 17, 993.

208 Gaubicher, J.; Wurm, C., Goward, G.; Masquelier, C.; Nazar, L. *Chem. Mater.* **2000**, 12, 3240.

209 Moreau, P.; Guyomard, D.; Gaubicher, J.; Boucher, F. *Chem. Mater.* **2010**, 22, 4126.

210 Kawabe, Y.; Yabuuchi, N.; Kajiyama M.; Fukuhara, N.; Inamasu, T.; Okuyama, R.; Nakai, I.;Komaba, S. *Electrochemistry* **2012**, 80, 8084.

211 Ong, S.P.; Chevrier, V.L.; Hauteir, G.; Jai, A.; Moore, C.; Kim, S.; Ma, X.; Ceder, G. *Energy Environ. Sci*. **2011**, 4, 3680.

212 Kawabe, Y.; Yabuuchi, N.; Kajiyama M.; Fukuhara, N.; Inamasu, T.; Okuyama, R.; Nakai, I.; Komaba, S. *Electrochem. Comm*. **2011**,13,1225.

213 Zhu, Y.; Xu, Y.; Liu, Y.; Luo, C.; Wang, C. *Nanoscale* **2013**, 5, 780.

214 Casas-Cabanas, M; Roddatis, V, V.; Saurel, D.; Kubiak, P.; Carretero-González, J.; Palomares,V; Serras, P.; Rojo, T. *J. Mater. Chem* **2012**, 22, 17421.

215 a) Allan, N. L.; Rohl, A. L.; Gay, D. H.; Catlow, C. R. A.; Davey, R. J.; Mackrodt, W. C. *Faraday Discuss*. **1993**, 95, 273 c) Sastre, G; Gale, J.D. *Chem. Mater*. **2005**, 17, 730 d). Gomez-Hortiguela, L; Cora, F; Catlow, CRA; Perez-Pariente, J. *J. Amer. Chem. Soc*. **2004**, 126, 12097.

216 Dick, B. G.; Overhauser, A. W. *Phys. Rev*. **1958**, 112, 90.

217 a) Jackson, R. A.; Valerio, M. E. G.; Lima, J. F. *J. Phys. Condensed Matter* **1996**, 8, 10931 b) Islam, M. S. ; D'Arco, S. *Chem. Comm.* **1996**, 2291.

218 Gale, J. D.; Rohl, A. L *Mol. Simul.* **2003,** 29, 291.

219 Kang, K.; Carlier, D.; Reed, J.; Arroyo, E.M.; Ceder, G.; Croguennec, L.; Delmas, C. *Chem. Mater.* **2003**, 15, 4503.

220 Sebastian, L.; Gopalakrishnan, J *J. Mater. Chem*. **2003**, 13, 433.

221 Ati, M; Sougrati, T. M.; Recham, N., Barpanda, P., Leriche, J.B.; Courty, M; Armand M.; Jumas, J. C.; Tarascon, J.M. *J. Electrochem. Soc.* **2010**, 157, A1007.

222 Liu Z., Huang X. *Solid State Ionics* **2010**, 181, 1209.

223 Schitz, A.K. I. *Solid State Ionic* **1997**, 100, 149.

224 Kutner , R. *Phys. Lett*. **1981**, 81, 239.

225 Van Der Ven, A.; Ceder G. *J. Power Sources* **2001**, 97-98, 529.

226 Delacourt, C.; Ati, M.; Tarascon, J. M. *J. Electrochem. Soc.* **2011**, 158, A741.

227 Kang, K. S.; Meng, Y. S.; Breger, J.; Grey, C. P.; Ceder, G. *Scienc*e **2006**, 311, 977.

228 Lepage, Y.; Donnay, G. *Can. Mineral.* **1977**, 15, 518.

229 Loiseau, Th.; Calage, Y.; Lacorre, P.; Frey, G. *J. Solid Sate Chem.* **1994**, 111, 390.

230 Tordjman, I.; Masse, R.; Guitel, J.C. *Z. Kristallogr.* **1974**, 139,103.